

CWP-326
December 1999



**2.5D Downward Continuation of the
Seismic Wavefield Using
Kirchhoff Data Mapping**

Steven D. Sheaffer

— Master's Thesis —
Mathematical and Computer Sciences

Center for Wave Phenomena
Colorado School of Mines
Golden, Colorado 80401
303/273-3557

TABLE OF CONTENTS

Chapter 1	INTRODUCTION	1
Chapter 2	GENERAL DERIVATIONS	5
2.1	The 2.5D data mapping formulation	5
2.2	Downward continuation of receivers	7
2.3	Downward continuation of sources	14
2.4	Implementation in general media	15
Chapter 3	CONSTANT-WAVESPEED MEDIA	17
3.1	Receiver continuation in a constant-wavespeed medium	17
3.2	Location of the stationary point for receiver continuation	19
3.3	Receiver continuation from a horizontal surface	21
3.4	Source continuation in a constant-wavespeed medium	22
3.5	Location of the stationary point for source continuation	23
3.6	Source continuation from a horizontal surface	25
3.7	Implementation options for constant-wavespeed media	25
Chapter 4	BASIC SYNTHETIC MODELS	27
4.1	Horizontal reflector and a horizontal recording surface	27
4.2	Horizontal reflector and a topographic recording surface	29
4.3	Curved reflector and a horizontal recording surface	37
4.4	Curved reflector and a topographic recording surface	45
Chapter 5	VALIDITY IN DATA MAPPING	53
5.1	Finite data aperture and ray theory	53
5.2	Finite data aperture and asymptotic wave theory	56
5.3	Data mapping and stationary phase	60
Chapter 6	COMPARISONS WITH OTHER DATUMING METHODS	69
6.1	Analytic comparisons	69
6.2	Comparison for synthetic data	74
6.3	Non-Kirchhoff methods	90

Chapter 7	CONCLUSIONS AND FUTURE WORK	93
7.1	Discussion and conclusions	93
7.2	Future work	96
Appendix A	DERIVATION OF THE FACTOR G	
	FOR CONSTANT-WAVESPEED MEDIA	99

ABSTRACT

Kirchhoff data mapping (Bleistein & Jaramillo, 1997, 1999) is a procedure for transforming seismic or acoustic data collected with one set of source/receiver locations and wavespeed model, to equivalent data collected in a different source/receiver configuration and wavespeed model. A major application of this general process is downward continuation of the wavefield, or wave-equation datuming. This study specializes the general data-mapping theory to the process of downward continuation of receivers given common-source data, and of sources given common-receiver data. Unlike many previous downward continuation algorithms, this procedure is not only kinematically correct, but is also dynamically correct in heterogeneous media, at least in a model-consistent sense. Furthermore, it does not require that the recording surface be horizontal, or even planar. Both of these features make the method applicable to wave-equation datuming of seismic data in areas of rough terrain, where preservation of amplitude or amplitude variation with offset (AVO) is important.

Implementation of the method in constant-wavespeed media allows the use of simple synthetic models to study the ability of the method to preserve amplitude in downward continuation, even when the recording surface is topographically varying. Accurate amplitudes do appear in the output, within a depth-dependent range of offsets, provided that various asymptotic validity conditions are obeyed. These conditions limit, among other things, the curvatures on the recording and reflecting surfaces. In general, amplitude accuracy in the downward continued data degrades when these curvatures are too large.

Analytic and numerical comparisons with more familiar Kirchhoff-datuming methods adapted to the extrapolation of line data show that the 2.5D data-mapping method is quantitatively different, and generally produces more accurate amplitudes and AVO in extrapolated data, particularly when the recording surface is not horizontal. Furthermore, Kirchhoff-datuming appears to break down faster than does the data-mapping method as validity conditions on the recording surface are violated.

ACKNOWLEDGMENTS

I wish to express my gratitude to some of the people that made this work possible. My advisor, Dr. Norman Bleistein, introduced me to the mathematical problem of amplitude preservation in seismic data processing, and to data mapping. His boundless enthusiasm for the subject kept me going through more than a few periods of frustration. Also, many thanks to Dr. Kenneth Larner, who served on the thesis committee and was instrumental in helping me to develop a clearer focus on the details and implications of the theoretical work in the context of its geophysical application. He is also a consummate editor, and is greatly responsible for making this thesis readable and comprehensible. Thanks to Dr. Willy Hereman, as well, the remaining member of the committee, who contributed greatly by pointing out the weak spots in early versions of the thesis.

A large debt of gratitude goes to The Center for Wave Phenomena for providing generous financial and intellectual support throughout my entire time at CSM. I am greatly indebted to all the students and faculty of CWP, of which there are too many to list here, with whom I have had the pleasure of working with over the last three years. Their help and contributions were invaluable.

Finally, I want to thank my wife, Jennifer, for her undying support over not only the last three years, but over my entire graduate career. Her sacrifices included two moves away from friends and family, and in particular, one that took her two-thousand miles away to Colorado.

Chapter 1

INTRODUCTION

Reverse propagation, or downward continuation, of the seismic wavefield is an important tool in seismic imaging, processing, and interpretation. It is most generally described as the process by which data collected on one acquisition surface are transformed to data that appear as if collected on another, usually deeper, recording surface, assuming some subsurface wavespeed model. While various approaches for downward continuation exist, the most versatile are probably the Kirchhoff-based methods.

Kirchhoff downward continuation methods are often used as a basis for Kirchhoff migration algorithms, such as that of Schneider (1978). In these methods, imaging at a depth point generally involves the combination of downward continuation and an appropriate imaging condition.

Downward continuation is also commonly applied as a preprocessing step, prior to further processing and migration. For example, data collected on a topographic recording surface must often be transformed to a horizontal datum prior to migration by algorithms that are unable to account for such a surface. Common implementations of frequency-domain migration methods, such as those of Stolt (1978) and Gazdag (1978), and finite-difference migration methods, including those reviewed in Berkhout (1981), generally require the input surface to be horizontal. In areas of complex, near-surface structure, where propagation is not generally vertical, datum correction via wave-theoretical downward continuation may be preferable to an approximate, vertical static correction, with respect to the accuracy of subsequently migrated results. Recent studies concerning the use of datuming versus static correction prior to migration are given in Zhu et al. (1995), and Salinas (1997).

Another notable application of downward continuation is in multi-step, layered migration. A migration procedure that alternates steps of downward continuation and migration is introduced in Bevc (1995) as a cost-effective method to reduce the degradation of Kirchhoff migrated images using first-arrival traveltimes.

Regardless of how downward continuation is employed in data processing, it generally has a significant influence on the final image. In applications that require accurate amplitude-variation-with-offset (AVO) or amplitude-variation-with-angle (AVA) analysis, a downward-continuation algorithm that preserves amplitude is necessary to prevent the introduction of erroneous amplitudes that result in degradation of the migrated image. Furthermore, a method that produces results that are both kinematically and dynamically accurate in heterogeneous media is highly desirable, as is one that correctly accommodates a topographically-varying input surface.

In this study, expressions are developed that perform “true-amplitude” down-

ward continuation in heterogeneous media, at least in the sense that the amplitude mapping is consistent with the assumed wavespeed model. This involves the derivation and analysis of integral expressions for 2.5D downward continuation of receivers or sources for offset data based on the 2.5D Kirchhoff data-mapping theory of Bleistein & Jaramillo (1997, 1999).¹ This approach is desirable for several reasons. First, data mapping is a general, dynamically accurate theory for the transformation of data from one survey configuration to another, where the input and output surfaces are not assumed to be horizontal. Second, 2.5D theory accounts for amplitude in data that are truly 3D but collected in a linear survey, provided that the survey line is oriented normal to the dominant structural axis, or equivalently, parallel to the direction of the dominant structural dip.

The development of this method begins in Chapter 2, where the general, “true-amplitude” data-mapping formula in 2.5D (Bleistein & Jaramillo, 1997, 1999) is specialized to the process of the downward continuation of receivers given data in a common-source gather, and of sources given data in a common-receiver gather. Stationary phase analysis of the general formula under the assumption of these geometries results in a Kirchhoff-like integral for performing the downward continuations. That is, the downward-continued field at a given output receiver location on the datum and output time, is an integral over weighted contributions from each input receiver in the data, or equivalently, each data trace.

Evaluation of the weights in the integrand depends on the evaluation of various Jacobians on the paths to and from a particular stationary point in the medium. This stationary point must be determined for each combination of input and output location and output time. Stationary phase analysis locates this point at the intersection of a reflection isochron related to a particular input time and the ray connecting the input and output locations. This input isochron has the property that it is tangent to the isochron associated with the desired output time at this intersection point.

Location of each stationary point requires knowledge of the isochron geometry and the tracing of rays to find the proper intersection. While the downward continuation formula derived is valid for a general heterogeneous medium, this procedure, and the subsequent evaluation of the required factors in the integrand, may be computationally expensive, demanding a great deal of information from external ray tracing. Even though a specific procedure to accomplish this is not described here, it is evident that the large cost makes extrapolation in a completely general medium somewhat impractical.

In more simple wavespeed models, though, enough generalizations about the isochron geometry may be possible to greatly simplify this process. So, to facilitate more tractable calculations for testing and other purposes, Chapter 3 concentrates on the specialization of these general results to constant-wavespeed media.

For constant wavespeed, isochrons are elliptical and rays are straight lines. There-

¹Downward extrapolation of both sources and receivers is generally required to accommodate many common migration algorithms, which require sources and receivers to be on the same input surface.

fore, analytic expressions can be developed for the location of the stationary point, given the traveltime. These expressions are derived in Chapter 3 for both a horizontal recording surface and a general, topographic recording surface.

Using the constant-wavespeed forms of the process, Chapter 4 investigates the results of various synthetic models, and discusses the general features of the method. Using simple homogeneous models with a single reflector, it is shown that the data-mapping method produces accurate amplitudes in downward continued data, within a particular range of offsets. This range has a width that decreases as the depth of the datum is moved closer to that of the target reflector. Examples of amplitude preservation in data-mapping are shown for horizontal and topographic recording surfaces, as well as for horizontal and irregular reflector surfaces.

The data-mapping procedure is a leading-order asymptotic method, and, therefore, produces accurate results only when it obeys various asymptotic validity conditions. Chapter 5 discusses these conditions in detail, specifically those that involve finite extent of input data and stationary phase evaluations inherent in the data-mapping theory. The inherent stationary phase approximations are shown to produce a set of general validity conditions on length scales in the problem, which imply a set of conditions on the curvatures of the recording and reflecting surfaces.

Chapter 6 compares data mapping to more familiar Kirchhoff-datuming approaches. Specifically, it addresses the methods of Berryhill (1979), Bevc (1995), and Salinas (1997), all of which adapt a common Kirchhoff-based 3D downward continuation integral to line data. It is shown that these adapted methods differ from data mapping in two significant ways. First, they are not 2.5D methods, that is, they do not preserve amplitudes for point-source data. Second, unlike data mapping, they explicitly assume a horizontal recording surface in their derivations. Using the identical result of Bevc (1995) and Salinas (1997), it is shown that these facts result in a significant difference between the integrals derived in these studies and those in data mapping. Then, downward continuation results for both methods are calculated for simple, homogeneous synthetic models in order to illustrate the differences in the methods in terms of amplitude preservation. The data-mapping method is generally more accurate with respect to amplitude and amplitude variation with offset than is the Kirchhoff-datuming method, particularly when the input surface is not horizontal. This is shown to be generally true, even when length scale constraints on the input surface are violated, and both methods are expected to be in error.

Finally, Chapter 7 summarizes the study and offers some general conclusions. It also discusses the next important steps in the development of the method, and makes suggestions for further research.

Chapter 2

GENERAL DERIVATIONS

The derivation of a general formulation for 2.5D downward continuation begins here with the introduction of the 2.5D assumption and the general Kirchhoff data-mapping platform. A common-source geometry is then assumed, and a general method for downward continuation of receivers is derived, via stationary phase analysis of the data-mapping integral. From this result, the analogous expression for continuation of sources follows directly. The formulas produced are general with respect to wavespeed heterogeneity, as well as the shapes of the recording and datum surfaces, at least within the assumptions inherent to the data mapping platform, and those required by the asymptotic analyses.

2.1 The 2.5D data mapping formulation

To adequately characterize the 3D nature of the subsurface, 3D data acquisition and processing is generally required. Given the expense of conducting fully 3D seismic surveys, however, it is often still attractive to collect data in linear surveys. The problem with this is that 2D processing is generally applied to such data. Truly 2D methods, however, assume that the source is a line source, perpendicular to the line of the survey. In this configuration, the generated wavefield undergoes 2D geometrical spreading. Since the seismic source is generally approximated as a point, or at least localized, source of waves that undergo 3D geometrical spreading, 2D processing will not produce correct amplitudes.

The 2.5D approach is one alternative that is applicable when the linear survey is conducted in the direction of the dominant structural dip of the subsurface. Assume a Cartesian coordinate system where the orthogonal directions x_1 and x_2 reside in a horizontal plane at the surface, with the x_1 -direction oriented parallel to the survey line. If the subsurface structure is assumed to be constant in the x_2 -direction, normal to the survey, then no energy is reflected back into the vertical plane extending below the survey (the survey plane) from any out-of-plane reflectors. This condition allows the x_2 dependence in an appropriate 3D integral expression for propagation to be eliminated by stationary phase. The resulting equation depends on only the in-plane variables, but will preserve amplitude variation due to 3D geometrical spreading. This is known as the two-and-one-half dimensional (2.5D) approximation. A full discussion is found in Bleistein (1986) and Bleistein et al. (1997).

Kirchhoff data mapping, hereafter just *data mapping*, as developed in Bleistein & Jaramillo (1997, 1999), is a general integral expression that allows seismic sources and receivers of some arbitrary input configuration to be mapped to some other output

configuration. They derive a general, 3D data-mapping integral by cascading an inversion formula and a modeling formula. This is achieved by replacing the spatially-dependent reflectivity in the modeling formula with an appropriate expression for data inversion. This is equivalent to inverting the input data for reflectivity and then remodeling through this reflectivity distribution to the output locations, all in one process. Subsequent analysis yields a simplified true-amplitude data-mapping platform in 3D, which features spatial integrations over all subsurface depth points and over the input data surface. They then derive the 2.5D version of the platform by making the subsurface assumption described above, and eliminating both the x_2 integral in the subsurface and that on the recording surface by two stationary phase approximations. This procedure yields a true-amplitude data-mapping platform for in-plane input and output survey configurations, under the assumption of constant structure in the direction normal to the vertical plane containing the data lines.

Following Bleistein & Jaramillo (1997, 1999), the general 2.5D data-mapping integral is

$$\begin{aligned}
 u_O(\xi_O, \omega_O) \approx & \frac{\sqrt{|\omega_O|}}{4\pi^2} e^{-i\pi/4 \operatorname{sgn}(\omega_O)} \iiint \sqrt{|\omega_I|} e^{i\pi/4 \operatorname{sgn}(\omega_I)} u_I(\xi_I, \omega_I) \frac{a_O(\mathbf{x}, \xi_O)}{a_I(\mathbf{x}, \xi_I)} \\
 & \cdot \frac{|\nabla_{\mathbf{x}} \tau_O(\mathbf{x}, \xi_O)|}{|\nabla_{\mathbf{x}} \tau_I(\mathbf{x}, \xi_I)|} \frac{\sqrt{\sigma_{IS} + \sigma_{IG}}}{\sqrt{\sigma_{OS} + \sigma_{OG}}} \frac{\sqrt{\sigma_{OS} \sigma_{OG}}}{\sqrt{\sigma_{IS} \sigma_{IG}}} |H(\mathbf{x}, \xi_I)| \\
 & \cdot e^{(i\omega_O \tau_O(\mathbf{x}, \xi_O) - i\omega_I \tau_I(\mathbf{x}, \xi_I))} d\omega_I d\xi_I dx_1 dx_3 .
 \end{aligned} \tag{2.1}$$

Here, the survey plane is defined on a Cartesian coordinate system, with x_1 indicating the horizontal direction, and x_3 the denoting the vertical (depth) direction. The position vector \mathbf{x} describes the locations of scattering points in this plane, and is the integration variable for the $dx_1 dx_3$ integration. As usual, ω is the angular frequency. The subscripts I and O denote quantities associated with the input and output configurations, respectively. The subscripts S and G indicate source and geophone, with all vectors evaluated in the survey plane. Source locations in the input data are given by \mathbf{x}_{IS} and receiver locations by \mathbf{x}_{IG} . Each source-geophone pair is described by a parameter ξ_I , so the $d\xi_I$ indicates an integration over the input data. Analogous quantities in the output data are given by \mathbf{x}_{OS} , \mathbf{x}_{OG} , and ξ_O . The ratio,

$$\frac{a_O(\mathbf{x}, \xi_O)}{a_I(\mathbf{x}, \xi_I)} = \frac{A(\mathbf{x}, \mathbf{x}_{OS}(\xi_O)) A(\mathbf{x}_{OG}(\xi_O), \mathbf{x})}{A(\mathbf{x}, \mathbf{x}_{IS}(\xi_I)) A(\mathbf{x}_{IG}(\xi_I), \mathbf{x})} , \tag{2.2}$$

is the quotient of the output to input amplitudes, where each a is the product of the 3D Green's function amplitudes, A , evaluated in the survey plane, as required by the 2.5D theory. The denominator is the product of the amplitudes associated with the paths from \mathbf{x}_{IS} to the scattering point \mathbf{x} , and from \mathbf{x} to \mathbf{x}_{IG} in the input data. The numerator is the product of amplitudes associated with the paths from \mathbf{x}_{OS} to the scattering point \mathbf{x} , and from \mathbf{x} to \mathbf{x}_{OG} , in the output data. It is important to note that these are ray-theoretical Green's functions, and are not valid in the presence of a caustic. In equation (2.1), the factor

$$H(\mathbf{x}, \xi_I) = \det \left| \begin{array}{c} \nabla_{\mathbf{x}} \tau_I(\mathbf{x}, \xi_I) \\ \frac{\partial}{\partial \xi_I} \nabla_{\mathbf{x}} \tau_I(\mathbf{x}, \xi_I) \end{array} \right| \quad (2.3)$$

is the 2D Beylkin determinant for the problem, evaluated in-plane as prescribed by the 2.5D result. A full discussion of this factor is found in Bleistein et al. (1997). The symbol σ represents a parameter measured along the raypath from a scatterer to a source or receiver location, as

$$\left(\frac{\partial \mathbf{x}}{\partial \sigma} \right)^2 = \mathbf{p} \cdot \mathbf{p} = |\nabla \tau|^2 = \frac{1}{c^2(\mathbf{x})}, \quad (2.4)$$

and

$$d\sigma = c^2(\mathbf{x}) d\tau, \quad (2.5)$$

where \mathbf{p} is the ray vector, $c(\mathbf{x})$ is the wavespeed, and τ is travel time along the ray. As before, the subscripts S and G indicate a parameter evaluated on the source-to-scatterer and scatterer-to-geophone paths, respectively.

The data-mapping formulation is referred to here as a “platform.” This choice of terminology reflects the fact that this general integral expression can be modified, and hopefully simplified, for specific data-mapping applications. One of the most important of these applications is downward extrapolation of the wavefield. This is achieved by asymptotic analysis of the 2.5D data-mapping platform expression, for the source and receiver configurations specific to this application. Extrapolation of prestack data requires the downward continuation of both receivers and sources, and is approached here as a two-step, cascaded process.

2.2 Downward continuation of receivers

Consider the problem of the downward continuation of receivers with a fixed source (common-source gather). This implies

$$\mathbf{x}_{OS} = \mathbf{x}_{IS} = \mathbf{x}_S = \text{constant}. \quad (2.6)$$

As previously defined, ξ_I parameterizes all source-geophone combinations in the input data. In a fixed-source configuration, this parameter needs only to distinguish among geophones. So, here ξ_I is associated with the lateral, or x_1 , coordinates of the receiver locations on the input surface. The parameter ξ_O denotes the same for receiver locations on the output surface.¹

¹Since evaluation of the 2.5D expression is over a 2D vertical plane, the source and receiver locations are properly described as being on input and output *curves*. However, to be consistent with common geophysical terminology, these curves are referred to as the input and output *surfaces*, to refer to their association with geologic “surfaces”, such as that of the Earth, and not with a 3D mathematical surface.

To obtain an expression useful for application of the theory, the spatial integration in equation (2.1) is reduced to an integral over the input data only. The integration over the survey plane is performed analytically, making use of asymptotic methods such as the method of stationary phase. For problems of this type, the derivatives required for stationary phase are more easily evaluated following a change in variables from (x_1, x_3) to coordinates based on reflection traveltime isochrons. In this context, an isochron denotes any surface of scattering points, that, for a given source and receiver, produces arrivals with equal traveltime, τ , from source to scattering point to receiver. For example, in constant-wavespeed media these curves are ellipses.

For a given source and receiver pair in the input, and a given receiver location in the output, each depth point \mathbf{x} lies on the intersection of two of these isochronal curves of constant reflected traveltime. One is associated with the traveltime τ_I from the source to the input receiver location, and the other is associated with the traveltime τ_O from the source to the output receiver location, both via a point \mathbf{x} in the medium. Therefore, $dx_1 dx_3$ is transformed to $d\gamma d\tau$, where τ is an isochron and γ is a parameter along τ . This geometry is shown in Figure 2.1. Since each subsurface point lies on both an input and an output isochron, the integration can be performed along either one. For reasons that emerge in the following analysis, the input isochron, τ_I will be used. This means that

$$\mathbf{x} = f(\gamma_I, \tau_I) , \quad (2.7)$$

and

$$dx_1 dx_3 = \left| \frac{\partial(\mathbf{x})}{\partial(\gamma_I, \tau_I)} \right| d\gamma_I d\tau_I , \quad (2.8)$$

where the factor relating the two sets of differentials is the Jacobian of transformation from (x_1, x_3) to (γ_I, τ_I) . In terms of these new variables, equation (2.1) becomes

$$\begin{aligned} u_O(\xi_O, \omega_O) \approx & \frac{\sqrt{|\omega_O|}}{4\pi^2} e^{-i\pi/4 \operatorname{sgn}(\omega_O)} \iiint \sqrt{|\omega_I|} e^{i\pi/4 \operatorname{sgn}(\omega_I)} u_I(\xi_I, \omega_I) \frac{a_O(\mathbf{x}, \xi_O)}{a_I(\mathbf{x}, \xi_I)} \\ & \cdot \frac{|\nabla_{\mathbf{x}} \tau_O(\mathbf{x}, \xi_O)|}{|\nabla_{\mathbf{x}} \tau_I(\mathbf{x}, \xi_I)|} \frac{\sqrt{\sigma_{IS} + \sigma_{IG}}}{\sqrt{\sigma_{OS} + \sigma_{OG}}} \frac{\sqrt{\sigma_{OS} \sigma_{OG}}}{\sqrt{\sigma_{IS} \sigma_{IG}}} |H(\mathbf{x}, \xi_I)| \\ & \cdot e^{(i\omega_O \tau_O(\mathbf{x}, \xi_O) - i\omega_I \tau_I(\mathbf{x}, \xi_I))} \left| \frac{\partial(\mathbf{x})}{\partial(\tau_I, \gamma_I)} \right| d\gamma_I d\tau_I d\omega_I d\xi_I , \end{aligned} \quad (2.9)$$

where \mathbf{x} is understood to be a function of γ_I and τ_I through the change in variables, as defined in equation (2.7).

The next step is to approximate the γ_I integral by the method of stationary phase. Define Φ to be the phase in equation (2.9), or

$$\Phi \equiv \omega_O \tau_O(\mathbf{x}, \xi_O) - \omega_I \tau_I(\mathbf{x}, \xi_I) . \quad (2.10)$$

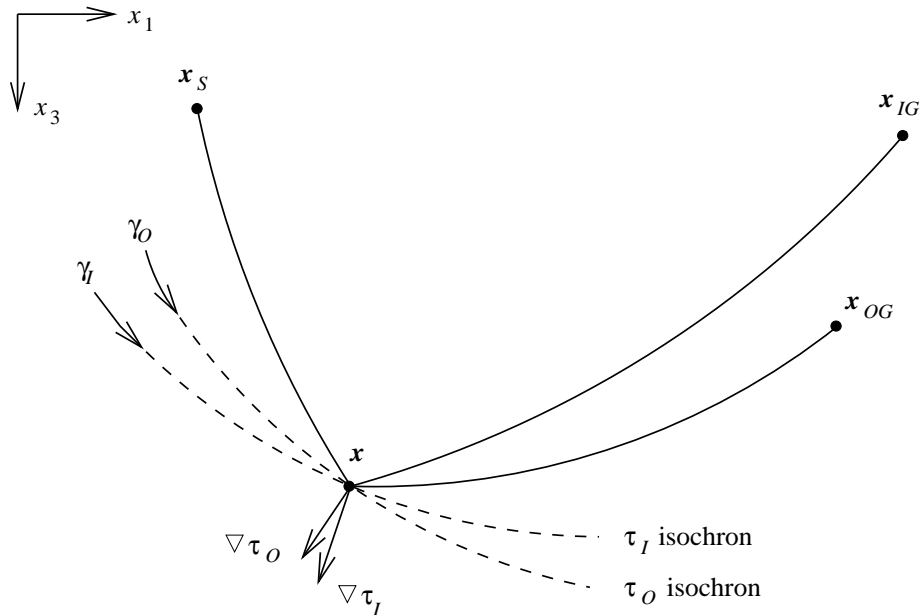


FIG. 2.1. 2D depth section showing the general geometry for downward continuation. Any depth point \mathbf{x} in the plane below the survey is expressed in coordinates (τ_I, γ_I) , referencing the traveltime isochron for the scattered raypath from the source to the input receiver.

The γ_I integration is an integration of \mathbf{x} along a particular input isochron, so that τ_I is constant with respect to differentiation over γ_I . Thus, stationarity is defined by the condition

$$\frac{\partial \Phi}{\partial \gamma_I} = \omega_O \frac{\partial \tau_O(\mathbf{x}, \xi_O)}{\partial \gamma_I} = \omega_O \frac{\partial \tau_O}{\partial x_i} \frac{\partial x_i}{\partial \gamma_I} = \omega_O \left(\nabla_{\mathbf{x}} \tau_O \cdot \frac{\partial \mathbf{x}}{\partial \gamma_I} \right) = 0, \quad (2.11)$$

where a summation over $i = 1, 3$ is assumed in the second result. Note that $\nabla_{\mathbf{x}} \tau_O$ is a vector normal to the τ_O isochron. Since \mathbf{x} is constrained to be on the τ_I isochron, ($\tau_I = \text{constant}$), in this integration, $\partial \mathbf{x} / \partial \gamma_I$ is, therefore, a vector that is tangent to the τ_I isochron. Then, equation (2.11) implies that stationarity occurs at all points where the dot product of these vectors is zero, that is, at all \mathbf{x} where the vectors are orthogonal.

This orthogonality occurs at all \mathbf{x} where the tangents of the isochrons τ_O and τ_I are collinear, or equivalently, where the gradients of these isochrons are collinear. For a given source, input, as well as output, receiver locations, assuming no multipathing, there is a unique \mathbf{x} on each τ_i isochron where this is true. For a fixed source, both the input and output configurations must therefore share the same ray from the source to \mathbf{x} . That is, with the isochrons tangent at \mathbf{x} , the scattered rays to the input and output receivers leave \mathbf{x} at the same angle, and therefore the ray from \mathbf{x} to \mathbf{x}_{OG} overlays the ray from \mathbf{x} to \mathbf{x}_{IG} . This means that stationarity occurs at all \mathbf{x} along the ray passing through both \mathbf{x}_{IG} and \mathbf{x}_{OG} , as shown in Figure 2.2.

An important feature of this result is that both the input and the output paths scatter at the same angle. Therefore, the angularly-dependent reflection coefficient is the same for both the input and output configurations. So, in this case, preservation of the input reflection coefficients in the output correctly maps the amplitude.²

With the source location fixed, and common to both the input and output geophone locations, the raypath from the source to the integration point \mathbf{x} at stationarity is the same path for both input and output. So, it follows that

$$\sigma_{OS} = \sigma_{IS} = \sigma_S , \quad (2.12)$$

and

$$\frac{A(\mathbf{x}, \mathbf{x}_{OS}(\xi_O))}{A(\mathbf{x}, \mathbf{x}_{IS}(\xi_I))} = \frac{\sqrt{\sigma_{OS}}}{\sqrt{\sigma_{IS}}} = 1 . \quad (2.13)$$

Also, along the stationary ray, the gradients of τ_I and τ_O are equal. So by the stationarity condition,

$$\frac{|\nabla_{\mathbf{x}}\tau_O(\mathbf{x}, \xi_O)|}{|\nabla_{\mathbf{x}}\tau_I(\mathbf{x}, \xi_I)|} = 1 . \quad (2.14)$$

Evaluation of the γ_I integration in equation (2.9) under the stationary phase condition therefore yields

$$\begin{aligned} u_O(\xi_O, \omega_O) &\approx \frac{\sqrt{2\pi}}{4\pi^2} \iiint \sqrt{\frac{|\omega_O|}{|\Phi''|}} e^{-i\pi/4 \operatorname{sgn}(\omega_O) + i\pi/4 \operatorname{sgn}(\Phi'')} \sqrt{|\omega_I|} e^{i\pi/4 \operatorname{sgn}(\omega_I)} \\ &\cdot u_I(\xi_I, \omega_I) \frac{A_O(\mathbf{x}_{OG}(\xi_O), \mathbf{x})}{A_I(\mathbf{x}_{IG}(\xi_I), \mathbf{x})} \frac{\sqrt{\sigma_S + \sigma_{IG}} \sqrt{\sigma_{OG}}}{\sqrt{\sigma_S + \sigma_{OG}} \sqrt{\sigma_{IG}}} |H(\mathbf{x}, \xi_I)| \\ &\cdot e^{(i\omega_O\tau_O(\mathbf{x}, \xi_O) - i\omega_I\tau_I(\mathbf{x}, \xi_I))} \left| \frac{\partial(\mathbf{x})}{\partial(\tau_I, \gamma_I)} \right| d\tau_I d\omega_I d\xi_I . \end{aligned} \quad (2.15)$$

The second derivative of the phase and the Jacobian remain to be evaluated. The second-derivative calculation is the same as in other data-mapping applications, and is derived in Bleistein & Jaramillo (1997, 1999). For the variables used in this discussion, the result is

$$\frac{\partial^2\Phi}{\partial\gamma_I^2} = \omega_O \frac{\cos^2\theta}{c(\mathbf{x})} \left(\frac{\partial s}{\partial\gamma_I} \right)^2 (\kappa_{OG} - \kappa_{IG}) , \quad (2.16)$$

where κ_{OG} and κ_{IG} are the magnitudes of the curvature vector associated with a wavefront emanating from a source at depth point \mathbf{x} and moving along the stationary ray, evaluated at the output and input receiver locations, respectively. This is depicted in Figure 2.3. The angle θ is half of the angle between the incoming ray from the

²Note that this result is a characteristic of the downward-continuation problem, and does not generally occur in data mapping.

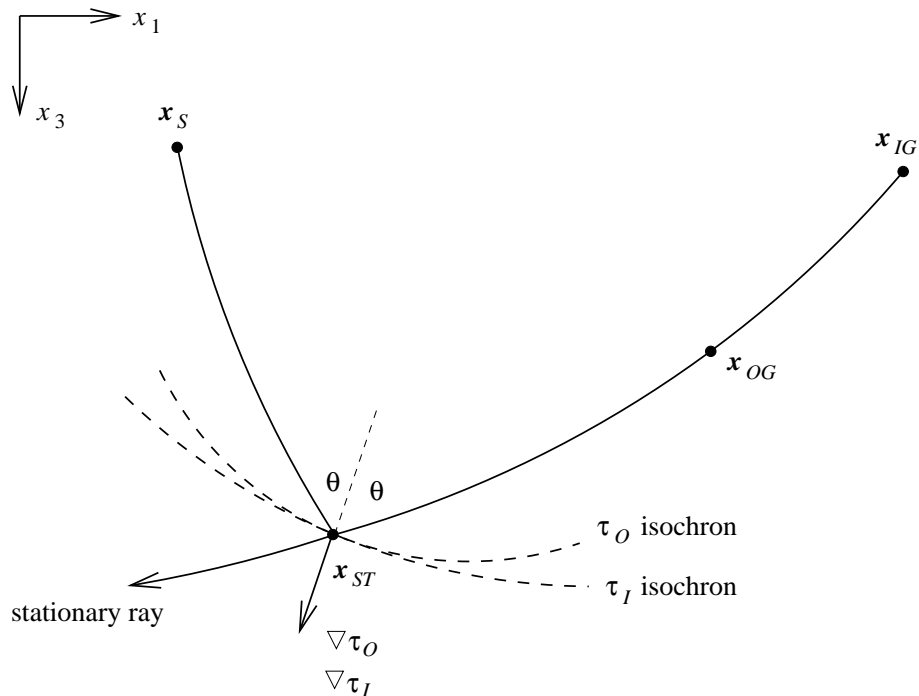


FIG. 2.2. 2D depth section showing the ray geometry at stationarity for the γ_I integration. All points in the survey plane along the ray through both \mathbf{x}_{IG} and \mathbf{x}_{OG} are stationary. The τ_I integration picks out a single stationary point on this ray, namely where it crosses the $\tau_O = t_O$ isochron.

source to \mathbf{x} , and the stationary ray from \mathbf{x} to the receiver locations, shown in Figure 2.2. Since γ_I is measured along the isochron, but is not necessarily equal to the arc length, s , the derivative $\partial s / \partial \gamma_I$ appears. From equation (2.16), the sign of the second derivative depends on that of frequency, as well as that of the difference in the curvatures.³

In the absence of wavespeed anomalies that result in lensing, the geometrical spreading of waves as they propagate away from their source guarantees that, given two wavefronts propagating along the same ray away from a common source, the wavefront that travels the longer distance along the ray always has the smaller curvature. The downward-continuation problem is defined by the condition that \mathbf{x}_{OG} be at a greater depth than \mathbf{x}_{IG} , so, for any point on the stationary ray beyond κ_{OG} , the path length from a scatterer to the datuming surface is always shorter than that to the recording surface, meaning $\kappa_{OG} > \kappa_{IG}$ and the difference of curvatures in (2.16) is always positive. Since stationary points between the datum and the recording surface generally represent energy scattered from features above the datum, which do not belong in the downward-continued data, the integral is evaluated for stationary points

³The curvature magnitudes κ_{OG} and κ_{IG} , as well as any other similarly defined curvatures hereafter, are pure magnitudes. That is, they are strictly nonnegative.

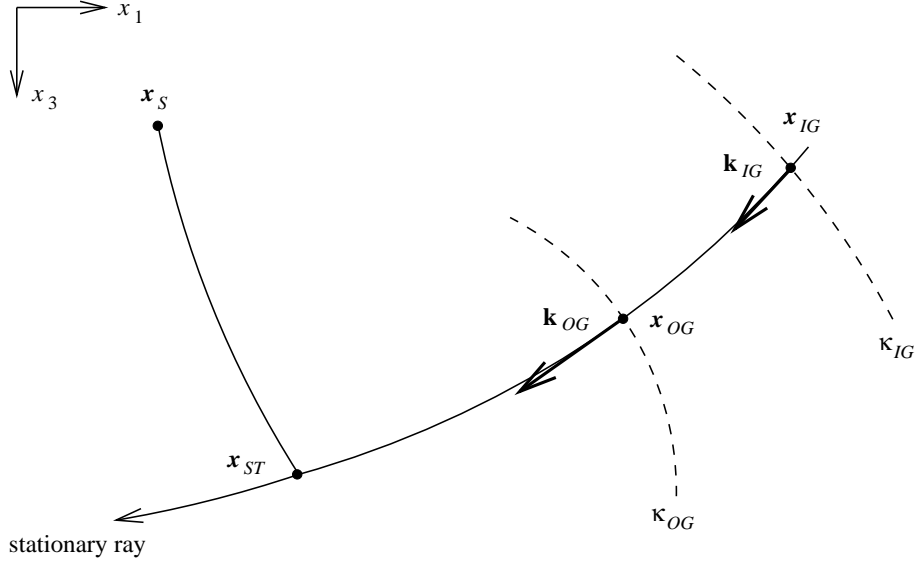


FIG. 2.3. 2D depth section depicting the definitions of the curvature magnitudes κ_{OG} and κ_{IG} , as the magnitudes of the curvature vectors \mathbf{k}_{OG} and \mathbf{k}_{IG} associated with the wavefronts at the output and input receiver locations, respectively. Alternatively, these can be viewed as wavefront curvatures at the stationary point \mathbf{x}_{ST} due to sources at \mathbf{x}_{IG} and \mathbf{x}_{OG} .

below \mathbf{x}_{OG} only, and the above condition holds. In general, wavespeed anomalies that change the sign of the curvature difference can occur along the stationary ray, between the recording and datuming surfaces. This, however, requires that the ray pass through a caustic. As previously noted, data-mapping expression (2.1) is based on the use of ray-theoretical Green's functions that assume no multipathing. Therefore, the results of the downward continuation are subject to the same restriction, and are not valid in the presence of a caustic. Under these limitations, $\kappa_{OG} > \kappa_{IG}$. Therefore,

$$\text{sgn}(\Phi'') = \text{sgn}(\omega_O) . \quad (2.17)$$

The expression for the Jacobian at stationarity is also the same as that in other data-mapping applications, and is derived in Bleistein & Jaramillo (1997, 1999). For the variables in this discussion, it is

$$\left| \frac{\partial(\mathbf{x})}{\partial(\tau_I, \gamma_I)} \right| = \frac{c(\mathbf{x})}{2 \cos \theta} \left| \frac{\partial s}{\partial \gamma_I} \right| . \quad (2.18)$$

So, using equations (2.16), (2.17), and (2.18), and assuming no caustics, the final form of integral (2.15) at stationarity becomes

$$u_O(\xi_O, \omega_O) \approx \frac{\sqrt{2\pi}}{8\pi^2} \iiint \frac{\sqrt{c^3(\mathbf{x}) |\omega_I|}}{\cos^2 \theta} e^{i\pi/4 \text{sgn}(\omega_I)} u_I(\xi_I, \omega_I) \frac{A_O(\mathbf{x}_{OG}(\xi_O), \mathbf{x})}{A_I(\mathbf{x}_{IG}(\xi_I), \mathbf{x})}$$

$$\begin{aligned}
& \cdot \frac{\sqrt{\sigma_S + \sigma_{IG}} \sqrt{\sigma_{OG}}}{\sqrt{\sigma_S + \sigma_{OG}} \sqrt{\sigma_{IG}}} \frac{|H(\mathbf{x}, \xi_I)|}{\sqrt{|\kappa_{OG} - \kappa_{IG}|}} e^{(i\omega_O \tau_O(\mathbf{x}, \xi_O) - i\omega_I \tau_I(\mathbf{x}, \xi_I))} \\
& \cdot d\tau_I d\omega_I d\xi_I .
\end{aligned} \tag{2.19}$$

Unlike the analogous result for the general data-mapping problem, the phase here is linear in τ_I , so stationary phase cannot be employed to evaluate the τ_I integral. However, an asymptotic approximation is unnecessary, since an exact evaluation of the integral can be performed. To do so, take the inverse Fourier transform of equation (2.19) from ω_O to the output time t_O . Since the only ω_O dependence is in the phase, a delta function results, giving

$$\begin{aligned}
u_O(\xi_O, t_O) & \approx \frac{\sqrt{2\pi}}{8\pi^2} \iiint \frac{\sqrt{c^3(\mathbf{x}) |\omega_I|}}{\cos^2\theta} e^{i\pi/4 \operatorname{sgn}(\omega_I)} u_I(\xi_I, \omega_I) \frac{A_O(\mathbf{x}_{OG}(\xi_O), \mathbf{x})}{A_I(\mathbf{x}_{IG}(\xi_I), \mathbf{x})} \\
& \cdot \frac{\sqrt{\sigma_S + \sigma_{IG}} \sqrt{\sigma_{OG}}}{\sqrt{\sigma_S + \sigma_{OG}} \sqrt{\sigma_{IG}}} \frac{|H(\mathbf{x}, \xi_I)|}{\sqrt{|\kappa_{OG} - \kappa_{IG}|}} e^{-i\omega_I \tau_I(\mathbf{x}, \xi_I)} \delta(t_O - \tau_O(\mathbf{x}, \xi_O)) \\
& \cdot d\tau_I d\omega_I d\xi_I .
\end{aligned} \tag{2.20}$$

At stationarity, the gradients of the input and output isochrons are equal, so the integration in equation (2.20) over τ_I is transformed to an integral over τ_O by simply making the substitution $d\tau_I = d\tau_O$. Using the sifting property of the delta function, the integration is straightforward, yielding the result,

$$\begin{aligned}
u_O(\xi_O, t_O) & \approx \frac{\sqrt{2\pi}}{8\pi^2} \iint \frac{\sqrt{c^3(\mathbf{x}) |\omega_I|}}{\cos^2\theta} e^{i\pi/4 \operatorname{sgn}(\omega_I)} u_I(\xi_I, \omega_I) \frac{A_O(\mathbf{x}_{OG}(\xi_O), \mathbf{x})}{A_I(\mathbf{x}_{IG}(\xi_I), \mathbf{x})} \\
& \cdot \frac{\sqrt{\sigma_S + \sigma_{IG}} \sqrt{\sigma_{OG}}}{\sqrt{\sigma_S + \sigma_{OG}} \sqrt{\sigma_{IG}}} \frac{|H(\mathbf{x}, \xi_I)|}{\sqrt{|\kappa_{OG} - \kappa_{IG}|}} e^{-i\omega_I \tau_I(\mathbf{x}, \xi_I)} d\omega_I d\xi_I ,
\end{aligned} \tag{2.21}$$

evaluated at the point \mathbf{x} on the stationary ray where

$$\tau_O(\mathbf{x}, \xi_O) = t_O . \tag{2.22}$$

Note that integration over the delta function has chosen a single stationary point on what could previously be constrained to only a stationary ray. Equation (2.21), however, still contains the isochron value τ_I in the phase. With condition (2.22), though, τ_I is determined, given the traveltimes τ_{IO} along the stationary ray from \mathbf{x}_{OG} to \mathbf{x}_{IG} . Thus, τ_I is evaluated using

$$\tau_I(\mathbf{x}, \xi_I) = \tau_O(\mathbf{x}, \xi_O) + \tau_{IO}(\mathbf{x}_{IG}, \mathbf{x}_{OG}) = t_O + \tau_{IO}(\mathbf{x}_{IG}, \mathbf{x}_{OG}) . \tag{2.23}$$

Two additional simplifications to equation (2.21) that are a result of the 2.5D dimensionality are derived in Bleistein, et al. (1997), which shows that

$$|H(\mathbf{x}, \xi_I)| = \frac{2\cos^2\theta}{c(\mathbf{x})} \left| \frac{\partial}{\partial \xi_I} \nabla_{\mathbf{x}} \tau_{IG} \right|, \quad (2.24)$$

where the gradient is that of the traveltime to the input receiver location, and

$$|A(\mathbf{x}_O, \mathbf{x})| = \frac{\text{constant}}{\sqrt{\sigma_O} |J(\mathbf{x}_O, \mathbf{x})|}, \quad (2.25)$$

where $|J(\mathbf{x}_O, \mathbf{x})|$ is the Jacobian of transformation between the receiver location \mathbf{x}_O and the depth point \mathbf{x} , and σ_O is as previously defined in equation (2.5), along the path between \mathbf{x}_O and \mathbf{x} .

Finally, the 2.5D downward continuation of receivers is performed via the integral expression,

$$u_O(\xi_O, t_O) \approx \frac{1}{\sqrt{2\pi}} \int \frac{\sqrt{c(\mathbf{x})}}{\sqrt{|\kappa_{OG} - \kappa_{IG}|}} \frac{\sqrt{|J(\mathbf{x}_{IG}, \mathbf{x})|}}{\sqrt{|J(\mathbf{x}_{OG}, \mathbf{x})|}} \frac{\sqrt{\sigma_S + \sigma_{IG}}}{\sqrt{\sigma_S + \sigma_{OG}}} \cdot \left| \frac{\partial \nabla_{\mathbf{x}} \tau_{IG}}{\partial \xi_I} \right| D_f(\xi_I, \tau_I(\mathbf{x}, \xi_I)) d\xi_I, \quad (2.26)$$

where

$$D_f(\xi_I, t) \equiv \frac{1}{2\pi} \int \sqrt{|\omega_I|} u_I(\xi_I, \omega_I) e^{-i\omega_I t + i\pi/4 \operatorname{sgn}(\omega_I)} d\omega_I. \quad (2.27)$$

D_f is a frequency-domain filter on the input data that reverses phase distortions associated with wave propagation between the output and input receiver locations. The entire integration is evaluated at the depth point \mathbf{x} , which is the point where the raypath connecting both the input and output receiver locations intersects the isochron given by

$$\tau_I(\mathbf{x}, \xi_I) = t_O + \tau_{IO}(\mathbf{x}_{IG}(\xi_I), \mathbf{x}_{OG}). \quad (2.28)$$

Note that the data-mapping integral (2.26) depends on quantities that are evaluated along raypaths through stationary points below the output surface. This is not typical of other downward-continuation methods, which generally require only knowledge of wave propagation between the input and output surfaces. This difference is addressed further in Chapter 6.

2.3 Downward continuation of sources

The same derivation can be performed for the mapping of source locations in the case of a fixed receiver (common-receiver gather). Recasting the previous derivation in terms of sources, where η_I and η_O are parameters describing the lateral coordinate

of the input and output source locations given a fixed receiver location, the expression analogous to equation (2.26) is

$$u_O(\eta_O, t_O) \approx \frac{1}{\sqrt{2\pi}} \int \frac{\sqrt{c(\mathbf{x})}}{\sqrt{|\kappa_{OS} - \kappa_{IS}|}} \frac{\sqrt{|J(\mathbf{x}_{IS}, \mathbf{x})|}}{\sqrt{|J(\mathbf{x}_{OS}, \mathbf{x})|}} \frac{\sqrt{\sigma_G + \sigma_{IS}}}{\sqrt{\sigma_G + \sigma_{OS}}} \cdot \left| \frac{\partial \nabla_{\mathbf{x}} \tau_{IS}}{\partial \eta_I} \right| D_s(\eta_I, \tau_I(\mathbf{x}, \eta_I)) d\eta_I, \quad (2.29)$$

where

$$D_s(\eta_I, t) \equiv \frac{1}{2\pi} \int \sqrt{|\omega_I|} u_I(\eta_I, \omega_I) e^{-i\omega_I t + i\pi/4 \text{sgn}(\omega_I)} d\omega_I. \quad (2.30)$$

Here, D_s is a frequency-domain filter on the input data that corrects phase distortions associated with wave propagation between the input and output source locations. The integration is evaluated at the depth point \mathbf{x} defined as the point of intersection between the raypath connecting the source locations and the isochron

$$\tau_I(\mathbf{x}, \eta_I) = t_O + \tau_{IO}(\mathbf{x}_{IS}(\eta_I), \mathbf{x}_{OS}). \quad (2.31)$$

The geometry of the problem is analogous to that shown in Figure 2.2, under the interchange of the roles of source and receiver, such that the stationary ray is now traced through \mathbf{x}_{IS} and \mathbf{x}_{OS} . Again, factors in equation (2.29) are evaluated along raypaths through stationary points below the output surface, which is not typical of other downward-continuation methods.

This is a general result, but it is essential to recognize that in practice the receiver and source extrapolations are a cascaded process, so care must be taken in implementation of the second process to account for the fact that part of the data has already been downward continued. Traveltimes, as well as quantities that are evaluated with respect to the relevant raypaths connecting the source and receiver locations, differ depending on whether the sources or receivers are on the recording surface, or have already been extrapolated to the datum. For example, if receivers are downward continued first, then the second step of extrapolating the sources must account for the fact that the receivers are on the datum, not the original recording surface. Failure to do so evaluates the integral for the wrong raypaths, and produces an erroneous result.

2.4 Implementation in general media

In evaluation of the above integrals, only the desired output time, the input and output geometries, and the wavespeed model, are assumed known initially. To obtain the correct kinematics, ray tracing between the recording and datuming surfaces can be used to provide τ_{IO} , and therefore τ_I , giving accurate traveltimes and phase. Evaluation of the amplitude factors, however, requires determination of the

isochrons and rays so that the stationary points can be located, and the relevant ray-paths, Jacobians, curvatures, and ray parameters can be calculated. Given what is assumed known initially, this is accomplished in general, heterogeneous media only by extensive application of ray tracing. Since these factors must be calculated for every input-output configuration at every output time, this process is generally expensive computationally, especially in complex models where no specific analytic results or *a priori* information about the ray geometry is available to be incorporated into the process. It is likely that computation in depth-dependent, or $v(z)$, media can be made reasonably efficient, as in the case of $v(z)$ dip-moveout processing (DMO), which is a similar process. Implementation in more heterogeneous wavespeed models, however, seems impractical at this time given current computational limitations.

Chapter 3

CONSTANT-WAVESPEED MEDIA

Implementation of the downward continuation formula developed in Chapter 2 is problematic in general media because no simplifying assumptions can be made about the isochron or ray geometries. In constant-wavespeed media, these geometries are known, and, as is shown in this discussion, analytic expressions for the coordinates of the stationary point, as well as for the relevant ray quantities required to evaluate the downward continuation integrals, are possible. While homogeneous wavespeed models may not be representative of the actual propagation media of field data, they are still important initial cases for study. Many commonly used data processing methods assume constant wavespeed for amplitude determination, and a direct comparison with the data-mapping result under the same assumption is valuable for understanding when and how it should be used. More important, simple, constant-wavespeed models provide insights into the abilities and limitations of the method.

3.1 Receiver continuation in a constant-wavespeed medium

In a constant-wavespeed medium, many of the factors in the integral expression (2.26) simplify. Assuming an arbitrary recording surface, let the source and receiver locations be given by

$$\mathbf{x}_{IG} = (\xi_I, z_I) , \quad \mathbf{x}_{OG} = (\xi_O, z_O) , \quad \mathbf{x}_S = (x_S, z_S) , \quad (3.1)$$

and define the location of each stationary point as

$$\mathbf{x} = (\bar{x}_1, \bar{x}_3) . \quad (3.2)$$

As shown in Figure 3.1, rays are straight and isochrons are ellipses, tilted with respect to the coordinate system such that the source and the appropriate receiver location are at the foci. As a result, analytic expressions are possible for the location of the stationary point that are functions of only the source and receiver locations and the traveltime.

In a constant-wavespeed medium, the σ -factors are rc , where r is path length, and c is again wavespeed. Jacobians of the form $|J(\mathbf{x}_G, \mathbf{x})|$ describe the transformation between the receiver location \mathbf{x}_G and the depth point \mathbf{x} . At stationarity, in homogeneous media, these are equal to the lengths of straight paths connecting the given points, or

$$|J(\mathbf{x}_{IG}, \mathbf{x})| = r_{IG} = \sqrt{(\bar{x}_1 - \xi_I)^2 + (\bar{x}_3 - z_I)^2} , \quad (3.3)$$

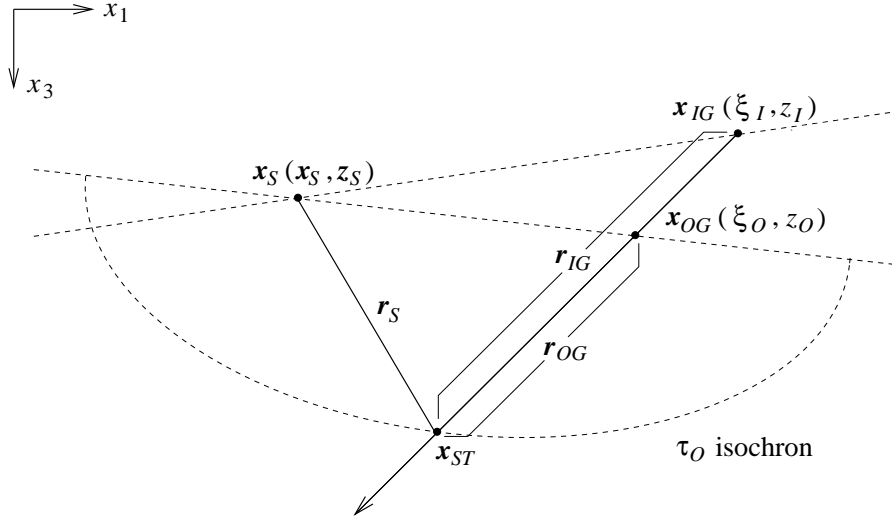


FIG. 3.1. 2D depth section showing the geometry for receiver continuation in a constant-wavespeed medium.

$$|J(\mathbf{x}_{OG}, \mathbf{x})| = r_{OG} = \sqrt{(\bar{x}_1 - \xi_I)^2 + (\bar{x}_3 - z_O)^2}. \quad (3.4)$$

For homogeneous media, the radii of curvature of the wavefronts emitted from \mathbf{x} and arriving at the input and output locations along the stationary ray are simply the distances between the points, and the wavefronts are spherical, so that

$$\frac{1}{\kappa_{IG}} = r_{IG} = \frac{\sigma_{IG}}{c}, \quad \frac{1}{\kappa_{OG}} = r_{OG} = \frac{\sigma_{OG}}{c}. \quad (3.5)$$

Finally, the gradient of the scattered traveltime, $\nabla_{\mathbf{x}}\tau_{IG}$, is a vector pointing in the direction of r_{IG} with magnitude $1/c$. In Appendix A, its derivative is shown to be

$$\left| \frac{\partial \nabla_{\mathbf{x}}\tau_{IG}}{\partial \xi_I} \right| = \frac{G(\bar{x}_1, \bar{x}_3)}{c r_{IG}^2}, \quad (3.6)$$

where G is a factor that contains the influence of topographic variations in the recording surface, given by the expression

$$G(\bar{x}_1, \bar{x}_3) \equiv \left| (\bar{x}_3 - z_I) - (\bar{x}_1 - \xi_I) \frac{\partial z_I}{\partial \xi_I} \right|. \quad (3.7)$$

These results allow equation (2.26) to be written as

$$u_O(\xi_O, t_O) \approx \frac{1}{\sqrt{2\pi c}} \int d\xi_I \frac{G(\bar{x}_1, \bar{x}_3)}{r_{IG}} \frac{\sqrt{r_S + r_{IG}}}{\sqrt{r_S + r_{OG}}} \frac{D_f(\xi_I, \tau_I(\mathbf{x}, \xi_I))}{\sqrt{|r_{IG} - r_{OG}|}}, \quad (3.8)$$

where

$$D_f(\xi_I, t) \equiv \frac{1}{2\pi} \int \sqrt{|\omega_I|} u_I(\xi_I, \omega_I) e^{-i\omega_I t + i\pi/4 \operatorname{sgn}(\omega_I)} d\omega_I . \quad (3.9)$$

The integral still contains functions of the stationary point, which requires determination of the location of \mathbf{x} . As previously described, this point lies at the intersection of the ray through \mathbf{x}_{IG} and \mathbf{x}_{OG} and the output isochron $\tau_O = t_O$, or equivalently, with the input isochron $\tau_I = t_O + \tau_{IO}$, where τ_{IO} is independently determined.

In the general derivation, it was noted that under the assumption of no caustics, downward continuation requires that the stationary point must always be below the datum. In the constant-wavespeed case, this is equivalent to the condition

$$r_{IG} > r_{OG} . \quad (3.10)$$

Since values of t_O exist that violate this condition when evaluating the integral (3.8) over all output times, requirement (3.10) must be applied. Not only does this exclude scattered energy associated with features above the datum, but it also avoids the singularity due to $\sqrt{|r_{IG} - r_{OG}|}$ in the denominator.

In fact, a more stringent condition arises from the use of leading-order stationary phase, which sets a minimum on all relevant length scales in the problem. The proximity of the input and output receiver locations, or equivalently, the difference in depth between points on the recording and datuming surfaces, is one of these length scales. Therefore, an asymptotic validity condition sets a lower bound on acceptable values of $r_{IG} - r_{OG}$. These validity conditions are discussed later in this study.

3.2 Location of the stationary point for receiver continuation

The geometry shown in Figure 3.1 allows the derivation of analytic expressions for the location of the stationary point by considering the tilted ellipse of the τ_O isochron and the straight ray between the input and output locations. To facilitate the calculation for any general set of source and receiver locations placed on arbitrary recording and datuming surfaces, proceed as follows: For every combination of source and input-output receiver locations,

1. shift the origin in both coordinate directions to the source location (x_S, z_S) ;
2. rotate the coordinate axes about the new origin so that the new horizontal axis is coincident with the major axis of the τ_O ellipse;
3. calculate the location of the stationary point and the required paths in the rotated coordinates.

The shift-rotation is expressed in terms of the rotation angle and the primed quantities,

$$x_S' = 0 , \quad z_S' = 0 , \quad z_O' = 0 , \quad (3.11)$$

$$\varphi = \tan^{-1} \left(\frac{z_O - z_S}{\xi_O - x_S} \right), \quad (3.12)$$

$$\xi_O' = (\xi_O - x_S) \cos \varphi + (z_O - z_S) \sin \varphi, \quad (3.13)$$

$$\xi_I' = (\xi_I - x_S) \cos \varphi + (z_I - z_S) \sin \varphi, \quad (3.14)$$

$$z_I' = -(\xi_I - x_S) \sin \varphi + (z_I - z_S) \cos \varphi, \quad (3.15)$$

$$h' = \frac{\xi_O'}{2}. \quad (3.16)$$

Given this change in reference, the major axis of the ellipse representing the τ_O isochron is aligned with the x_1' -axis. It is centered at $x_1' = h'$, with h' being the signed half-offset between the source and the output receiver location in the primed coordinate frame. From the general derivation, $\tau_O = t_O$, and using these facts, the ellipse is defined by the equation

$$x_3'^2 = Q \left[(ct_O)^2 - 4(x_1' - h')^2 \right], \quad (3.17)$$

where

$$Q \equiv \frac{(ct_O)^2 - 4h'^2}{4(ct_O)^2}. \quad (3.18)$$

The stationary ray is the line through \mathbf{x}_{IG} and \mathbf{x}_{OG} , and is described by

$$x_1' = \left(\frac{\xi_I' - \xi_O'}{z_I'} \right) x_3' + \xi_O'. \quad (3.19)$$

The stationary point is one of the two intersections of these two curves. In our case of a straight ray that crosses the major axis of the ellipse, these two points are distinguished by the fact that one must lie above the $x_3' = 0$ surface, the other below. Because this construction exists only in the $x_3' > 0$ half-space, the simplest approach to the problem is to solve equations (3.17) and (3.19) for x_3' , then choose only the positive solution. After some algebra, this produces

$$\bar{x}_3' = \sqrt{S + P^2} - P, \quad (3.20)$$

where

$$S \equiv \frac{Q \left((ct_O)^2 - \xi_O'^2 \right) z_I'^2}{z_I'^2 + 4Q \left(\xi_I' - \xi_O' \right)^2}, \quad (3.21)$$

and

$$P \equiv \frac{2Q (\xi_I' - \xi_O') \xi_O' z_I'}{z_I'^2 + 4Q (\xi_I' - \xi_O')^2}, \quad (3.22)$$

with Q defined in equation (3.18). Equation (3.20) produces a value that is both positive and real, since, by the problem geometry, S is always positive.

Now, \bar{x}_1' is easily found using this result and either equation (3.17) or (3.19). Since rotation of the coordinate system does not change the path lengths between the source and receiver locations and the stationary point, these lengths are calculated directly in the primed coordinates using

$$r_S = r_S' = \sqrt{\bar{x}_1'^2 + \bar{x}_3'^2}, \quad (3.23)$$

$$r_{OG} = r_{OG}' = \sqrt{(\bar{x}_1' - \xi_O')^2 + \bar{x}_3'^2}, \quad (3.24)$$

$$r_{IG} = r_{IG}' = \sqrt{(\bar{x}_1' - \xi_I')^2 + (\bar{x}_3' - z_I')^2}. \quad (3.25)$$

To evaluate the depth coordinates of the stationary point appearing in the integral, rotate the depth in the primed coordinates back to the unprimed frame, and undo the shift, via

$$\bar{x}_1 = \bar{x}_1' \cos \varphi - \bar{x}_3' \sin \varphi + x_S, \quad (3.26)$$

$$\bar{x}_3 = \bar{x}_1' \sin \varphi + \bar{x}_3' \cos \varphi + z_S. \quad (3.27)$$

3.3 Receiver continuation from a horizontal surface

The above discussion is applicable to data collected on any arbitrary recording surface. If data are collected on a horizontal recording surface, however, several simplifications are possible. Define the flat surface by letting

$$z_I = \frac{\partial z_I}{\partial \xi_I} = 0. \quad (3.28)$$

Given this, equation (3.7) becomes simply

$$G(\bar{x}_1, \bar{x}_3) = \bar{x}_3, \quad (3.29)$$

making the integral for a horizontal recording surface,

$$u_O(\xi_O, t_O) \approx \frac{1}{\sqrt{2\pi c}} \int d\xi_I \frac{\bar{x}_3}{r_{IG}} \frac{\sqrt{r_S + r_{IG}}}{\sqrt{r_S + r_{OG}}} \frac{D_f(\xi_I, \tau_I(\mathbf{x}, \xi_I))}{\sqrt{|r_{IG} - r_{OG}|}}. \quad (3.30)$$

Stationary point locations and path lengths required for evaluation of equation (3.30) are found using the same procedure as described above for the topographic case, that is, using equations (3.11) through (3.27).

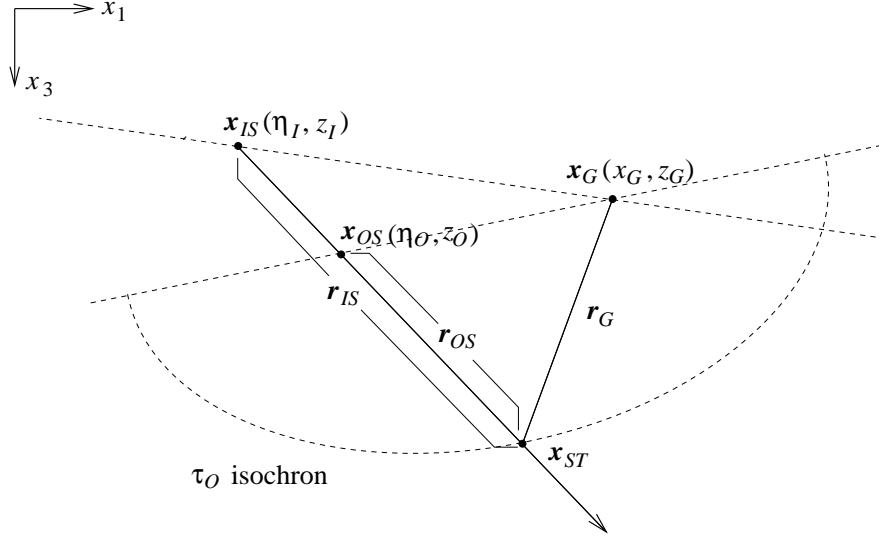


FIG. 3.2. 2D depth section showing the geometry for source continuation in a constant-wavespeed medium.

3.4 Source continuation in a constant-wavespeed medium

The process of downward continuation of both sources and receivers is completed by implementing a source continuation in a constant-wavespeed medium. This derivation parallels that for receiver continuation, where the roles of the source and receiver locations are interchanged. So, define

$$\mathbf{x}_{IS} = (\eta_I, z_I) , \quad \mathbf{x}_{OS} = (\eta_O, z_O) , \quad \mathbf{x}_G = (x_G, z_G) . \quad (3.31)$$

The resulting geometry is shown in Figure 3.2.

Applying simplifications analogous to those for receiver continuation to the general integral (2.29), gives the constant-wavespeed expression

$$u_O(\eta_O, t_O) \approx \frac{1}{\sqrt{2\pi c}} \int d\eta_I \frac{G(\bar{x}_1, \bar{x}_3)}{r_{IS}} \frac{\sqrt{r_G + r_{IS}}}{\sqrt{r_G + r_{OS}}} \frac{D_s(\eta_I, \tau_I(\mathbf{x}, \eta_I))}{\sqrt{|r_{IS} - r_{OS}|}} , \quad (3.32)$$

where

$$D_s(\eta_I, t) \equiv \frac{1}{2\pi} \int \sqrt{|\omega_I|} u_I(\eta_I, \omega_I) e^{-i\omega_I t + i\pi/4 \text{sgn}(\omega_I)} d\omega_I . \quad (3.33)$$

The factor containing the topographic variation in the survey surface is

$$G(\bar{x}_1, \bar{x}_3) \equiv \left| (\bar{x}_3 - z_I) - (\bar{x}_1 - \eta_I) \frac{\partial z_I}{\partial \eta_I} \right| . \quad (3.34)$$

As for the receiver case, the integral contains factors that depend on knowing the location of the stationary point, \mathbf{x} . Equation (3.32) is also subject to the same

validity conditions as for expression (3.8), and under the assumption of no caustics, the condition analogous to requirement (3.10) in this case is

$$r_{IS} > r_{OS} . \quad (3.35)$$

As before, this condition eliminates scattered energy in the input data that should not appear in the downward-continued data. As in the case of receiver continuation, a more stringent validity condition arising from leading-order asymptotics sets a lower bound on $r_{IS} - r_{OS}$, as it is a relevant length scale in the problem. These asymptotic validity conditions are discussed further in Chapter 5.

3.5 Location of the stationary point for source continuation

Analytic expressions for the location of the stationary point in source continuation are analogous to those for the receiver continuation, and follow the geometry outlined in Figure 3.2. The same type of shift-rotation is performed for each set of source and receiver locations, into a coordinate system aligned with the axes of the τ_O isochron. This time, however, the origin is shifted to the common-receiver location, (x_G, z_G) . As expected, the results are those of the receiver continuation, above, with the roles of the source and receiver locations interchanged. Using definitions (3.31), the shift-rotation is expressed in terms of the rotation angle and the primed quantities,

$$x_G' = 0 , \quad z_G' = 0 , \quad z_O' = 0 , \quad (3.36)$$

$$\varphi = \tan^{-1} \left(\frac{z_O - z_G}{\eta_O - x_G} \right) , \quad (3.37)$$

$$\eta_O' = (\eta_O - x_G) \cos \varphi + (z_O - z_G) \sin \varphi , \quad (3.38)$$

$$\eta_I' = (\eta_I - x_G) \cos \varphi + (z_I - z_G) \sin \varphi , \quad (3.39)$$

$$z_I' = -(\eta_I - x_G) \sin \varphi + (z_I - z_G) \cos \varphi , \quad (3.40)$$

$$h' = \frac{\eta_O'}{2} , \quad (3.41)$$

As before, this change in reference means the major axis of the ellipse representing the τ_O isochron is aligned with the x_1' -axis. It is centered at $x_1' = h'$, as h' is the signed half-offset between the common-receiver location and the output source location in the primed frame. Again, use the fact that $\tau_O = t_O$. The equation of the ellipse is the same as in the previous case,

$$x_3'^2 = Q \left[(ct_O)^2 - 4 (x_1' - h')^2 \right] , \quad (3.42)$$

where

$$Q \equiv \frac{(ct_O)^2 - 4h'^2}{4(ct_O)^2}, \quad (3.43)$$

but interpreted under the source-continuation geometry. The stationary ray is the line through \mathbf{x}_{IS} and \mathbf{x}_{OS} , and is described by

$$x_1' = \left(\frac{\eta_I' - \eta_O'}{z_I'} \right) x_3' + \eta_O'. \quad (3.44)$$

As before, the stationary point is the intersection of these two curves in the $x_3' > 0$ half-space. This produces the solution

$$\bar{x}_3' = \sqrt{S + P^2} - P, \quad (3.45)$$

where

$$S \equiv \frac{Q \left((ct_O)^2 - \eta_O'^2 \right) z_I'^2}{z_I'^2 + 4Q (\eta_I' - \eta_O')^2}, \quad (3.46)$$

and

$$P \equiv \frac{2Q (\eta_I' - \eta_O') \eta_O' z_I'}{z_I'^2 + 4Q (\eta_I' - \eta_O')^2}, \quad (3.47)$$

where, again, the result in equation (3.45) is real and positive since S is always positive. \bar{x}_1' is easily found using this result and either equations (3.42) or equation (3.44), and the path lengths are computed in the primed coordinates using

$$r_G = r_G' = \sqrt{\bar{x}_1'^2 + \bar{x}_3'^2}, \quad (3.48)$$

$$r_{OS} = r_{OS}' = \sqrt{(\bar{x}_1' - \eta_O')^2 + \bar{x}_3'^2}, \quad (3.49)$$

$$r_{IS} = r_{IS}' = \sqrt{(\bar{x}_1' - \eta_I')^2 + (\bar{x}_3' - z_I')^2}. \quad (3.50)$$

Rotating back to the unprimed frame and reversing the shift, the depth coordinates of the stationary point appearing in the integral are determined via

$$\bar{x}_1 = \bar{x}_1' \cos \varphi - \bar{x}_3' \sin \varphi + x_G, \quad (3.51)$$

$$\bar{x}_3 = \bar{x}_1' \sin \varphi + \bar{x}_3' \cos \varphi + z_G. \quad (3.52)$$

3.6 Source continuation from a horizontal surface

Assuming a horizontal recording surface,

$$z_I = \frac{\partial z_I}{\partial \eta_I} = 0, \quad (3.53)$$

the topographic factor G is, as before,

$$G(\bar{x}_1, \bar{x}_3) = \bar{x}_3, \quad (3.54)$$

making the integral for a horizontal recording surface,

$$u_O(\eta_O, t_O) \approx \frac{1}{\sqrt{2\pi c}} \int d\eta_I \frac{\bar{x}_3}{r_{IS}} \frac{\sqrt{r_G + r_{IS}}}{\sqrt{r_G + r_{OS}}} \frac{D_s(\eta_I, \tau_I(\mathbf{x}, \eta_I))}{\sqrt{|r_{IS} - r_{OS}|}}. \quad (3.55)$$

Stationary-point locations and path lengths required for evaluation of equation (3.55) are found using the same procedure as described above for the topographic case, that is, using equations (3.36) through (3.52).

3.7 Implementation options for constant-wavespeed media

While the assumption of constant wavespeed is not generally representative of the propagation medium of field data, the case is not purely illustrative. Obtaining the correct kinematics, even in heterogeneous media, is a matter of obtaining the correct values for τ_{IO} , as previously noted, by ray-tracing between the recording surface and the datum. Given this, an implementation that is kinematically correct, but uses a constant-wavespeed assumption for the dynamics, is possible. This involves using the constant-wavespeed form of the integral where all path lengths appearing in the amplitude weighting factors are approximated by straight rays, but where τ_I in the phase is determined using ray-traced values for τ_{IO} . This type of approximation is commonly applied to Kirchhoff methods of downward continuation and migration, in practice, for situations where true-amplitudes are not of primary importance.

Since the data-mapping method involves the same basic integrations as in other Kirchhoff approaches to the same problem, the same computational cost is incurred by using it as opposed to other, similar methods. Therefore, the constant-wavespeed version of the data-mapping process is a possible alternative to other Kirchhoff dating methods for processing kinematic data. The data-mapping algorithm also has the feature that it may be upgraded at a later time to evaluate amplitudes under the assumption of more complex wavespeed models, because the integral expression for heterogeneous media is already derived in this study.

As in other Kirchhoff approaches, an algorithm based on the data-mapping method may be modified for application to horizontally layered media with no significant lateral wavespeed variations, through the use of root-mean-square velocities above each stationary point. This allows the use of the straight-ray approximation in a somewhat more complicated medium.

Chapter 4

BASIC SYNTHETIC MODELS

Downward continuation of various synthetic data sets by the data-mapping process, via computer codes that implement equation (3.8) for receiver continuation under the assumption of a constant-wavespeed medium, provides some insight into the features of the method. In these codes, stationary points and path lengths are calculated using the analytic schemes previously described for homogeneous media. All codes used here were developed by the author, and are implemented as part of the Seismic Unix (SU) processing suite, maintained by the Center for Wave Phenomena, at the Colorado School of Mines.

Synthetic data examples involving both horizontal and irregular recording and reflecting surfaces illustrate general features and accuracy of the output data. In this discussion, only the results of the downward continuation of receivers to a horizontal datum for a single fixed source are given, since the continuation of sources is simply the same process under the interchange of sources and receivers. That is, the demonstration of the ability to downward continue receivers shows the validity of the process for source continuation as well. Schematically, this process is depicted in Figure 4.1.

Since a detailed study of kinematic issues in datuming with Kirchhoff methods is presented in Salinas (1997), the following discussion focuses primarily on the dynamic calculation, and the ability of the data-mapping method to preserve amplitude, at least in the sense that the amplitude calculation is correct with respect to the wavespeed model employed in the downward-continuation process.

4.1 Horizontal reflector and a horizontal recording surface

Consider the most basic datuming problem. Given a common-source gather, collected on a horizontal recording surface over a single horizontal reflector, receivers are downward continued to a horizontal datum below the surface.

The common-source data are assumed to be collected on a horizontal recording surface where there are 201 receivers, starting at zero offset and spaced 12.5 m apart. The horizontal reflector is at 1500-m depth, and the wavelet in the data has a peak frequency of 20 Hz. Downward continuation of the receivers is performed such that the data are extrapolated to a horizontal output datum with the same lateral positions of receivers as those on the input surface. The subsurface model is given in Figure 4.2, where the wavespeed between the recording surface and the reflector is a constant 2000 m/s. The data were generated analytically, by placing a wavelet centered at the proper traveltimes on each trace, with a peak amplitude consistent with 3D geometrical spreading along the travel path. The 3D amplitudes are accurately mapped in the

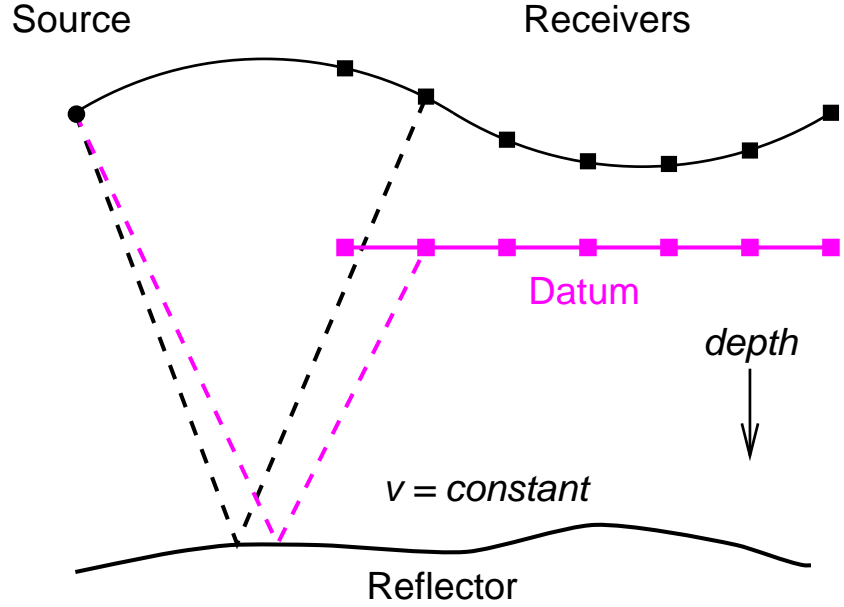


FIG. 4.1. 2D depth section schematically depicting the downward continuation of receivers to a horizontal datum in a constant-wavespeed medium.

2.5D process, so the same analytic data-generation procedure is used to calculate comparison amplitudes for the datum level.

Figure 4.3 shows synthetic, common-source data generated with receivers on the input surface, as well as on three horizontal datum levels at depths of 200 m, 500 m, and 800 m below the source. These depths are equivalent to roughly 13%, 34%, and 53% of the reflector depth below the source. Figure 4.4 shows the same input data and the results of the downward continuation of these data to the three datum levels via the data-mapping algorithm.

Direct comparison of Figures 4.3 and 4.4 show that the data-mapping calculation is kinematically accurate over a range of offsets interior to the ends of the spread. Outside of this range, edge effects begin to dominate. Amplitudes appear incorrect near the ends of the spread, as well, and the range of accurate data decreases as the datum moves closer to the reflector. Also note the weak artifacts that cross above the primary reflection. These arise from the endpoints of integration for the finite-aperture data, a topic that is discussed later.

Figure 4.5 shows plots of amplitude versus offset for the three downward-continued time sections. In each panel, the black curve shows peak amplitude from the data-mapping result, the grey curve shows peak amplitude from the synthetic data, to show the correct amplitudes on the desired datum, and the light grey dotted curve shows the peak amplitude in the input data. Clearly, the data-mapping results and the analytic comparison data match well over the offsets within a depth-dependent aperture. At each end of the aperture, the amplitude rises slightly due to constructive interference with the artifacts noted above. The range of offsets where the amplitudes

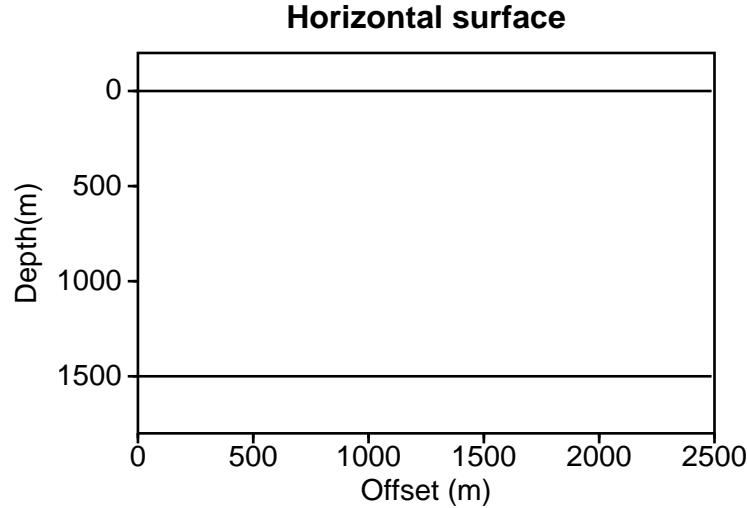


FIG. 4.2. 2D depth section showing a subsurface model with a horizontal recording surface and horizontal reflector in a constant-wavespeed medium.

are accurate will be referred to as the *useful aperture*.

Note that the width of the useful aperture decreases as the datum is moved closer to the reflector. Where the datuming depth is small compared to the depth of the target reflectors, this may not be a large problem. However, where the datum must be evaluated at depths that are significant percentages of the target depth, the range of useful amplitudes may be noticeably restricted. This problem results from finite data aperture, and is discussed in detail later.

4.2 Horizontal reflector and a topographic recording surface

Next, consider the problem of a common-source survey carried out over a horizontal reflector, again with a 20-Hz wavelet, but with a recording surface that is not horizontal.

In this model, the topography is sinusoidal, with the spread length (i.e. the maximum source-to-receiver offset) equal to one topographic wavelength. The model, depicted in Figure 4.6, has a 125-m surface variation, over a reflector at 1500-m depth. The source is placed on the recording surface at zero offset and 125-m depth. The source depth is not defined to be zero since the computer code assumes that all points on the recording surface have a non-negative depth and the surface peaks are 125 m above the source. Again, the velocity is a constant 2000 m/s. The spread has 201 receivers on the input surface, spaced uniformly as measured in the lateral direction, not as measured along the surface, with a separation of 12.5 m. Downward continuation of the receivers is performed such that the data are extrapolated to a

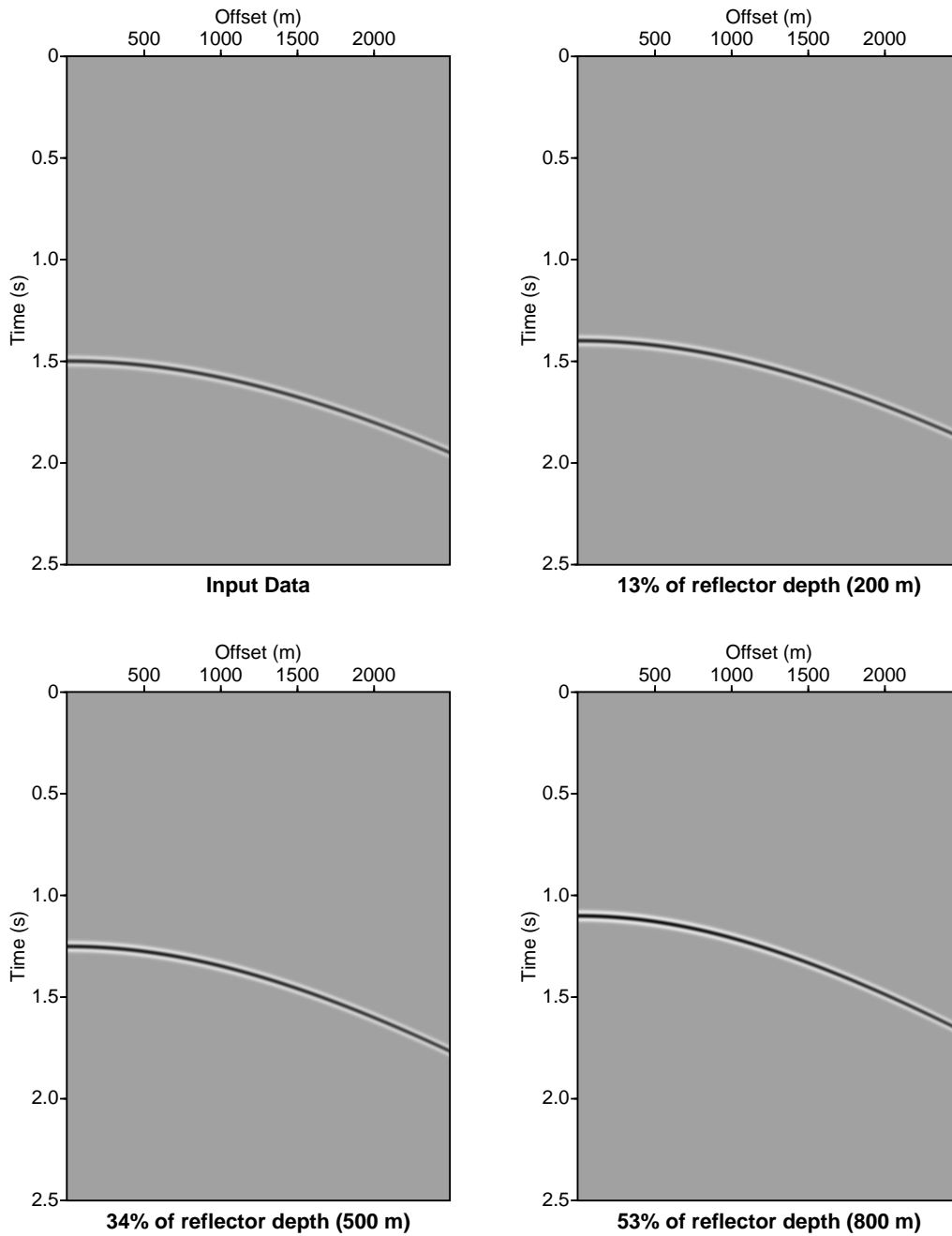


FIG. 4.3. Synthetic, common-source data for a horizontal reflector, with receivers on a horizontal recording surface, as well as on horizontal datum surfaces at three different depths.

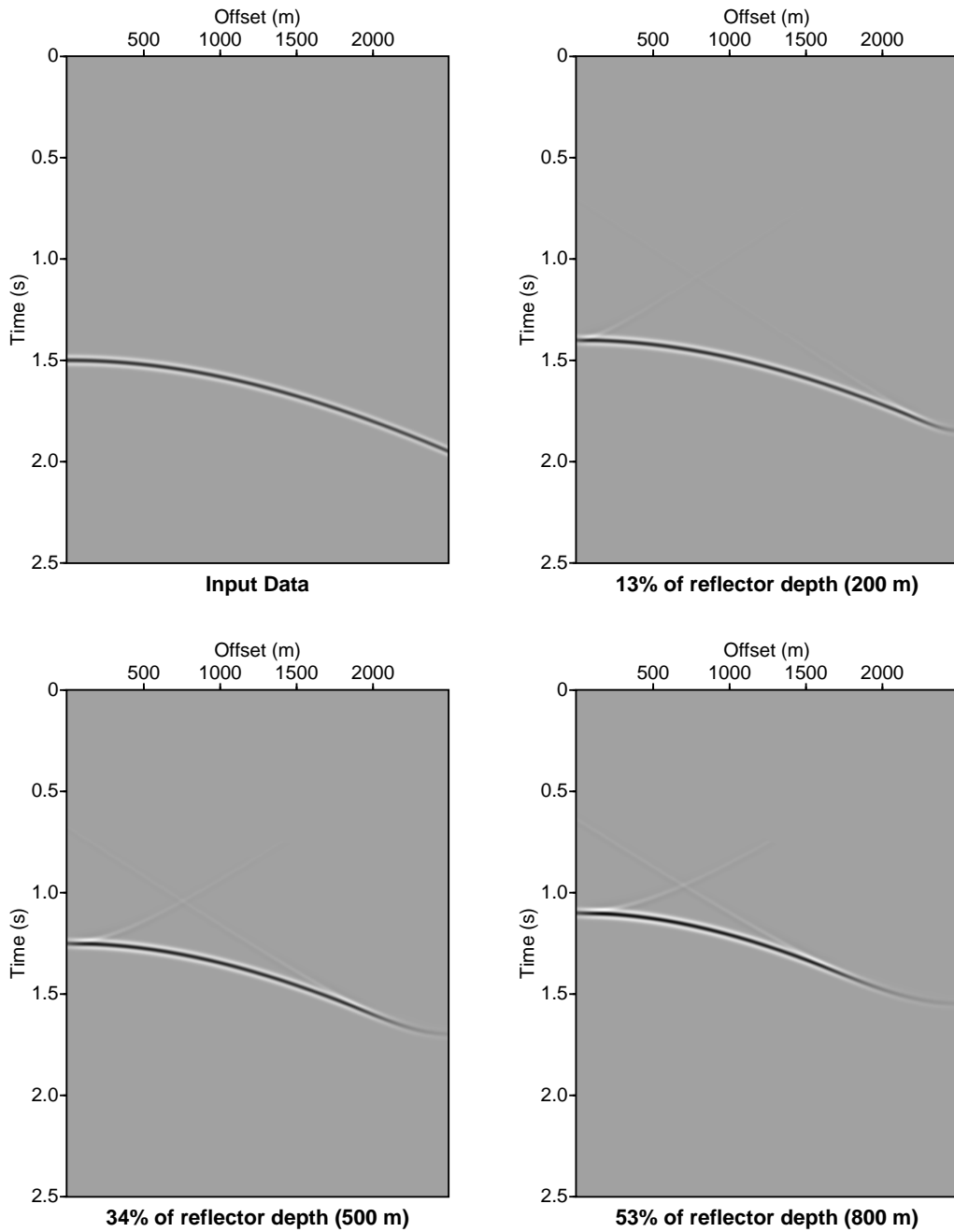


FIG. 4.4. Input and downward continued, common-source data for a horizontal reflector and horizontal recording and datum surfaces, showing kinematic results.

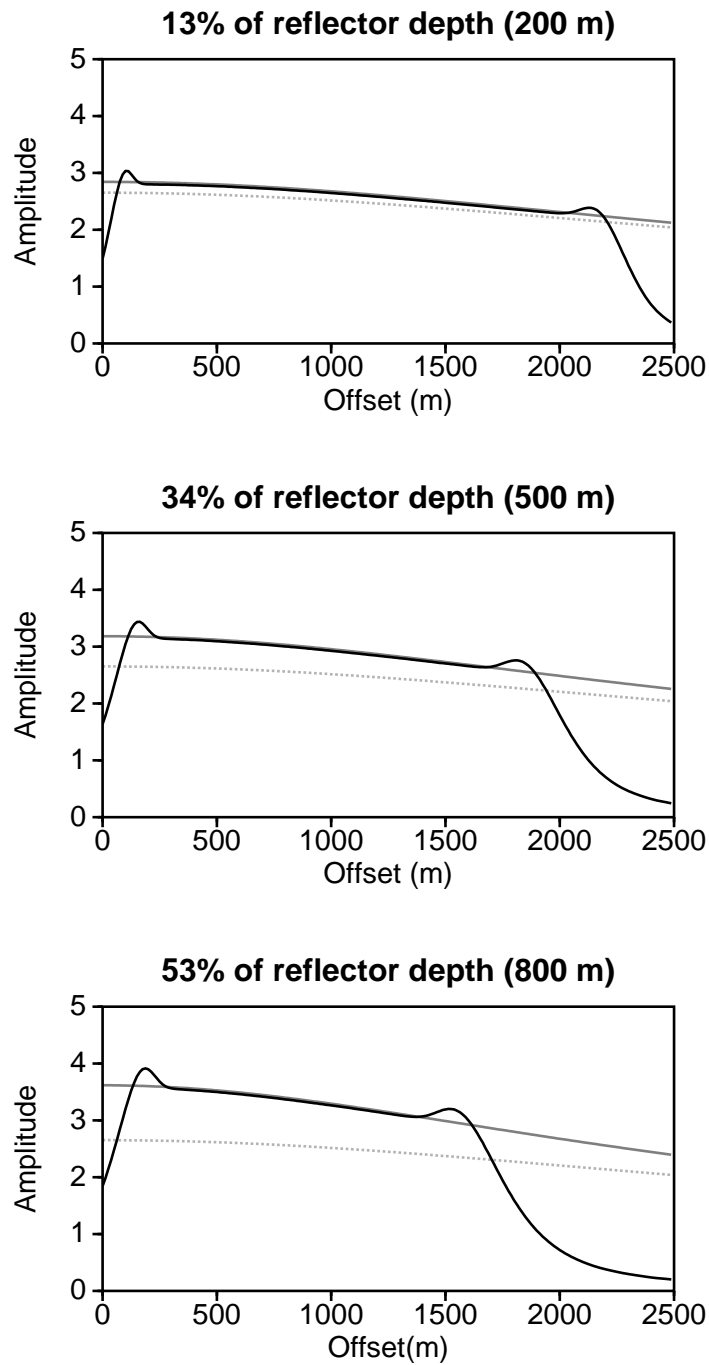


FIG. 4.5. Peak amplitude versus offset for downward continuation of receivers from a horizontal recording surface to three horizontal datum surfaces.

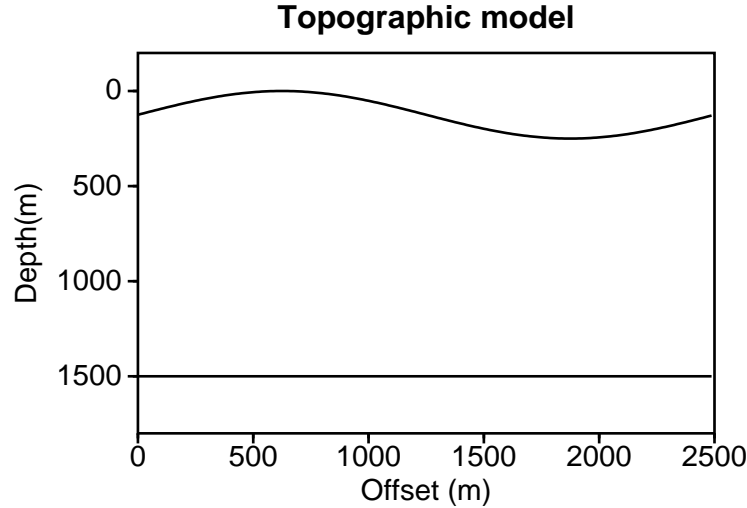


FIG. 4.6. Subsurface model with a topographic recording surface and a horizontal reflector, in a constant-wavespeed medium.

horizontal output datum, with receiver locations that are, again, spaced evenly in the lateral direction. The data has a 20-Hz wavelet, and is generated in the same way as in the above model.

Figure 4.7 shows synthetic, common-source data for this model, generated with receivers on the topographic input surface, and on three horizontal datum levels at depths of 325 m, 625 m, and 925 m, corresponding to 22%, 42%, and 62% of the reflector depth, or equivalently, 200 m, 500 m, and 800 m below the source. Figure 4.8 shows the input common-source data from the topographic surface, again, along with the results of downward continuation of this data to the three datuming depths using the data-mapping method.

Comparison of Figures 4.7 and 4.8 verify that the kinematic distortion due to the irregular surface has been corrected in the output data on the horizontal datum surfaces. Again, timing is accurate within an aperture interior to the ends of the spread, that decreases in width as the datum approaches the reflector depth, as in the previous model. As before, artifacts from the endpoints contaminate the primary arrivals near the ends of the aperture.

In Figure 4.9, the black curve shows peak amplitudes versus offset for the downward continuation of receivers. As before, the solid grey curve represents peak amplitudes from the synthetic data, and the dotted grey curve shows the peak amplitudes in the input data. The amplitude variation due to the surface has been corrected in the downward-continued data, and, as before, amplitudes match well with the analytic prediction within the useful aperture. The small amplitude peaks near the ends of the aperture arise due to edge effects.

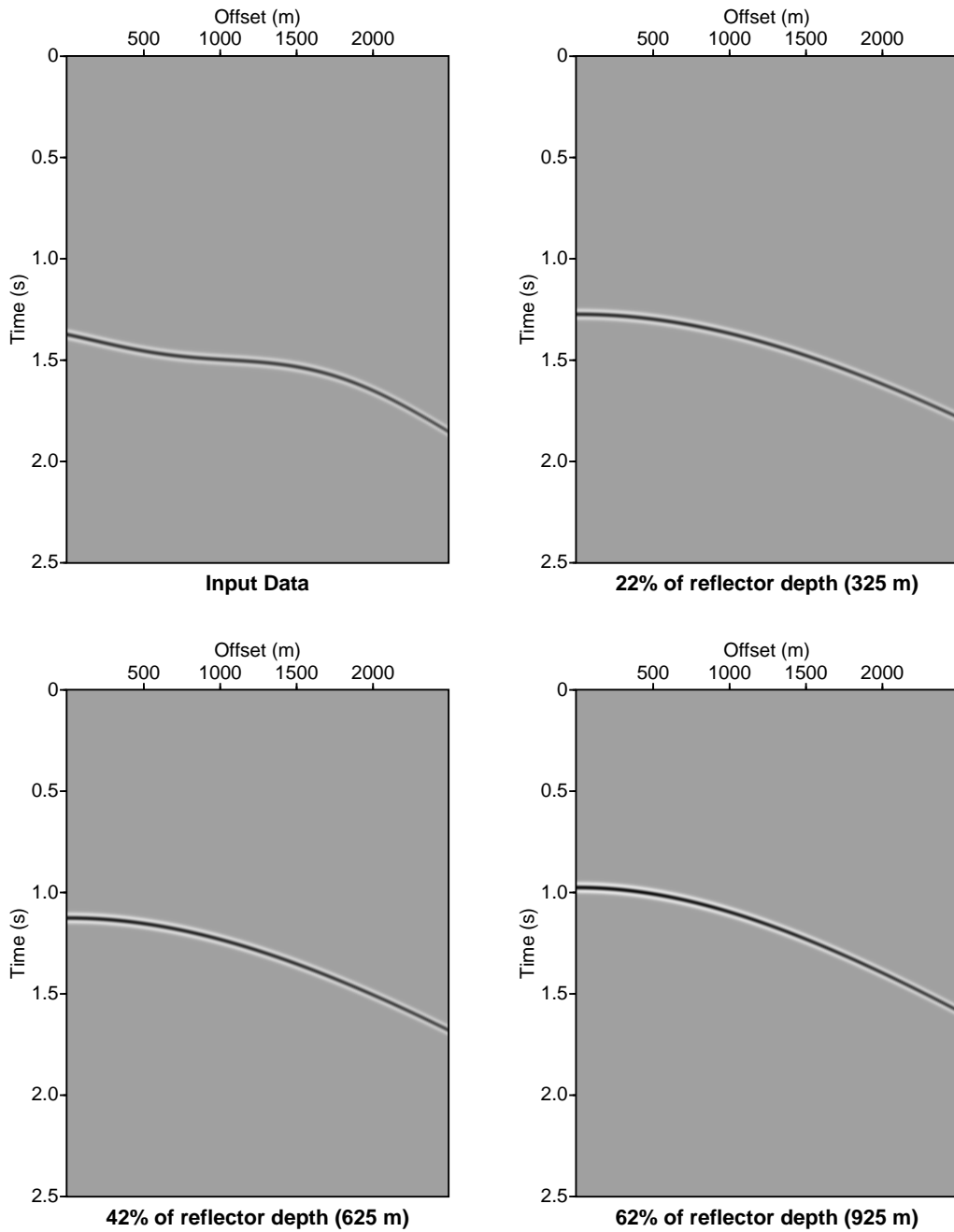


FIG. 4.7. Synthetic, common-source data for a horizontal reflector, with receivers on a sinusoidal recording surface, as well as on horizontal datum surfaces at three different depths.

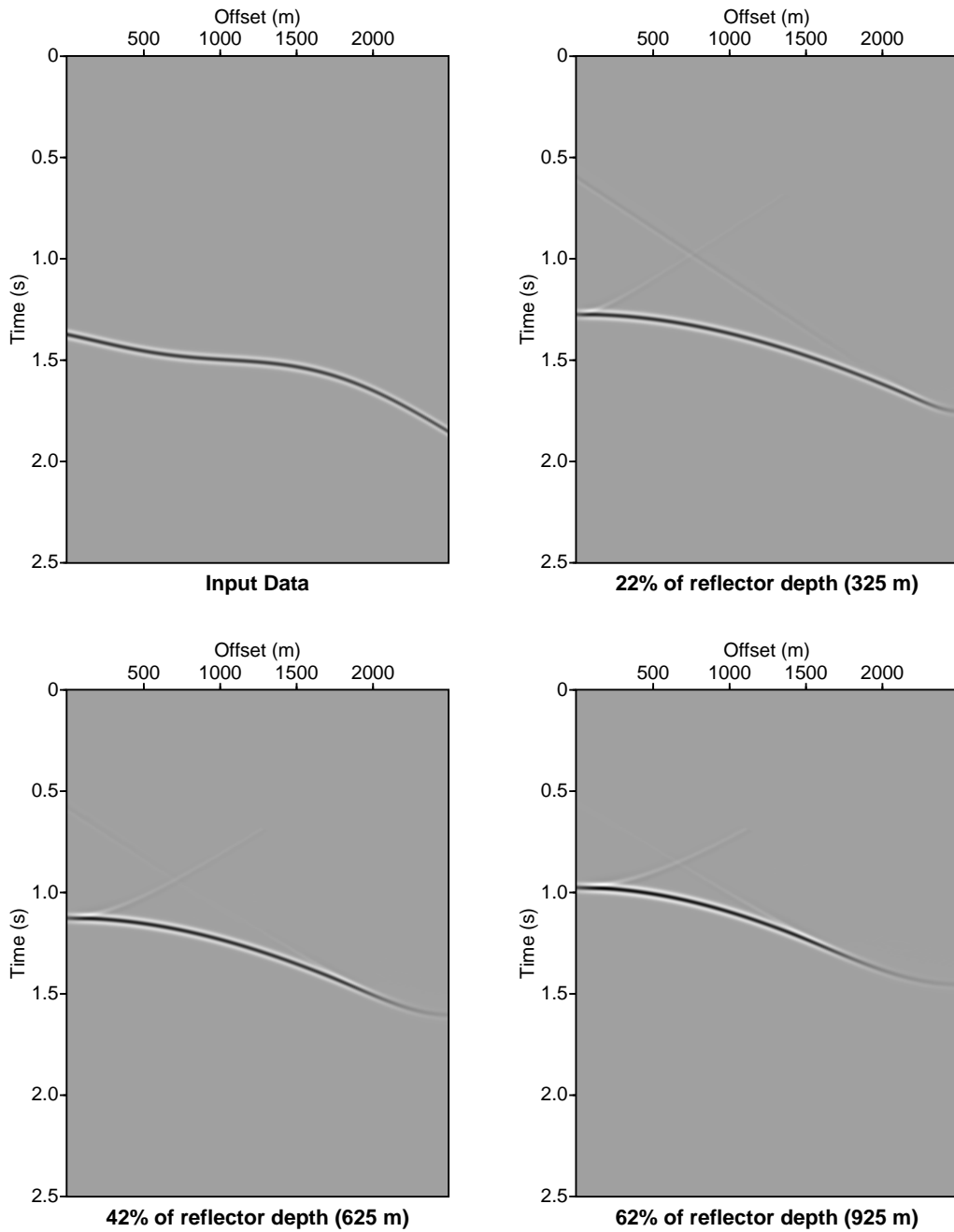


FIG. 4.8. Input and downward-continued, common-source data for a horizontal reflector and sinusoidal recording surface of 125-m amplitude, mapped to a horizontal datum at three depths.

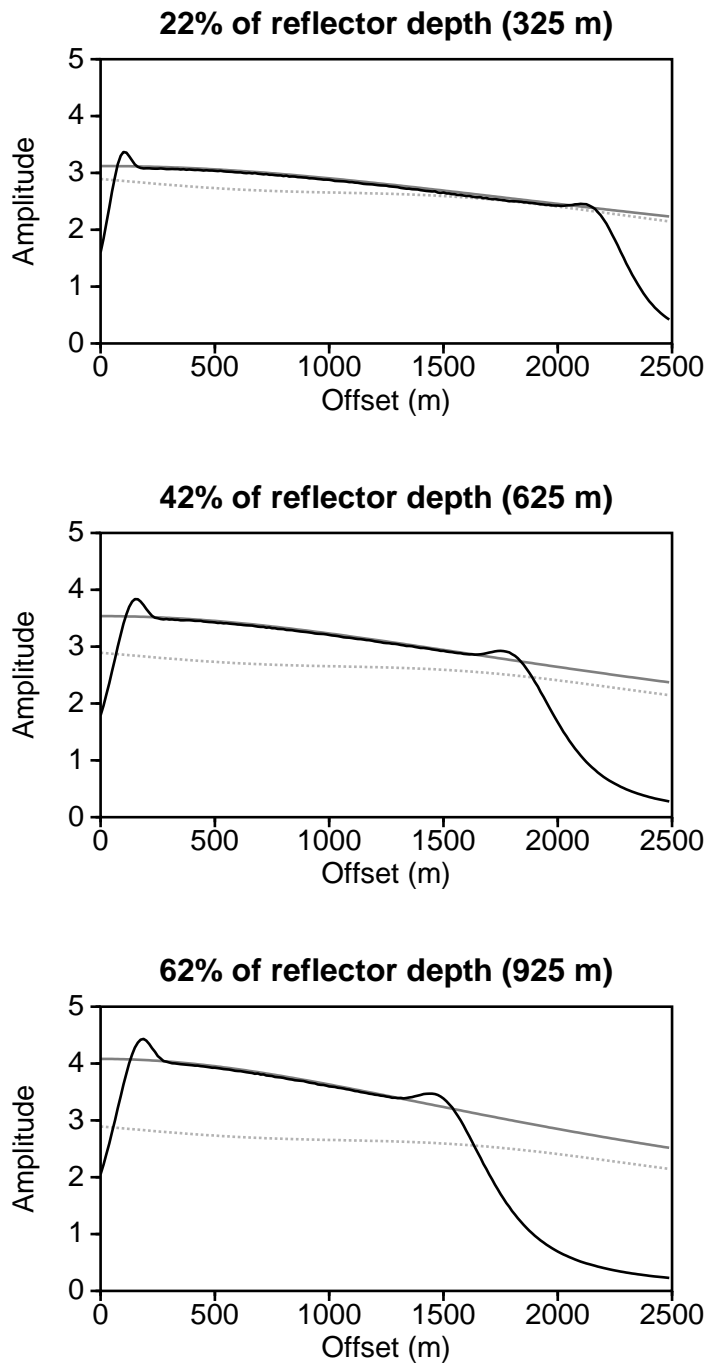


FIG. 4.9. Peak amplitude versus offset for downward continuation of receivers from a sinusoidal recording surface of 125-m amplitude to three horizontal datum surfaces.

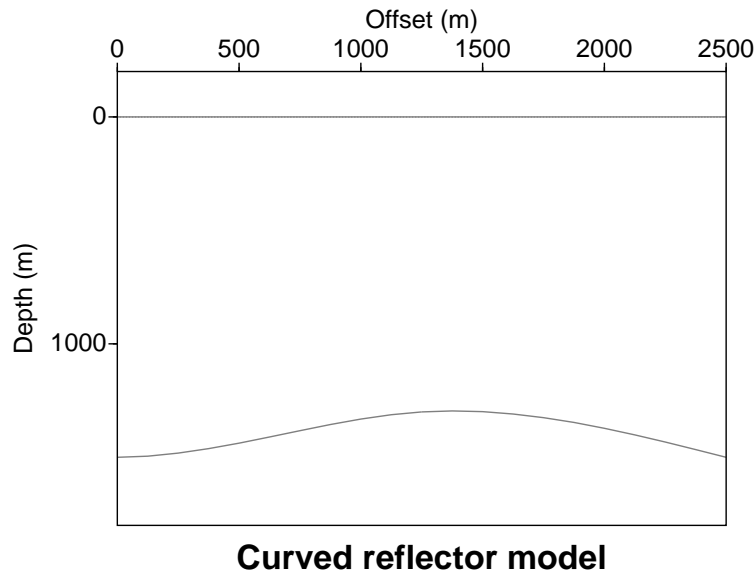


FIG. 4.10. Subsurface model with a horizontal recording surface and a curved reflector, in a constant-wavespeed medium.

4.3 Curved reflector and a horizontal recording surface

Next, consider the problem of common-source data collected on a horizontal recording surface, due to reflection from a single, curved reflector, in the shape of an anticline, with an average depth of 1400 m, and a relief of 200 m. As before, the wavespeed is a constant 2000 m/s between the surface and the reflector. The model is depicted in Figure 4.10. The gentle reflector variation is chosen in this example to avoid multiple arrivals, a case that is treated separately below. As before, downward continuation of the receivers is performed to horizontal datum surfaces, and 201 receivers are spaced uniformly along each of the recording and datuming surfaces, with a spacing of 12.5 m. Again, the wavelet has a peak frequency of 20 Hz. This time, however, the curved reflector requires that the data be generated using the CSHOT Modeling Program, part of the Center for Wave Phenomena code library at the Colorado School of Mines (Docherty, 1991). This code calculates 2.5D data for reflecting surfaces of irregular shape, which is “true-amplitude” in the sense that the amplitudes are correct for propagation through the chosen wavespeed model.

Figure 4.11 shows synthetic, common-source data for receivers on the input surface and on three horizontal datum surfaces at 200-m, 500-m, and 800-m depth. These depths correspond to roughly 14%, 36%, and 57% of the average reflector depth below the source. Figure 4.12 shows the input data again, and the results of downward continuation to the three datum surfaces using data mapping.

As in the previous examples, comparison of Figures 4.11 and 4.12 verifies that

the kinematic result is accurate within an aperture that decreases in width as the datum depth approaches that of the reflector.

Again, the black curve in Figure 4.13 shows peak amplitudes versus offset for the receiver continuation via the data-mapping method, the grey curve shows the amplitudes for the placement of the receivers on the output datum as calculated by the CSHOT modeling code, and the dotted grey curve displays the amplitude distribution of the input data. As in the previous examples, the amplitudes are correct within a depth-dependent useful aperture.

In this example, the shape of the reflector is a simple anticline, and, as in the flat reflector models, a single specular arrival path is associated with each receiver. If, however, the reflector were a syncline, or has a shape that contains any synclinal features, then, for some subset of the receivers, specular energy may arrive along multiple reflection paths of varying length. This situation arises in the presence of a *buried focus*. This is not to be confused with *multipathing* that arises from wave propagation through a wavespeed anomaly, or lens, such that the energy travels along multiple raypaths between a source and receiver through the same reflection point. A buried focus, on the other hand, refers to the presence of specular raypaths from a source to a receiver through more than one distinct reflection points.

The data-mapping method, like any Kirchhoff-type method, calculates an amplitude for each output receiver location and each output time by summing over energy contributions from all scattering points in the subsurface. Methods derived under the assumption that there is no multipathing require that there exist only one possible raypath connecting a given source and receiver through each scattering point. More than one path through a given scatterer creates a traveltime ambiguity that these methods are unable to resolve. However, there may be any number of single paths through different scatterers that result in specular energy arriving at the same output receiver at different times. This situation is perfectly valid in this method, and not subject to any assumptions about multipathing, as it is the result of an unrelated phenomenon.

Given this, the next example also has a curved reflector, but it is now sinusoidal with synclinal features. Figure 4.14 shows the model with a sampling of specular raypaths for the input data to illustrate the nature of the buried focus in the model. Note also that caustics are present in this problem.

Using the same three horizontal datums as in the previous example, Figure 4.15 shows synthetic data, and Figure 4.16 displays output from data-mapping extrapolations. The structure of the data is more complicated due to the “bow-tie” arrangement of the multiple arrivals. Note that, as the datum depth is increased, the bow-tie approaches the depth of a buried focus, where it collapses in on itself. Although the structure of the data is more complicated, comparison of these two figures still makes it possible to assess the accuracy of the kinematics in the data-mapping output within some interior region of offsets.

Given the presence of these multiple arrivals, picking and plotting amplitudes along any single branch in the data becomes difficult, especially in regions where

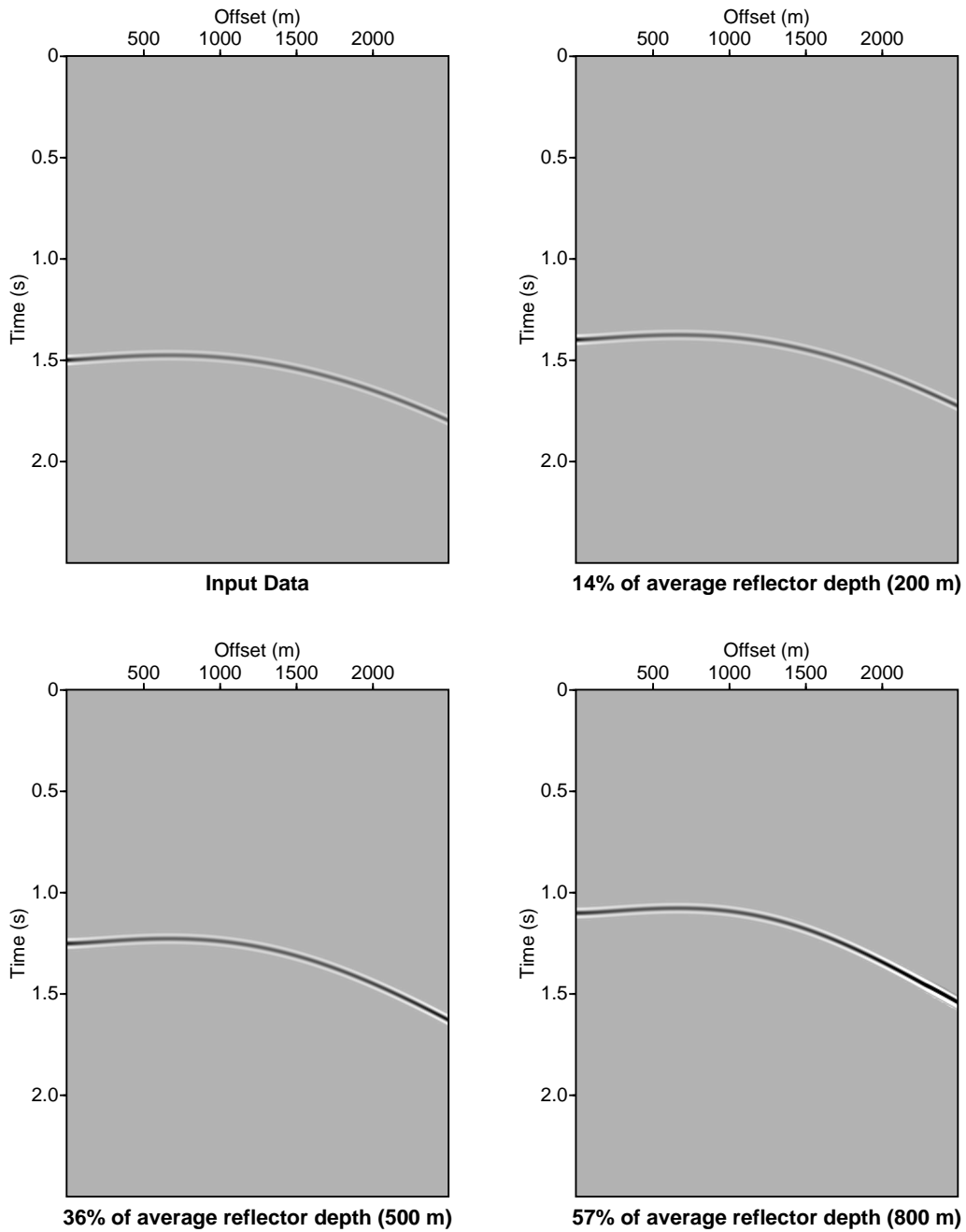


FIG. 4.11. Synthetic, common-source data for a curved reflector, with receivers on a horizontal recording surface, as well as on horizontal datum surfaces at three different depths.

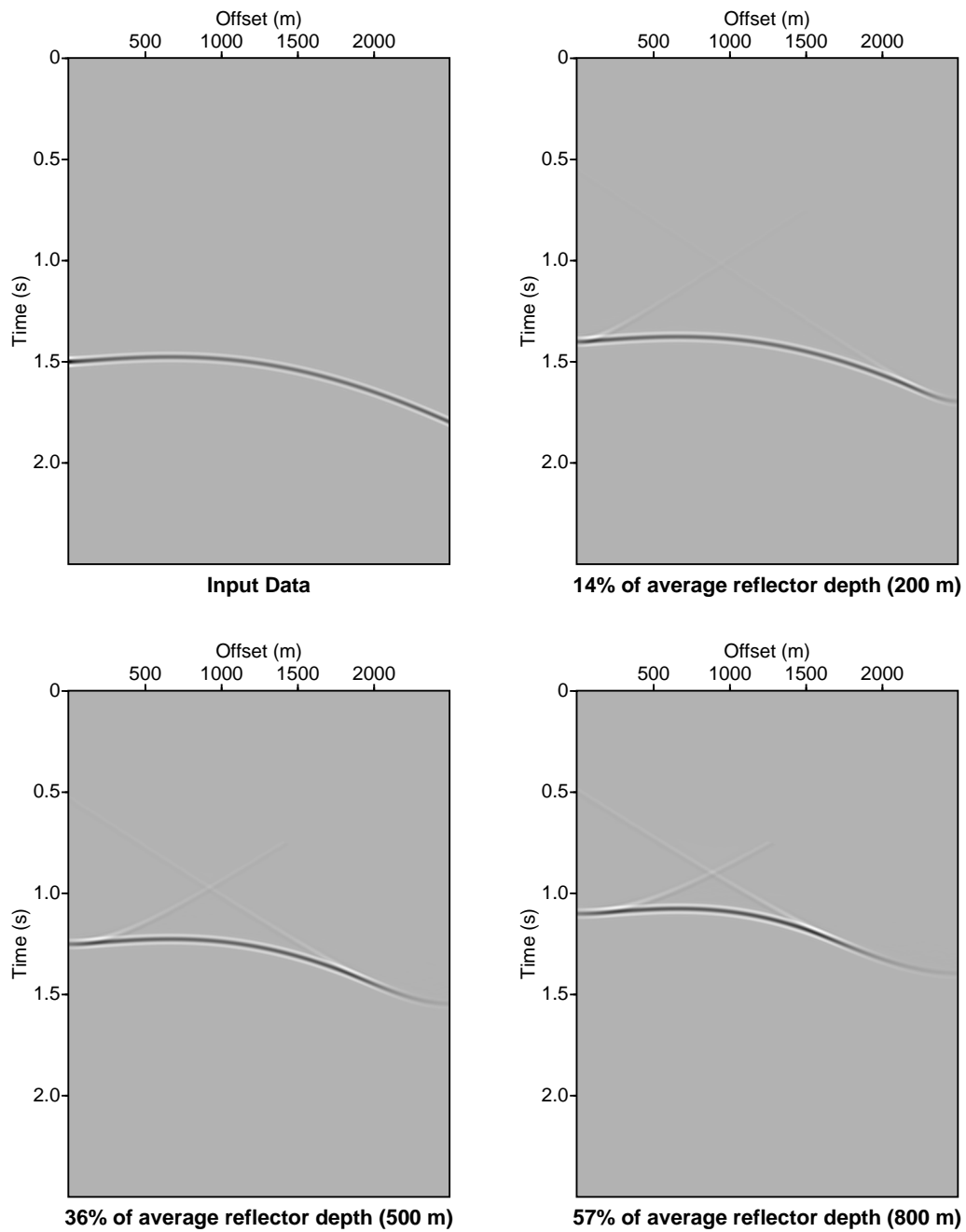


FIG. 4.12. Input and downward-continued data for a curved reflector on a horizontal recording surface and three horizontal datum surfaces.

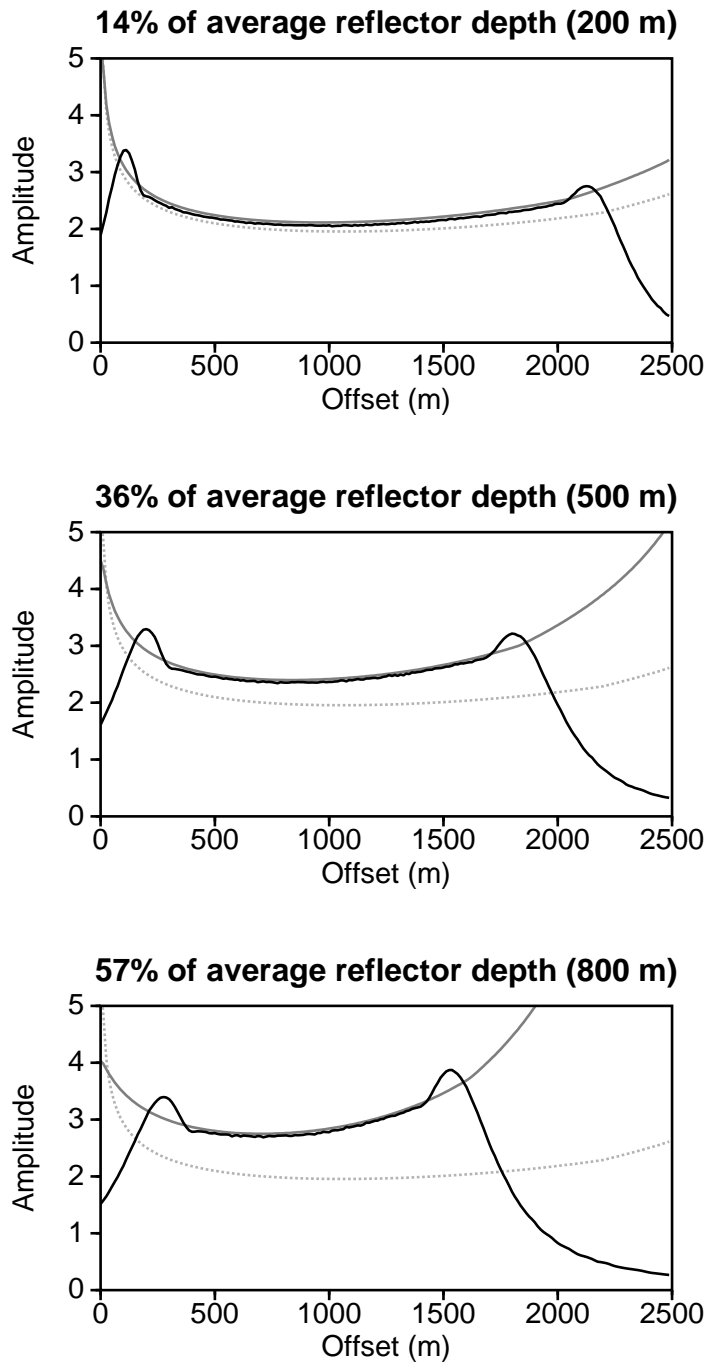


FIG. 4.13. Peak amplitude versus offset for downward continuation of receivers over a curved reflector to three horizontal datum surfaces.

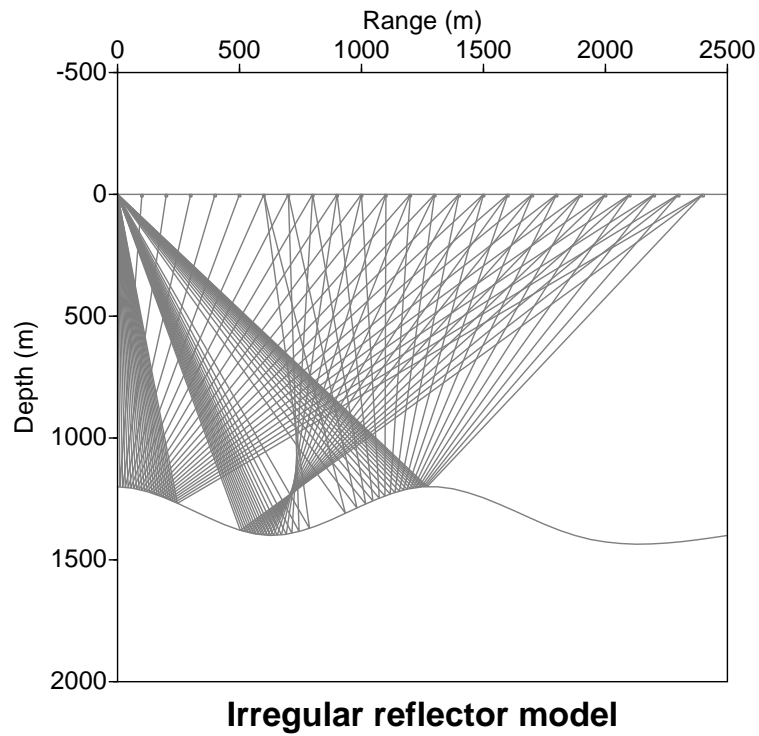


FIG. 4.14. Subsurface model with a horizontal recording surface and an irregular reflector, in a constant-wavespeed medium. Included is a sampling of specular rays, some of which cross at a buried focus.

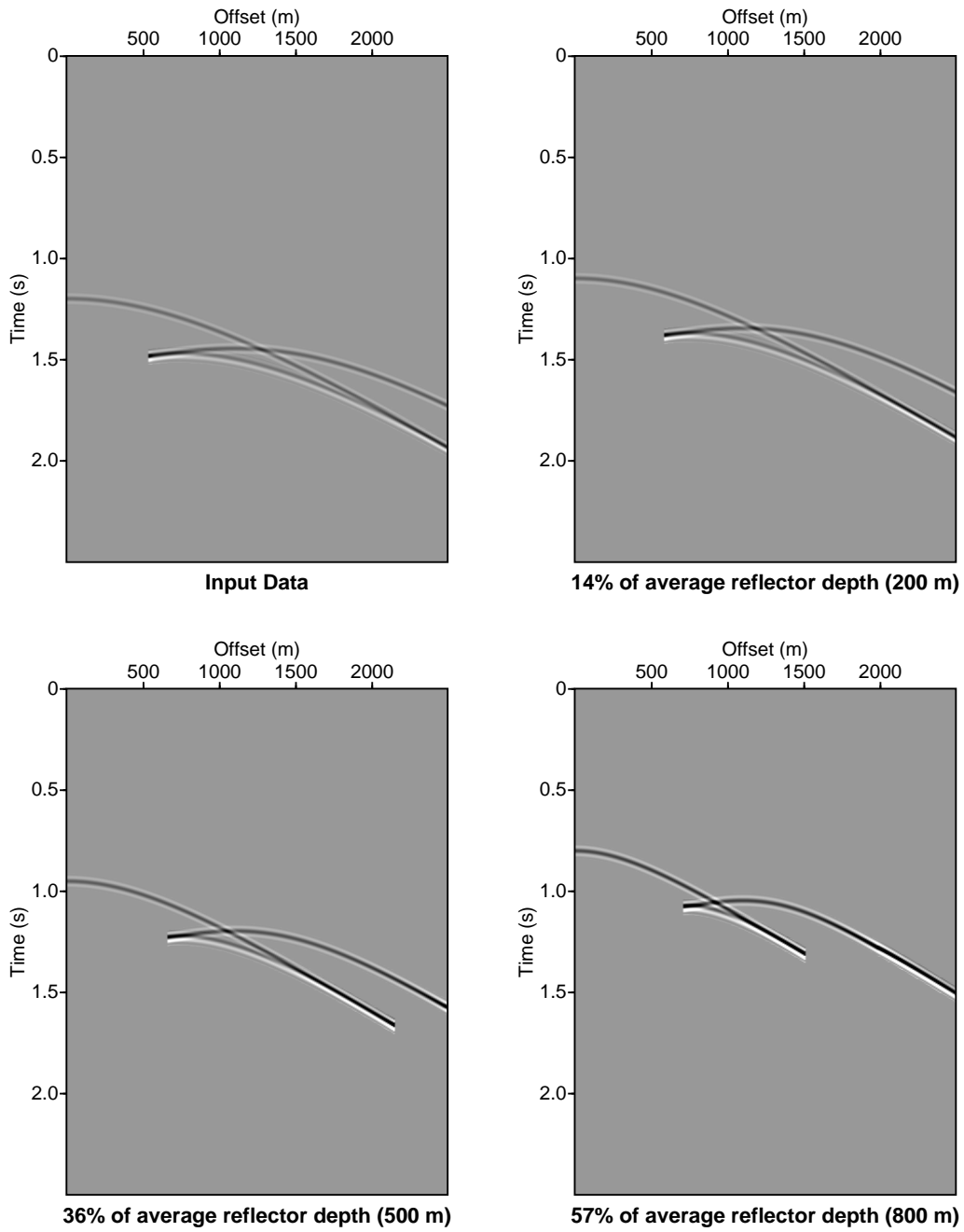


FIG. 4.15. Synthetic, common-source data for the synclinal reflector in Figure 4.14, with receivers on the horizontal recording surface and datum surfaces at three different depths.

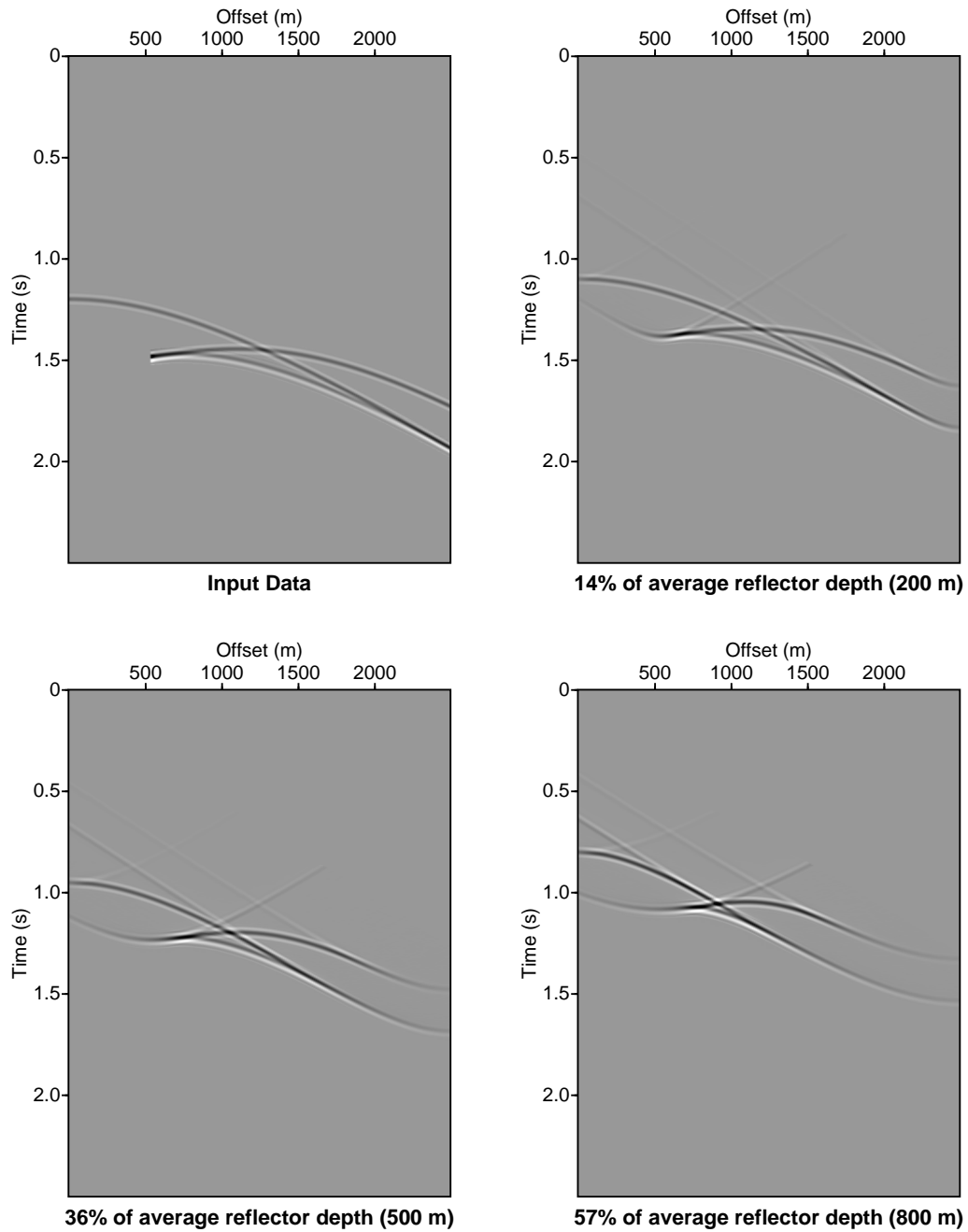


FIG. 4.16. Input and downward-continued data for the synclinal reflector and horizontal recording surface shown in Figure 4.14, and three horizontal datum depths.

these branches cross. Therefore, the amplitude-versus-offset results for this model are shown in data space. That is, each section of synthetic data from Figure 4.15 is subtracted from the corresponding data-mapping output section in Figure 4.16, creating a difference image for each datum. Arrivals where the amplitude and the phase of the data-mapping result match those of the synthetic data disappear to the background level in these difference images, and parts of the data-mapping output that are inaccurate retain some amplitude. This allows the accuracy for all the interacting arrivals to be depicted in a single plot.

Figure 4.17 shows these difference images for the three datuming depths. For shallow datum depths, the data-mapping results appear to be accurate over much of the interior of the data section, since most of the primary energy in the output data is not visible in the difference image. Only the linear artifacts arising from edge effects display significant energy in the interior of the difference image. As the datum depth increases, though, large errors occur in the interior of the difference image that are not associated with edge effects, but arise from phase errors in the input data. CSHOT does not properly determine amplitudes near the cusps of the caustics, and erroneous phase shifts appear in the data-mapping results.

4.4 Curved reflector and a topographic recording surface

Finally, consider the more general model of a curved reflector beneath a topographic recording surface, as shown in Figure 4.18. The model contains the same curved reflector as in the previous example given in Figure 4.10, but has an irregular recording surface that is approximately a sinusoid of 125-m amplitude and a variation of roughly one wavelength across the receiver spread.

The geometry of the survey is as in all the previous examples. Data are for a common-source gather with 200 receivers spaced 12.5 m apart as measured along the horizontal, starting at zero offset. As before, the data contain a wavelet with a peak frequency of 20 Hz. The source is on the recording surface at zero offset, which is again defined to have a depth of 125 m. That is, so that all recording surface locations have non-negative depths. The wavespeed is a constant 2000 m/s.

Figure 4.19 shows the synthetic data for the model at input and on three horizontal datums at 325 m, 625 m, and 925 m. The raw and data-mapping extrapolated data are shown in Figure 4.20. Again, comparison of these figures verifies the kinematic accuracy of the downward continued data. Peak amplitudes for synthetic and downward continued data are shown in Figure 4.21, as before.

The above discussion of synthetic model results focused mainly on qualitative observations of the useful aperture, that is, the range of offsets where output amplitudes are accurate. A more quantitative discussion the useful aperture is possible, though, by considering the two main factors in the determination of its width and location in more detail. These factors are finite spread length, or finite data aperture, in the input data, and asymptotic validity conditions on the data-mapping result. Both are discussed in the next chapter.

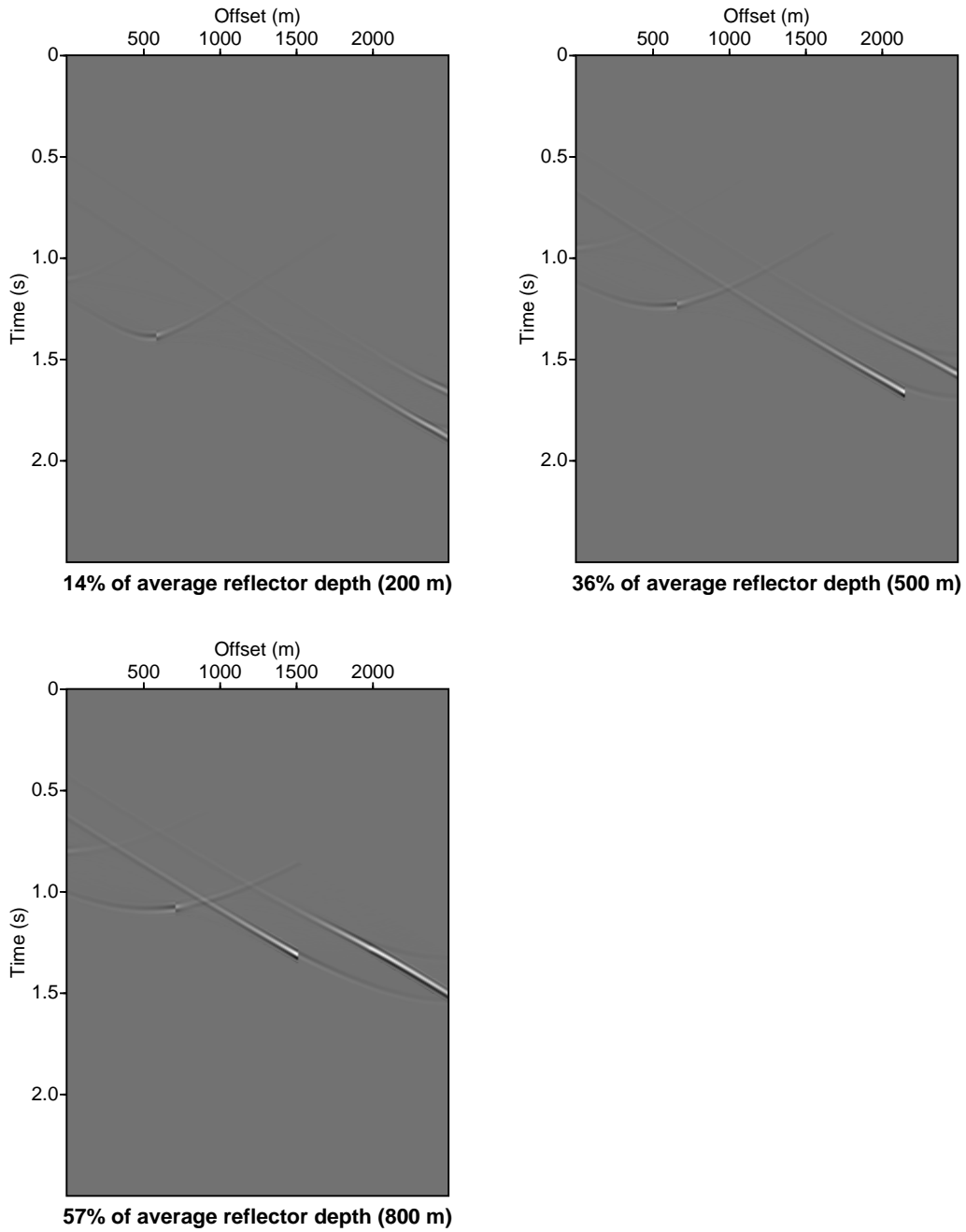


FIG. 4.17. Difference images of downward-continued data and CSHOT model data generated for the synclinal reflector and horizontal recording surface shown in Figure 4.14.

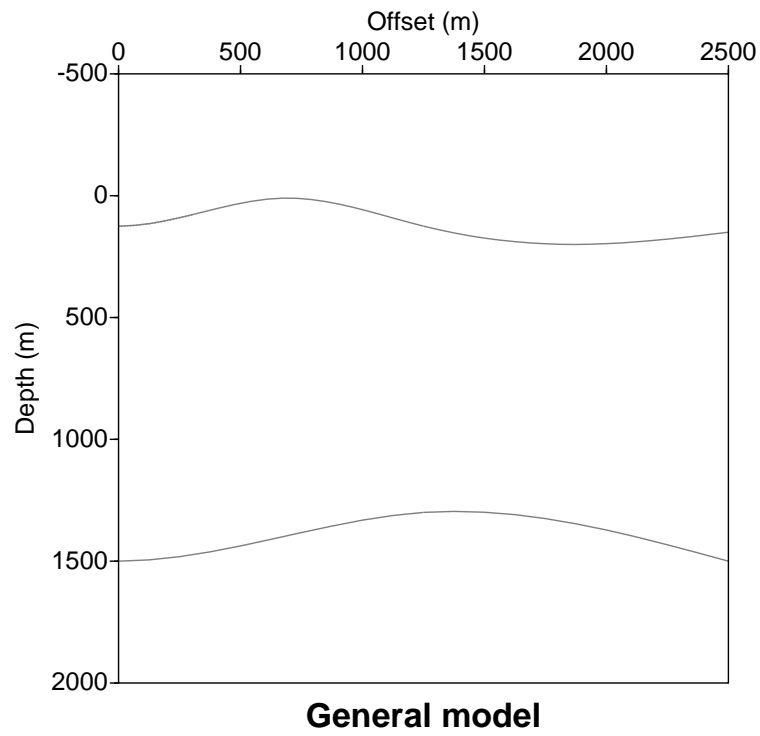


FIG. 4.18. Subsurface model with a topographic recording surface and a curved reflector, in a constant-wavespeed medium.

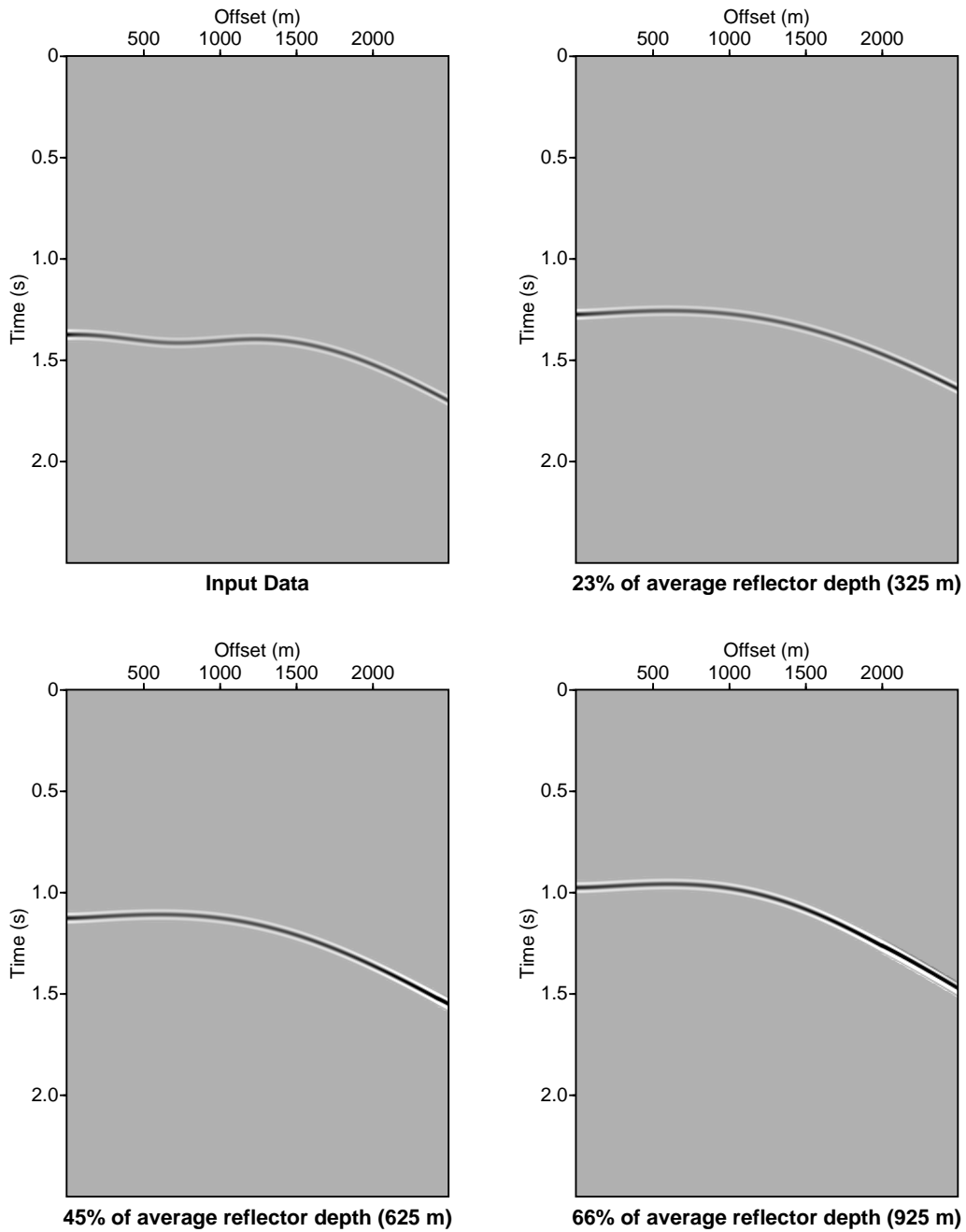


FIG. 4.19. Synthetic, common-source data for the curved reflector and topographic recording surface model of Figure 4.18, with receivers on the recording surface and datum surfaces at three different depths.

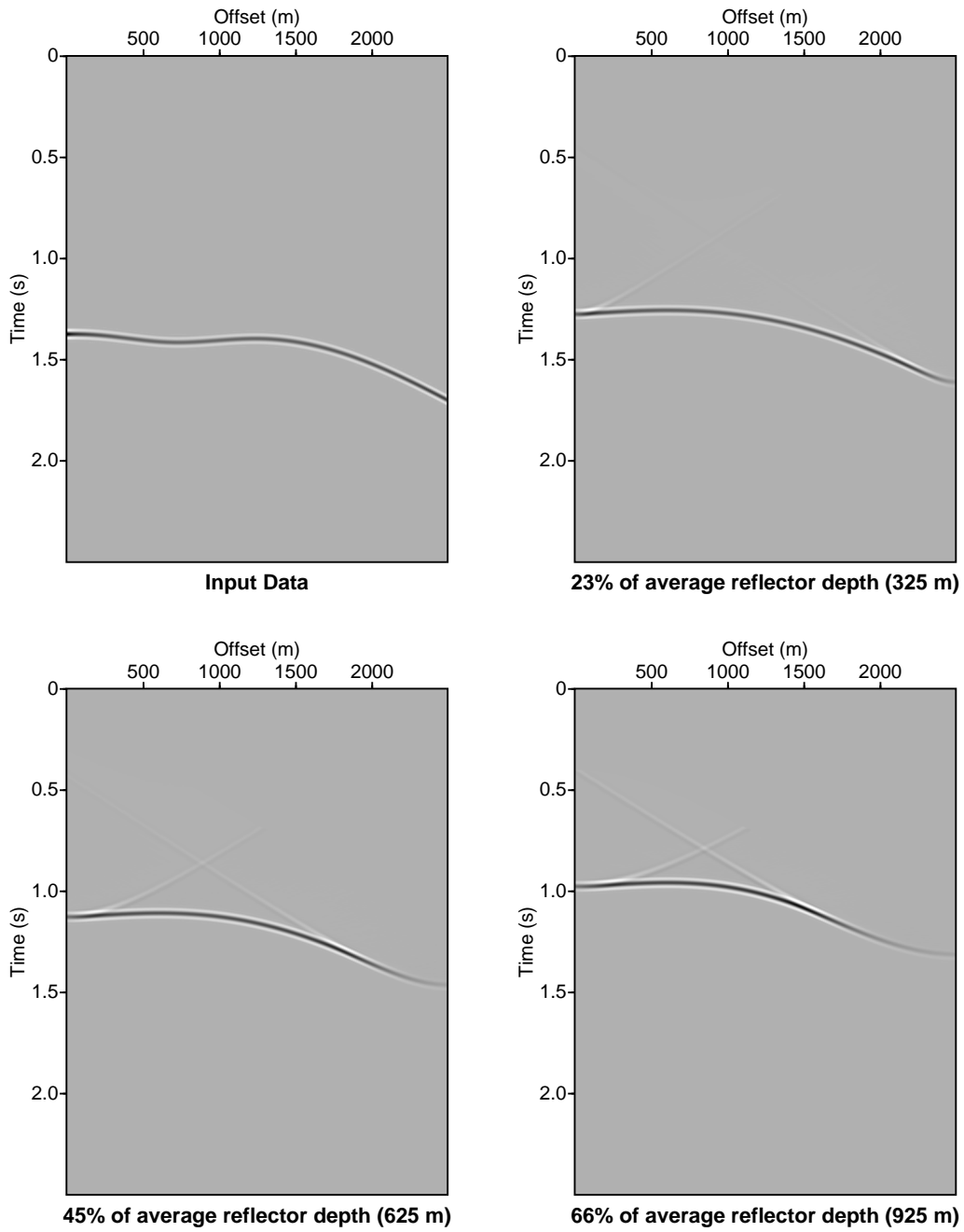


FIG. 4.20. Input and downward-continued common-source data for a curved reflector and topographic recording surface, mapped to a horizontal datum at three depths.

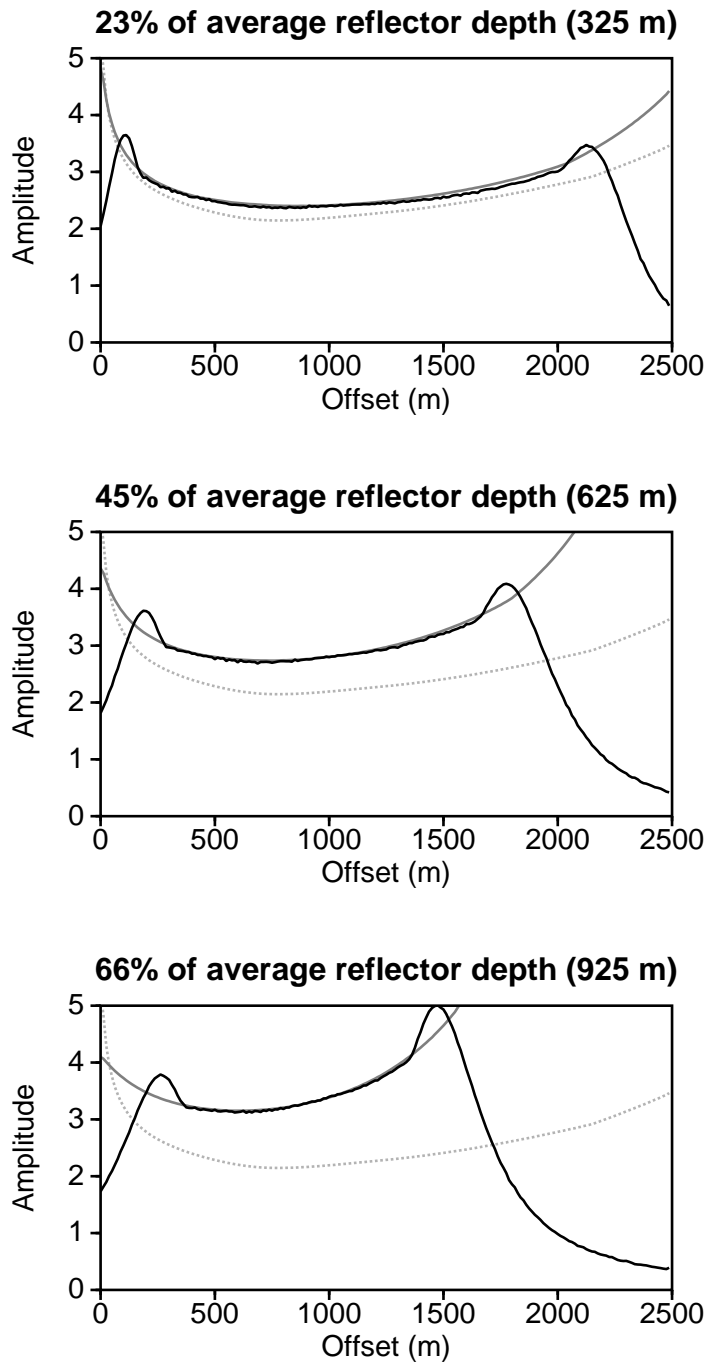


FIG. 4.21. Peak amplitude versus offset for downward continuation of receivers over a curved reflector, from a topographic recording surface to three horizontal datum surfaces.

Furthermore, direct comparisons of the results from these and other similar models with other Kirchhoff downward-continuation algorithms are possible, and are investigated in Chapter 6.

Chapter 5

VALIDITY IN DATA MAPPING

Amplitude accuracy in downward-continued data produced by the data-mapping method is limited by two primary factors. The first is finite data aperture. This limits the range of offsets in the output data at which accurate amplitudes are possible to obtain. The second is presence of validity conditions on leading-order asymptotic analyses inherent in the data-mapping platform. These not only play a role in determination of the useful aperture, but also limit characteristic length scales in the problem and the allowable curvatures on the recording and reflecting surfaces.

5.1 Finite data aperture and ray theory

The datuming examples in Chapter 4 showed that the data-mapping method produces accurate amplitudes within a limited range of offsets, defined in this study as the useful aperture of the problem, the width of which decreases as the datum depth approaches that of the reflector. In practice, data always exist over some finite range of offsets, so this reduction of the useful aperture is generally observed in downward-continued data.

This aperture reduction, however, does not indicate that any information about the reflector contained in the input data is lost. Instead, it is a result of the fact that all upcoming waves are spreading, and, therefore, energy that eventually emerges within the receiver spread on the input surface is entirely contained within a smaller range of receiver offsets on a deeper datum surface. So, all energy associated with the illuminated part of the reflector is contained in the output data, but concentrated over a smaller range of offsets. Output receiver locations outside this range are associated with upcoming energy that emerges outside of the finite receiver spread on the input surface. Therefore, amplitudes at these locations are not recovered, since the required wave energy is not in the input data.

To understand this aperture reduction, recall that the datuming integral is, for discrete data, a Kirchhoff-like summation, in the sense that the value of the output field at some output receiver location and output time, t_O , is a sum over contributions from each input location (data trace). In this method, though, each of these contributions is a function of quantities measured along a particular raypath through a unique stationary point, which lies on the reflection isochron associated with the output time under consideration. This set of stationary points and rays for the summation are depicted schematically in Figure 5.1, where \mathbf{x}_S is the fixed source location, \mathbf{x}_{OG} is the output receiver of interest, and the $\mathbf{x}_{IG}(\xi_I)$ are the input data locations, on the recording surface. The stationary points lie on the $\tau_O = t_O$ isochron, where

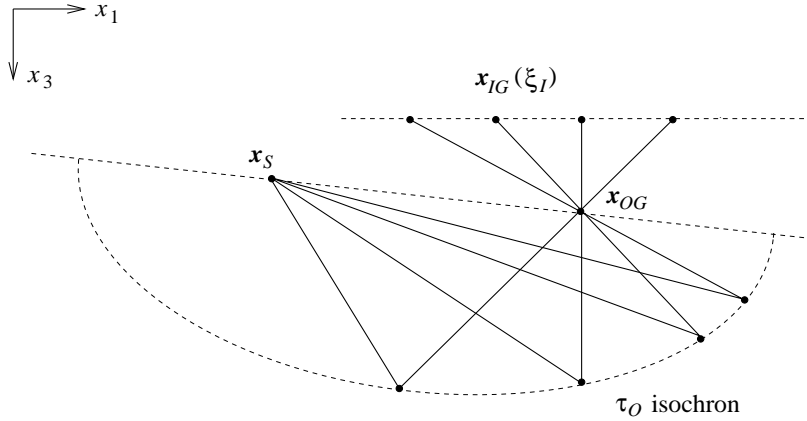


FIG. 5.1. 2D depth section schematically depicting rays and stationary points for downward continuation.

t_O is the output time of interest, as described previously. Note that this schematic figure, drawn for receiver continuation in constant-wavespeed media so that raypaths are straight and isochrons are elliptical, can be generalized to other raypath, isochron, and recording surface shapes, or for source continuation.

In the absence of multipathing, the set of raypaths implies a one-to-one correspondence between the stationary points along the isochron and each input receiver location, and therefore each data trace. Each stationary point and its associated raypath represents possible wave energy in the input data that arrives at the chosen output receiver location at the output time $t_O = \tau_O$.

Since data-mapping is a high-frequency method, it is assumed that the most significant wave energy is associated with specular raypaths. So, some insight into the aperture limiting mechanism is gained by investigating the influence of specular rays in the determination of the output field. Since they account for a significant portion of the scattered energy, accurate evaluation of the infinite integral expression requires that contributions from all stationary points associated with actual specular reflections be included in the summation. If, however, some of these specular rays emerge at recording surface locations that are outside the finite range of the data, then the absence of this specular energy from the input data prevents an accurate summation result. This is a description of the problem of approximating an infinite integral by a finite summation.

For example, consider the output receiver location \mathbf{x}_{OG} on Figure 5.1. Raypaths associated with the left-most stationary points on the isochron emerge at large offsets on the recording surface, some of which may be beyond the end of the receiver spread. If any of the rays that emerge beyond the last input receiver carry actual specular energy, then the input data does not contain all the energy necessary to yield an accurate amplitude at this output location and time. The same thing may occur for rays scattered through stationary points on the right-most part of the isochron that

surface at the small-offset end of the receiver spread, if they emerge to the left of the first input receiver.

The above discussion considers a single application of the integral, that is, the determination of the field at a single output location and time, without reference to any specific reflector geometry. Which stationary points and their associated rays account for the specular contributions to this summation depends on the subsurface model. The accuracy of the amplitude at each output location and output time, that is, each data point in the output, may degrade if the model is such that any rays carrying significant energy emerge outside the range of the input data, and their required contribution is missing from the summation. Furthermore, amplitude accuracy of a particular arrival in the output data is a function of the accuracies of all the data points that define the arrival, and is, thus, a result of the net action of a large number rays. So, in general, a specular ray-based analysis of this type to attempt to understand the influence of finite spread length on the amplitude accuracy of particular arrivals in the output data can be a complicated proposition.

For homogeneous, single-reflector models, however, such as many of those shown in this paper, this analysis is relatively simple. In these cases, there is some finite aperture in the output data, which is associated with all relevant specular energy present in the finite input data. Hereafter, this is referred to as the *specular aperture*. The specular aperture is a function of the subsurface model, the maximum data offset, and the depth of the output surface.

Consider the specular aperture for a common-source survey over a single horizontal reflector, as depicted in Figure 5.2. In this example, as well as in the synthetic models shown throughout in this study, there is no gap between the source and the first receiver, and the input and output surfaces are entirely covered by receivers, starting at zero-offset.

In this configuration, the specular energy associated with the first receiver on the input surface, the zero-offset receiver, travels along the vertical specular ray depicted on Figure 5.2 by a vertical dashed line below the source with reflection point A . The specular ray that emerges at the last receiver on the input surface is denoted by the second dashed line on the figure, and has the reflection point B . All specular rays that emerge within the input receiver spread have reflection points between A and B . That is, the illuminated part of the reflector in this problem is contained between A and B .

Observe the specular path arriving at the last offset in the input data through reflection point B . On each datum surface at some depth closer to the reflector, this raypath passes through an output receiver location having a smaller offset. At the source-end of the survey, however, the vertical ray carrying the zero-offset specular energy passes through the zero-offset receiver location on each datum. So, the output data on any given datum surface contains all specular energy scattered from the illuminated part of the reflector in a range of offsets that is reduced from the right, or large-offset, end of the survey, relative to the spread of the input data. This defines the specular aperture for each datum surface.

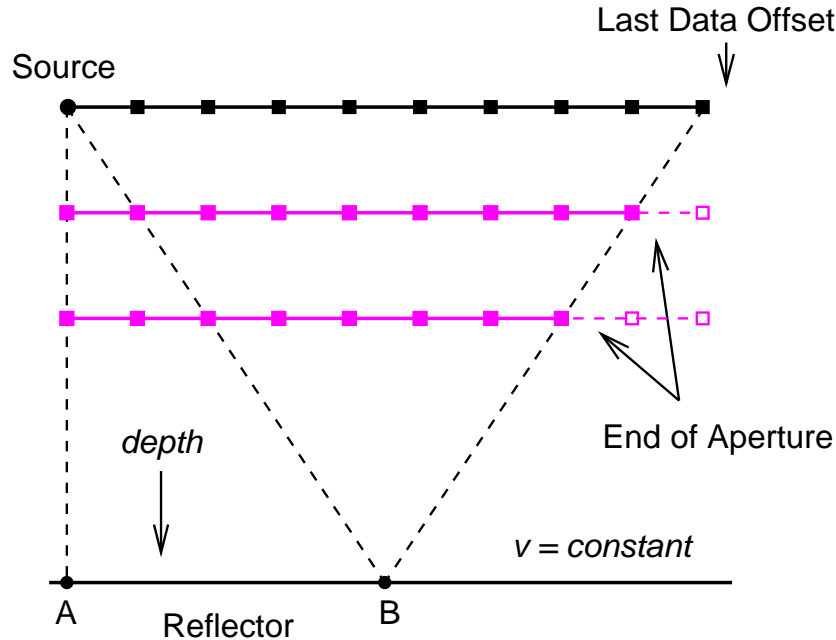


FIG. 5.2. Depth section showing the reduction of useful aperture in the horizontal-reflector model.

Specular paths associated with locations on the datum beyond the end of the specular aperture arrive at the original recording surface at offsets beyond the end of the receiver spread, and energy traveling along them is not included in the input data. Therefore, amplitudes at these large offsets are not fully recovered in the downward-continued data.

Note that, in this example, the specular aperture on the datum surface begins at zero offset, coincident with the beginning of the input data spread, and not at a location interior to it. Because the reflector is horizontal, the wavespeed is constant, and there is complete receiver coverage from zero-offset to maximum offset on all surfaces, the zero-offset specular ray is vertical and passes through through the zero-offset receiver on the input surface, as well as on each datum. So, the reduction of the specular aperture that occurs at large offset does not occur near zero-offset. However, this survey geometry does not guarantee this behavior in general. If the reflector is not horizontal or the medium is heterogeneous, the zero-offset ray may not be vertically propagating, and may emerge to the left of the source, resulting in the same type of reduction of the specular aperture on this end of the data as well.

5.2 Finite data aperture and asymptotic wave theory

While the above analysis of the reduction of the useful aperture in downward continuation using only specular arguments is enough to illustrate that the full amplitude cannot be regained outside of some specular aperture, it does not fully explain

the observed departures from the true solution. The inadequacy of the specular-ray approach alone in interpreting the useful aperture is clear in the results of the synthetic models shown in the previous chapter. For example, the model results show that, even in the case of a horizontal reflector and a homogeneous medium, the useful aperture is reduced near zero-offset, even though the previous section argues that no aperture reduction due to specular arguments is expected at small offsets for the given source/receiver geometry. Furthermore, if the presence or absence of the specular ray were the only aperture-limiting mechanism, then the output amplitude would be exactly correct within a specular aperture, and then drop immediately to zero for all offsets beyond that associated with the last specular arrival in the input data. The amplitude function in the model results is clearly more complicated than this, and the useful aperture is generally smaller than the specular aperture for any given problem.

These observations imply that ray theory alone is not sufficient to explain the observed amplitudes and the width of the useful aperture. Because data mapping is a wave theoretical, Kirchhoff-like approach, not all wave energy propagates along specular rays, even under the assumption of high frequency. Rather, energy is spread over a bundle of rays in some neighborhood around the specular ray. So, amplitudes may be inaccurate even when the specular ray is recorded, if energy associated with any members of this ray bundle surfaces outside the input data spread, and are not included in the input data.

In the simple example problem of Figure 5.2, this manifests itself as a type of edge-effect, and means that amplitudes in some neighborhood of the ends of the specular aperture are inaccurate. The amplitude at zero-offset on the datum surface depends on the vertical specular ray as well as a bundle of rays on either side of the specular. Energy from this specular ray, as well as that from rays emerging at adjacent points inside the data spread is present in the input data. However, energy traveling along rays in the bundle that emerge on the other side of the source is not. Therefore, important contributions to the summation are not in the input data, and the zero-offset amplitude is erroneous. The same may also occur at some near zero-offset receiver locations. This implies that the small-offset end of the useful aperture is located at an interior receiver location such that all significant members of the associated ray bundle emerge at or to the right of zero-offset. The same thing occurs at the large-offset end of the data, such that the end of the useful aperture is at some offset interior to the end of the specular aperture for the datum, due to this same edge-effect. Thus, the useful aperture must generally be smaller in width than the specular aperture.

This ray-bundle idealization, however, is just a conceptual description of the result of applying leading-order asymptotics to integrals with a finite region of integration. The method of stationary phase employed in the derivations of the data mapping platform (Bleistein & Jaramillo, 1997, 1999, Bleistein et al. 1997) is the result of a leading-order approximation of a more general asymptotic series. This means that the accuracy of the approximation is implicitly dependent upon the assumption

that there are no finite endpoints of integration, or at least that such endpoints have no significant contributions. Contributions from endpoints of integration appear in higher order terms that are truncated in the leading-order approximation. Field data are generally finite in extent, so this condition is satisfied in this case only if the data go smoothly to zero at the endpoints. Field data, however, do not generally have this property. The result, then, is that amplitudes are inaccurate for any stationary points in a neighborhood of these endpoints because accuracy of the method relies on the contributions from isolated stationary points bounded well away from any endpoints of integration. For example, Bleistein & Handelsman (1986) show that when a stationary point is coincident with an endpoint of integration, the predicted value is half of the value of an interior stationary point with the same functional value.

The ways in which this pertains to the datuming problem depend on where stationary phase is applied in the derivations, and how the validity of each application is influenced by finite data aperture. It turns out that the most important application of stationary phase for this discussion is not that applied in the general derivations of this paper, but that inherent in the derivation of the data mapping platform itself.

In Bleistein & Jaramillo (1997, 1999), the authors cascade a modeling formula with an inversion formula to derive the so-called *data mapping platform*, which includes equation (2.1) for the 2.5D case. Therefore, the validity of the data-mapping formula is limited by the conditions on the validity of any asymptotics inherent in either component of the cascade.

As shown in Bleistein et al. (1997), the inversion formula is derived under the requirement that it produce the correct, ray-theoretical, “true-amplitude” reflectivity when the input data are Kirchhoff-approximate modeling data for a single reflector of arbitrary shape. This is accomplished, in part, by conjecturing an inversion formula of the correct form, and then using it to perform a trial inversion of the Kirchhoff data. Since the reflectivity model assumed for this Kirchhoff data is arbitrary, but known, the results of the trial inversion are compared with the true reflectivity, and the final inversion formula is derived from this comparison. The trial inversion is a totally analytic calculation, and includes an integration over the recording surface evaluated by stationary phase. Thus, data mapping and any processes based upon it, such as the downward continuation developed in this study, are valid only under the conditions for which this stationary phase approximation of the integration over the recording surface is valid.

The integration over the recording surface is a feature of the inversion formula, as it is in any Kirchhoff-like migration or inversion. The Kirchhoff modeling data is represented by an integral expression that features an integration over an arbitrary, but known, reflecting surface, divided into small segments. This type of ray-based modeling requires the assumption that the reflector be locally smooth with a known orientation at all locations along its length, such that there is a specular reflection of known directivity associated with each. When the expression describing the Kirchhoff data is substituted into the inversion integral as input data, and the order of these particular integrations reversed, the result is an expression requiring two spatial inte-

grations. The inner integral is that over the recording surface, and the outer is that over the reflector.

First, consider only the inner integral of this new expression, that is, take the reflecting point, or segment, represented by the outer integration, to be fixed. If the source location is also fixed, then evaluation of the inner, recording surface integral by stationary phase picks out the main energy-carrying path between the fixed source, the fixed reflection point, and the recording surface. This is just the specular path, and a stationary point is assigned to the recording surface at the point where this specular ray surfaces. Then, the outer integration implies that this is repeated for all points on the reflector, and both integrations together assign stationary points to each location on the recording surface where a specular ray surfaces.

Assuming that the input data are of some finite extent, or maximum offset, stationary points may appear on the input surface in various neighborhoods of the ends of the finite data aperture, which are the endpoints of the recording-surface integration that was approximated using stationary phase. As previously noted, contributions from stationary points that are too close to the endpoints of integration are not accurate. Thus, amplitude contributions from reflections that surface within some neighborhood of the ends of the spread are not accurate.

It is assumed that the inversion, and therefore the data mapping formula, is valid only when this trial integration is valid. So, contributions from scattered energy traveling along rays that surface in some neighborhood of the ends of the input data spread for *any* input data are assumed inaccurate.

In practice, the size of this neighborhood is often taken to be that of a Fresnel zone. However, a more rigorous criterion is possible for specific problems. One detailed analysis, given in Cohen (1990), shows that, for inversion of a typical seismic survey, the Fresnel zone is a good approximation of the erroneous neighborhood of the endpoints when the reflector has a shallow dip, but is too small to represent the size of this neighborhood for events with steep dip.

In the datuming problem, though, the useful aperture is defined on the output surface, which generally differs from the surface on which the input data are recorded. It was already noted in the discussions of the previous section and Figure 5.2 that each ray surfacing within the input spread passes through a receiver location on the datum inside the specular aperture. This implies that the rays which emerge within the erroneous neighborhood of each endpoint of the input spread define an erroneous neighborhood around each end of the specular aperture in the output data. So, the endpoints of the useful aperture on each datum are interior to those of the specular aperture. The size of the erroneous neighborhood of the endpoint on the output surface generally differs from that on the input surface, due to the “downward continuation” along the specular raypaths in this manner. The actual distortion depends on the ray geometry at hand.

In practice, artifacts resulting from finite endpoints are often reduced by tapering the input data amplitudes so that they go smoothly to zero at the ends of the aperture. However, while this generally reduces the artifacts, it also results in a sacrifice of

amplitude accuracy in the tapered region, possibly resulting in an even smaller useful aperture than that previously described.

5.3 Data mapping and stationary phase

As described in Chapter 2, Bleistein & Jaramillo (1997, 1999) derive equation (2.1) by cascading a modeling formula with an inversion formula, and the validity of the result depends on the validity of any asymptotics inherent in each component of the cascade.

The most basic condition for the use of leading-order stationary phase approximations is the assumption of a large parameter, which equates to an assumption of high frequency when applied to wave integrals. What constitutes high frequency is always governed by the scale of the problem. Let L_0 be a characteristic length scale in the integration variable, and Λ be the characteristic wavelength in the data. Then Bleistein et al. (1997) show that adopting a Rayleigh criterion of the form

$$L_0 \geq \frac{\Lambda}{4}, \quad (5.1)$$

is sufficient to justify the use of the leading-order stationary phase approximation. A more useful form of the condition is obtained by introducing f_0 and c_0 , the characteristic frequency for the data and a characteristic wavespeed for the medium, respectively, leading to the equivalent condition

$$\frac{4f_0L_0}{c_0} \geq 1. \quad (5.2)$$

Consider the inversion formula used in the data-mapping cascade. As was previously noted, this inversion is derived under the requirement that it produce correct reflectivity values when the input consists of Kirchhoff-approximate modeling data, including the requirement that a stationary phase approximation of the integral over the recording surface be valid. The above Rayleigh condition may be applied as a criterion for the validity of this approximation.

For the criterion to be met, all length scales L_0 along the recording surface must obey condition (5.2). One of these length scales is the radius of curvature, so let R_s be the radius of curvature of the recording surface at a given point. Then

$$R_s = \frac{1}{\kappa_s}, \quad (5.3)$$

where κ_s is the magnitude of the associated curvature vector, or simply the curvature, at the point. If (5.2) is assumed to hold, and L_0 is taken to be R_s , the resulting condition is

$$\kappa_s \leq \frac{4f_0}{c_0}. \quad (5.4)$$

This sets an upper limit on the curvature of the recording surface for validity of the inversion, and therefore, the data-mapping result. As is expected, the maximum allowable surface curvature increases with increasing frequency.

The nature of this limitation arises from the basic structure of the inversion technique, which assumes that the recording surface is smooth and that the wavefield is coherent between adjacent recording surface locations (Bleistein et al., 1997). In the limit where surface curvatures become large relative to the frequency of the incoming waves, the surface may appear to contain diffracting points, thus violating the assumption.

While condition (5.4) yields a general maximum on surface curvature, it is not the only asymptotic condition arising from the inversion. In Bleistein et al. (1997) it is shown that condition (5.2) also leads to the condition

$$2f_0L_0^2 \left| \frac{\partial^2 \phi}{\partial \xi^2} \right| \geq 1, \quad (5.5)$$

where ϕ is the phase and ξ the integration variable.

Condition (5.5) is also a validity condition on the integration over the recording surface, where, as before, ξ describes the receiver locations $\mathbf{x}(\xi)$ on the recording surface, and ϕ is the phase of the reflected wave. For the stationary phase approximation of the inversion integral, the shot location is fixed, as is that of the scatterer.

To evaluate condition (5.5), the second derivative of the phase can be defined in terms of other quantities. First, note that $\phi = \phi(\mathbf{x}(\xi))$, so

$$\phi'(\xi) = \frac{\partial \phi}{\partial x_i} \frac{\partial x_i}{\partial \xi} = \nabla_{\mathbf{x}} \phi \cdot \frac{\partial \mathbf{x}}{\partial \xi}, \quad (5.6)$$

and

$$\begin{aligned} \phi''(\xi) &= \frac{\partial \phi}{\partial x_i} \frac{\partial^2 x_i}{\partial \xi^2} + \frac{\partial x_i}{\partial \xi} \frac{\partial}{\partial \xi} \left(\frac{\partial \phi}{\partial x_i} \right) \\ &= \frac{\partial \phi}{\partial x_i} \frac{\partial^2 x_i}{\partial \xi^2} + \frac{\partial x_i}{\partial \xi} \frac{\partial x_j}{\partial \xi} \frac{\partial^2 \phi}{\partial x_i \partial x_j}, \end{aligned} \quad (5.7)$$

where a summation over repeated indices is implied. Consider the above expression to be evaluated at the stationary points, which are those $\mathbf{x}(\xi_0)$ satisfying $\phi'(\xi) = 0$. From equation (5.6), this stationarity condition is equivalent to

$$\frac{\partial \phi}{\partial \xi} = \nabla_{\mathbf{x}} \phi \cdot \frac{\partial \mathbf{x}}{\partial \xi} = 0. \quad (5.8)$$

Since the derivative of \mathbf{x} with respect to ξ is always tangent to the recording surface, this condition implies that stationarity occurs at points $\mathbf{x}(\xi_0)$ where $\nabla_{\mathbf{x}} \phi$ is normal to this surface.

So far, the actual form of the parameter ξ is unspecified, so relate it to a parameter s denoting arclength along the recording surface. Then,

$$\frac{\partial \mathbf{x}}{\partial s} = \frac{\partial \mathbf{x}}{\partial \xi} \frac{\partial \xi}{\partial s}, \quad (5.9)$$

and

$$\frac{\partial^2 \mathbf{x}}{\partial s^2} = \frac{\partial^2 \mathbf{x}}{\partial \xi^2} \left(\frac{\partial \xi}{\partial s} \right)^2 + \frac{\partial \mathbf{x}}{\partial s} \frac{\partial^2 \xi}{\partial s^2}. \quad (5.10)$$

Let $\hat{\mathbf{n}}$ be an upward-pointing vector normal to the recording surface, and dot this normal into both sides of equation (5.10) to give

$$\hat{\mathbf{n}} \cdot \frac{\partial^2 \mathbf{x}}{\partial s^2} = \hat{\mathbf{n}} \cdot \frac{\partial^2 \mathbf{x}}{\partial \xi^2} \left(\frac{\partial \xi}{\partial s} \right)^2, \quad (5.11)$$

where the second term from equation (5.10) vanishes because the derivative of \mathbf{x} with respect to arclength is always tangent to the surface. Note also that, at stationarity,

$$\frac{\partial \phi}{\partial \mathbf{x}} = \pm |\nabla_{\mathbf{x}} \phi| \hat{\mathbf{n}}. \quad (5.12)$$

So, if both sides of equation (5.11) are multiplied by the magnitude of the gradient of the phase, equation (5.12) allows the result to be written in summation form as

$$\frac{\partial \phi}{\partial x_i} \frac{\partial^2 x_i}{\partial \xi^2} = \pm |\nabla_{\mathbf{x}} \phi| \left(\frac{\partial s}{\partial \xi} \right)^2 \hat{n}_i \frac{\partial^2 x_i}{\partial s^2}. \quad (5.13)$$

Now, consider the travelttime isochron passing through each of the stationary points. This isochron is associated with travel along a raypath, through a fixed depth point, that surfaces at the stationary point, as previously described by the stationarity condition on the ξ integral. Since the isochron is associated with a particular stationary point, it can be considered a function of ξ . Further, let the arclength along the isochron is denoted by the parameter γ , and the points along the isochron by $\mathbf{y}(\gamma)$. Considering the fact that an isochron is a surface of constant phase, these parameters allow the isochron to be defined as

$$\phi(\mathbf{y}(\gamma), \xi) = C(\xi), \quad (5.14)$$

where $C(\xi)$ is a constant along the isochron. Since γ is a parameter along the isochron, the phase is constant with respect to γ , and

$$\phi'(\gamma) = \frac{\partial \phi}{\partial y_i} \frac{\partial y_i}{\partial \gamma} = 0, \quad (5.15)$$

at all points along the isochron. Furthermore, the second derivative of the phase with respect to γ is zero as well, giving

$$\begin{aligned} \phi''(\gamma) &= \frac{\partial \phi}{\partial y_i} \frac{\partial^2 y_i}{\partial \gamma^2} + \frac{\partial y_i}{\partial \gamma} \frac{\partial}{\partial \gamma} \left(\frac{\partial \phi}{\partial y_i} \right) \\ &= \frac{\partial \phi}{\partial y_i} \frac{\partial^2 y_i}{\partial \gamma^2} + \frac{\partial y_i}{\partial \gamma} \frac{\partial y_j}{\partial \gamma} \frac{\partial^2 \phi}{\partial y_i \partial y_j} = 0. \end{aligned} \quad (5.16)$$

The isochron and the recording surface share a single common point, the stationary point, where $\mathbf{y} = \mathbf{x}$. The gradient of the phase, $|\nabla_{\mathbf{x}}\phi|$, is always normal to the isochron, by definition. At a stationary point, the required condition is that this gradient be collinear with the normal to the recording surface. Thus, the isochron is tangent to the recording surface there. In this case, then, at each stationary point,

$$\frac{\partial y_i}{\partial \gamma} = \frac{\partial x_i}{\partial s} = \frac{\partial x_i}{\partial \xi} \left(\frac{\partial \xi}{\partial s} \right). \quad (5.17)$$

Using this result and letting $\mathbf{y} = \mathbf{x}$, the second derivative expression in equation (5.16) can be rewritten as,

$$\frac{\partial \phi}{\partial x_i} \frac{\partial^2 x_i}{\partial \gamma^2} + \frac{\partial x_i}{\partial \xi} \frac{\partial x_j}{\partial \xi} \left(\frac{\partial \xi}{\partial s} \right)^2 \frac{\partial^2 \phi}{\partial x_i \partial x_j} = 0, \quad (5.18)$$

or equivalently, using equation (5.12),

$$\frac{\partial x_i}{\partial \xi} \frac{\partial x_j}{\partial \xi} \frac{\partial^2 \phi}{\partial x_i \partial x_j} = \mp |\nabla_{\mathbf{x}}\phi| \left(\frac{\partial s}{\partial \xi} \right)^2 \hat{n}_i \frac{\partial^2 x_i}{\partial \gamma^2}, \quad (5.19)$$

at each stationary point.

Finally, then, the second-derivative expression at each stationary point given in equation (5.7) can be rewritten using equation (5.13) to rewrite the first term, and equation (5.19) to redefine the second term, giving

$$\phi''(\xi) = |\nabla_{\mathbf{x}}\phi| \left(\frac{\partial s}{\partial \xi} \right)^2 \left[\pm \hat{n}_i \frac{\partial^2 x_i}{\partial s^2} \mp \hat{n}_i \frac{\partial^2 x_i}{\partial \gamma^2} \right]. \quad (5.20)$$

The two terms in the brackets have undetermined but opposite sign, owing to the use of equation (5.12) in the determination of the right sides of equations (5.13) and (5.19). Thus, combining the signs in front of the equation, and collapsing the summations to vector form, gives

$$\phi''(\xi) = \pm |\nabla_{\mathbf{x}}\phi| \left(\frac{\partial s}{\partial \xi} \right)^2 \left[\hat{\mathbf{n}} \cdot \frac{\partial^2 \mathbf{x}}{\partial s^2} - \hat{\mathbf{n}} \cdot \frac{\partial^2 \mathbf{x}}{\partial \gamma^2} \right]. \quad (5.21)$$

Substituting the absolute value of this derivative into equation (5.5) yields a validity condition

$$2f_0 L_0^2 |\nabla_{\mathbf{x}}\phi| \left(\frac{\partial s}{\partial \xi} \right)^2 \left| \hat{\mathbf{n}} \cdot \frac{\partial^2 \mathbf{x}}{\partial s^2} - \hat{\mathbf{n}} \cdot \frac{\partial^2 \mathbf{x}}{\partial \gamma^2} \right| \geq 1. \quad (5.22)$$

The second derivative in s in condition (5.22) is the curvature vector for the recording surface at the stationary point. The second derivative in γ is the curvature vector of the isochron or wavefront of the upcoming wave at the stationary point. Define κ_s and κ_ϕ to be the magnitudes of these recording-surface and wavefront curvature vectors, respectively. Since the curvature vector for the recording surface is normal to this surface by definition, and the curvature vector for the wavefront is normal to

the recording surface at stationarity, each dot product of a second derivative with the surface normal $\hat{\mathbf{n}}$ in the above condition is equal to the appropriate curvature magnitude when the curvature vector is aligned with the surface normal, and minus the appropriate magnitude when the curvature vector points opposite to the surface normal.

Where there is no multipathing, the isochron curvature vector of the upcoming waves is always downward pointing. Therefore, this vector is always aligned opposite to the upward pointing surface normal at stationarity, and the dot product in equation (5.22) is always negative, or

$$\hat{\mathbf{n}} \cdot \frac{\partial^2 \mathbf{x}}{\partial \gamma^2} = -\kappa_\phi . \quad (5.23)$$

The curvature vector along the recording surface, though, may point in either direction. Therefore, this curvature vector may be either aligned with or aligned opposite to the surface normal, and the dot product may be either positive or negative, depending on the shape of the recording surface at the given stationary point. Here, define the recording surface as *convex-up* when the curvature vector points upward (a synclinal sense of curvature), and *convex-down* when it points downward (an anticlinal sense of curvature). If the surface is convex-up at a given point, the normal and curvature vectors are aligned, and the dot product is positive. If the surface is convex-down, however, the normal and curvature vectors are oppositely directed, and the dot product is negative. Specifically,

$$\hat{\mathbf{n}} \cdot \frac{\partial^2 \mathbf{x}}{\partial s^2} = \begin{cases} -\kappa_s & \text{convex-down surface} \\ \kappa_s & \text{convex-up surface} \end{cases} . \quad (5.24)$$

Using these results for the dot products and taking into account the absolute value of their difference, the validity condition (5.22) is, for each point along the recording surface, equivalent to

$$2f_0 L_0^2 |\nabla_{\mathbf{x}} \phi| \left(\frac{\partial s}{\partial \xi} \right)^2 M(\kappa_s, \kappa_\phi) \geq 1 , \quad (5.25)$$

where

$$M(\kappa_s, \kappa_\phi) \equiv \begin{cases} |\kappa_s - \kappa_\phi| & \text{convex-down surface} \\ |\kappa_s + \kappa_\phi| & \text{convex-up surface} \end{cases} . \quad (5.26)$$

Condition (5.25) sets a lower bound on all length scales L_0 associated with the recording surface, including the spread length and the radius of curvature.

There are several factors arising from stationary phase approximations that influence validity through condition (5.25). One of these is the requirement that contact between the recording surface and the upcoming wavefront occur at only simple, isolated stationary points. When the contact between the wavefront and the surface is of high enough order that the second derivative of the phase is zero, leading-order stationary phase breaks down.

At points where it is convex-up, the recording surface has the opposite sense of curvature than the upcoming wavefront, and contact between the two always occurs at a single stationary point. Thus, the issue of the order of contact does not influence validity. This is consistent with the fact that, in this case, condition (5.25) is a function of the sum of the curvature magnitudes, and, therefore, the relative values of these magnitudes do not greatly influence the condition.

At points where it is convex-down, however, the recording surface and the upcoming wavefront have the same sense of curvature, and the possibility of high-order contact is a relevant issue for validity. When the curvature magnitudes are significantly different, contact between the wavefront and the surface is at a single point at a single time, yielding an isolated stationary point. Since the wavefront and the surface have the same sense of curvature in this case, though, the order of contact increases as the curvature magnitudes become close in value. When the contact is of high enough order such that the second derivative of the phase is zero, leading-order stationary phase breaks down. This is consistent with the fact that at points where the recording surface is convex-down, the validity condition (5.25) is a function of the difference of the curvature magnitudes, and, therefore, the relative values of the curvatures may have a significant influence on validity.

Note that while the maximum curvature of the recording surface is known, the maximum isochron curvature at the surface depends on details of the wave propagation. Consequently, in practice, this quantity must be estimated using whatever *a priori* information about the wavespeed profile and target depths is available to produce a “worst case” isochron curvature at the surface.

Now, consider similar conditions arising from the modeling formula in the data-mapping cascade. The modeling scheme is characterized by an integration over the reflecting surfaces, and produces Kirchhoff-approximate model data. In a similar procedure to that described for the inversion, the derivation of the modeling formula includes a trial integration of an intermediate formula, where the integration over the reflecting surfaces is approximated via stationary phase. The result of this trial integration is then compared with the correct result, and used to derive the final formula. Thus, the modeling formula is valid only when a stationary phase approximation along the reflector is valid.

Because the modeling and inversion formulas are related, and derived in analogous ways, the analysis of this problem is similar to that performed above for the inversion. In fact, the resulting conditions on the reflecting surface are analogous to those derived above for the reflecting surface. In particular, the problem at the reflector is simply that at the recording surface turned upside-down. For inversion, validity conditions depend upon the interaction of upcoming wavefronts and the recording surface. For the modeling formula, the conditions depend upon the same interactions between the downgoing wavefronts and the reflecting surface.

So, the same Rayleigh derived conditions (5.1) and (5.2) apply to this stationary phase integration, except now the characteristic length scale L_0 is measured along the reflecting surface, and all length scales related to this surface must obey the condition.

As before, the radius of curvature along the reflector is considered to be one of these length scales. This results in a condition analogous to that in the previous case, or

$$\kappa_\alpha \leq \frac{4f_0}{c_0}, \quad (5.27)$$

where κ_α is the curvature at a given point along the reflector. This sets an upper limit on the curvature of the reflecting surface for the validity of the modeling formula, and therefore, on the data-mapping result. Note that as long as the characteristic frequency and wavespeed are assumed to be the same for the incident and reflected wavefields, the upper bound on the curvatures of both the reflecting and recording surfaces, expressed in this condition and in condition (5.4), are the same, and have the same frequency dependence.

This arises for a reason analogous to that for inversion, namely that the modeling technique assumes that the reflecting surface is smooth, and that the wavefield is coherent between adjacent points. In the limit where the curvatures become large relative to the wavelength of the incident waves, the surface appears to contain diffracting points, and the assumption is violated.

Furthermore, condition (5.5) holds where ξ is replaced by α , an integration variable over the reflecting surface. The subsequent analysis is identical to that for the inversion, except that the incident wavefield and rays are considered instead of the scattered, and the stationary points from this integration appear on the reflecting surface, as opposed to the recording surface. The result is analogous to condition (5.25), and is defined for a given point along the reflector. If κ_α is the magnitude of the curvature vector of the reflecting surface, and κ_ϕ is the magnitude of the curvature vector of the downgoing wavefront, at the stationary point, the condition is

$$2f_0L_0^2 |\nabla_{\mathbf{x}}\phi| \left(\frac{\partial s}{\partial \xi} \right)^2 N(\kappa_\alpha, \kappa_\phi) \geq 1, \quad (5.28)$$

where

$$N(\kappa_\alpha, \kappa_\phi) \equiv \begin{cases} |\kappa_\alpha - \kappa_\phi| & \text{convex-up reflector} \\ |\kappa_\alpha + \kappa_\phi| & \text{convex-down reflector} \end{cases}. \quad (5.29)$$

This result is directly analogous to that at the recording surface. The definition (5.29) contains a difference, however, with respect to the analogous definition (5.26) for the recording surface. Specifically, that the association of the difference or sum of curvatures with either a convex-up or convex-down surface is reversed.

In the discussion of the previous validity condition (5.25), it is explained that this condition depends on difference of curvatures when the wavefront and the recording surface have the same sense of curvature, and high-order contact is possible. In that case, the wavefronts are assumed to be upcoming and convex-down. Therefore, condition (5.25) depends on the difference of curvatures when the recording surface is also convex-down.

The same physical situation occurs at the reflector, as governed by condition (5.28), except that the waves are now assumed to be down-going and convex-up, and

high-order contact is possible only when the reflector has the same sense of curvature. Therefore, condition (5.28) depends on the difference of curvatures when the reflector is convex-up.

So, condition (5.28) sets a lower bound on all length scales L_0 associated with the reflector. At points on the reflector where the curvature is convex-up, condition (5.28) is a function of the difference of curvatures of the down-going wavefront and the reflecting surface at each stationary point on the reflector, and the possibility of high-order contact between the wavefront and the reflector is an issue for validity.

Because neither the maximum reflecting surface curvature or the typical isochron curvature at the reflector are generally known at the time datuming is applied, in practice, a useful validity condition is obtained only by estimating these quantities using whatever *a priori* information concerning the subsurface is available.

These results imply that the data mapping result is fully valid only if the four validity conditions, given by equations (5.4), (5.25), (5.27), and (5.28), hold for all relevant length scales and at all points along the appropriate surfaces, with respect to any and all interactions between waves and these surfaces. In Chapter 6, some errors that result in data-mapping amplitudes due to violations of these conditions are shown using synthetic data examples.

Chapter 6

COMPARISONS WITH OTHER DATUMING METHODS

In the preceding chapters, the data-mapping method is shown to provide a general mathematical procedure for performing true-amplitude downward continuation in a heterogeneous medium, at least in the sense that the amplitudes are consistent with downward continuation of the input data through the given wavespeed model. Data mapping is not the only available method to extrapolate data, and it is desirable to compare data mapping to more familiar approaches to downward continuation.

It is demonstrated in this chapter that the 2.5D data-mapping extrapolation differs from more familiar Kirchhoff methods in two significant ways. First, many familiar Kirchhoff datuming methods explicitly assume a horizontal, or approximately horizontal, recording surface (Berryhill, 1979; Bevc, 1995). These methods are, at best, approximate when topographic variations are small. Data mapping is accurate for a topographic recording surface provided that the appropriate validity conditions of Chapter 5 are not violated. This implies that an important issue for study is whether the data-mapping method is able to produce accurate amplitudes for a larger degree of surface variation than other Kirchhoff methods. Second, unlike data mapping, common adaptations of 3D Kirchhoff downward-continuation methods to line data are not dynamically correct, that is, they do not preserve amplitudes in point-source data. This is an important consideration for any application of the method where amplitude preservation is required.

Therefore, this chapter employs both mathematical discussions and synthetic models to show how the results of the 2.5D data-mapping method compare with those of Kirchhoff-based datuming of line data in constant-wavespeed media. Comparisons of amplitude and amplitude variation with offset (AVO) results in various models are discussed, both with and without surface topography.

6.1 Analytic comparisons

To understand the differences between the 2.5D data-mapping approach and more familiar Kirchhoff methods for downward continuation, an analytic comparison is useful. A commonly used family of 3D Kirchhoff methods for downward continuation assume a constant-wavespeed reference medium, choose an appropriate free-space Green's function, and then apply Green's theorem to a hemispherical volume. This choice of volume allows the use of the method of images to eliminate the derivative of the field from the integrand, but limits the accuracy of the results for topographic recording surfaces by explicitly assuming a horizontal recording surface.

A full, 3D extrapolation is often not practical, and a method for downward continuation of single lines of data, where the calculation is performed entirely in a 2D plane beneath a survey line, is desirable. Adaptations of the 3D Kirchhoff method to line data are performed in Berryhill (1979, 1984), Bevc (1995), and Salinas (1997). In these studies, the above Green's-theorem approach is first used to obtain a 3D downward extrapolation formula. Since only the upper surface of the hemisphere is assumed to contribute to the output field, this 3D integral has only one spatial integration, namely a two-dimensional integral over the recording surface, that is, over the input data array.

At this point, it is assumed that the data are independent of one coordinate direction on the recording surface, say x_2 . In this case, only the known Green's function in the integral representation depends on x_2 , and the x_2 dependence is integrated out of the surface integral using stationary phase (Bevc, 1995; Salinas, 1997), or, alternatively, by rewriting the integral representation as a time domain convolution (Berryhill, 1979). This results in an expression that requires an integration over a single line of input data only.

Unfortunately, the assumption that the data are independent of x_2 is incorrect. The point-source Green's function in a constant-background medium is a function of the radial distance from the source point, and is, therefore, a function of x_2 . Thus, the reflection of an incident wave from a subsurface structure is also a function of x_2 , even for the simplest of reflection geometries. Consequently, this calculation in the out-of-plane direction is incorrect, and does not produce an expression that preserves 3D geometrical spreading amplitudes.

The data-mapping approach, however, is based on a correct 2.5D inversion procedure. In that method, the subsurface is assumed to be independent of the out-of-plane variable, again, x_2 . Then, a single line of data provides information about parallel lines of data with *identical source/receiver configurations*. Now, despite 3D spreading, the data for this *ensemble* of experiments is independent of x_2 . Starting from a 3D inversion formula and incorporating the appropriate Beylkin determinant for this ensemble of experiments results in a formula in which the operator depends in x_2 , but the data do not. In this case, the out-of-plane stationary phase is valid, and provides an expression that requires an integration over a line of data only, but properly incorporates 3D geometrical spreading into its characterization of the data. Details of the implementation of this inversion in the data-mapping platform are found in Bleistein & Jaramillo (1997, 1999).

It is important to note that the methods developed by the above-cited authors is kinematically correct, that is, their phase properly incorporates in in-plane traveltimes of the Green's function and the data. However, the amplitudes that they predict do not properly account for out-of-plane geometrical spreading in the data, and, therefore, are not 2.5D amplitudes as previously defined in this study.

To verify these statements, and to understand how the results of these methods compare with those of the 2.5D data-mapping downward continuation, consider a direct comparison of the extrapolation integrals. Bevc (1995) and Salinas (1997) use

the above procedure and a far-field assumption to arrive at the same, frequency-domain, downward-continuation integral. Since the data-mapping integrals are the result of stationary phase approximations in the frequency domain, as well, they are most easily compared to this result, as opposed to the expression in Berryhill (1979) that has an integrand in the form of a time-domain convolution.

So, the following discussions compare the data mapping method with *Kirchhoff datuming*, where this term is used to specifically refer to the datuming procedure described in Bevc (1995) and Salinas (1997), as a representative example of this class of familiar Kirchhoff methods, incorrectly adapted to single lines of survey data in the manner described above. Again, since the extrapolation of sources is essentially the same process as that of receivers, only the downward continuation of receivers given a fixed source is explicitly addressed in this discussion.

Following the results of Bevc (1995), downward continuation of receivers using Kirchhoff datuming for line data is given by

$$P(\mathbf{r}, \omega) \approx \frac{1}{\sqrt{2\pi c}} \int \frac{1}{\sqrt{r}} \frac{\partial r}{\partial n} \sqrt{i\omega} P(\mathbf{r}_S, \omega) e^{-i\omega r/c} dx, \quad (6.1)$$

where r is the distance between the output location being evaluated and the recording surface at each input receiver location. The derivative $\partial r/\partial n$ is that of the emerging ray path with respect to the normal to the recording surface at the input location. However, because the derivation explicitly assumes a horizontal recording surface, it is implied that this derivative is taken with respect to a vertical normal. The result may be approximate for a topographic surface, nevertheless, if the variations on that surface are sufficiently small and the factor $\partial r/\partial n$ is taken with respect to the normal to the actual surface, instead of the vertical (Berryhill, 1979). In fact, this approximation is made in the Kirchhoff-datuming examples used for comparison later in this study. Therefore, the normal derivative is left in this general form in the equations.

In order to make a direct comparison of the Kirchhoff-datuming and data-mapping results, it is helpful to write the Kirchhoff-datuming expression in terms of the variables used in the data-mapping derivations. First, consider the case where the recording surface is horizontal and located at $z = 0$. Then,

$$r = r_{IG} - r_{OG}, \quad \frac{\partial r}{\partial n} = \cos \theta = \frac{\bar{x}_3}{r_{IG}}, \quad (6.2)$$

noting that the θ refers to the emergence angle of the ray with respect to the vertical, and not the ray-opening angle as defined in the general derivations earlier in this paper. Further, the lateral x -direction is coincident with the horizontal recording surface, so x is directly replaced by ξ_I such that $dx = d\xi_I$. That is, the Jacobian of transformation between x and ξ_I is unity. These results allow equation (6.1) to be written as

$$U_O(\xi_O, \omega) \approx \frac{1}{\sqrt{2\pi c}} \int \frac{\bar{x}_3}{r_{IG}} \frac{\sqrt{i\omega} u_I(\xi_I, \omega)}{\sqrt{|r_{IG} - r_{OG}|}} e^{-i\omega(r_{IG} - r_{OG})/c} d\xi_I. \quad (6.3)$$

Here, the upper case U_O indicates that the result is from the Kirchhoff-datuming method. Rewriting the phase in terms of constant-wavespeed traveltimes produces

$$U_O(\xi_O, \omega) \approx \frac{1}{\sqrt{2\pi c}} \int \frac{\bar{x}_3}{r_{IG}} \frac{\sqrt{i\omega} u_I(\xi_I, \omega)}{\sqrt{|r_{IG} - r_{OG}|}} e^{-i\omega t_I} e^{i\omega t_O} d\xi_I, \quad (6.4)$$

where t_I and t_O represent the constant-wavespeed traveltimes for the input and output receiver locations, respectively. Now, perform the inverse Fourier transform from ω to t_O , yielding

$$U_O(\xi_O, t_O) \approx \frac{1}{\sqrt{2\pi c}} \frac{1}{2\pi} \iint \frac{\bar{x}_3}{r_{IG}} \frac{\sqrt{i\omega} u_I(\xi_I, \omega)}{\sqrt{|r_{IG} - r_{OG}|}} e^{-i\omega t_I} d\omega d\xi_I. \quad (6.5)$$

For the sake of comparison, write this in more compact form, as

$$U_O(\xi_O, t_O) \approx \iint F(\xi_O, t_O) d\omega d\xi_I, \quad (6.6)$$

where $F(\xi_O, t_O)$ is the integrand of equation (6.5).

The analogous data-mapping formula for downward continuation from a horizontal surface is given by equation (3.8) with $G = \bar{x}_3$. Rewriting the data-mapping equation in terms of the Kirchhoff-datuming integrand F gives

$$u_O(\xi_O, t_O) = \iint \frac{\sqrt{r_S + r_{IG}}}{\sqrt{r_S + r_{OG}}} F(\xi_O, t_O) d\omega d\xi_I, \quad (6.7)$$

which is equivalent to equation (3.8) in this case.

This expression shows that, for a horizontal acquisition surface, the Kirchhoff-datuming formula is identical to the data-mapping integral in terms of kinematics, but does not contain all of the factors necessary to correctly calculate amplitudes. The amplitude weighting factors in the integrands differ by a function of the path lengths to and from the given stationary point, specifically, by the factor

$$\frac{\sqrt{r_S + r_{IG}}}{\sqrt{r_S + r_{OG}}}. \quad (6.8)$$

This factor is identified by 2.5D theory as the correction for out-of-plane geometrical spreading (Bleistein, 1986). Apparently, the incorrect procedure used to adapt the 3D integral to line data in Kirchhoff datuming yields the correct in-plane calculation, but is missing exactly the correction for out-of-plane spreading.

The influence of factor (6.8) is greater when the datuming depth approaches that of the reflector, and lesser when the datum is closer to the recording surface, all other things being equal. While the value of this factor becomes close to unity when the distance between the recording surface and the datum is small compared to the reflector depth, it is never equal to one for all elements of the summation when the input and output surfaces are different. Thus, the Kirchhoff-datuming and data-mapping methods are not equivalent.

Note that the Kirchhoff-datuming result requires only the lengths r of paths connecting points on the recording surface with points on the datum, and the traveltimes along them. Evaluation of the amplitude factor (6.8) in the data mapping result, however, requires the lengths of paths connecting both the datum and recording surfaces with stationary points that lie below the datum, associated with the scattering surfaces. Thus, a greater knowledge of the subsurface, as well as additional computation of raypaths through it, is required to apply the data-mapping method, as compared to the computationally less expensive, but dynamically less accurate, Kirchhoff-datuming method.

So, when the recording surface is horizontal, the two methods differ only by the factor (6.8) in the integrand. Now, consider the case where the recording surface contains some topographic variation. As previously noted, the approach used to derive the Kirchhoff-datuming result has the limitation that it explicitly requires that the recording surface be horizontal, but it may be approximate for a recording surface of small topographic variation, provided that the factor $\partial r/\partial n$ is taken with respect to the normal of the actual surface, instead of to a vertical normal as prescribed by the assumption. For this approximation to be useful, the surface variation must be small enough that an integration over the actual recording surface can be approximated by an integration over the lateral variable x . That is, the Jacobian of transformation between x and ξ_I must be near unity. In this case, $dx \approx d\xi_I$, and the resulting integral is analogous to equation (6.5), where the normal derivative is retained to allow evaluation with respect to the actual surface, or

$$\bar{U}_O(\xi_O, t_O) \approx \frac{1}{\sqrt{2\pi c}} \frac{1}{2\pi} \iint \frac{\partial r}{\partial n} \frac{\sqrt{i\omega} u_I(\xi_I, \omega)}{\sqrt{|r_{IG} - r_{OG}|}} e^{-i\omega t_I} d\omega d\xi_I. \quad (6.9)$$

Here the field is designated by \bar{U}_O to distinguish the small-topography approximation from the previous, horizontal surface case. Again, for the sake of comparison, write this in more compact form, as

$$\bar{U}_O(\xi_O, t_O) \approx \iint \bar{F}(\xi_O, t_O) d\omega d\xi_I. \quad (6.10)$$

where $\bar{F}(\xi_O, t_O)$ is the integrand of equation (6.9).

The analogous data-mapping formula for downward continuation from a topographic surface is given by equation (3.8). Rewriting the data-mapping equation in terms of the Kirchhoff-datuming integrand \bar{F} gives

$$u_O(\xi_O, t_O) = \iint \frac{G(\bar{x}_1, \bar{x}_3)}{r_{IG}} \frac{\sqrt{r_S + r_{IG}}}{\sqrt{r_S + r_{OG}}} \left(\frac{\partial r}{\partial n} \right)^{-1} \bar{F}(\xi_O, t_O) d\omega d\xi_I. \quad (6.11)$$

which is equivalent to equation (3.8) in the topographic case.

Now the two methods differ by more than just factor (6.8). Specifically, equation (6.11) implies that the weighting factor in the data-mapping integral,

$$\frac{G(\bar{x}_1, \bar{x}_3)}{r_{IG}} \frac{\sqrt{r_S + r_{IG}}}{\sqrt{r_S + r_{OG}}}, \quad (6.12)$$

is approximated in the Kirchhoff-datuming integral by the factor

$$\frac{\partial r}{\partial n} = \cos \Theta, \quad (6.13)$$

where Θ is the angle between the surface normal and the upcoming ray at the given input receiver location. The factor (6.13) is said here to approximate the factor (6.12), because these two factors are not generally equal. Furthermore, the difference in these factors is not due to factor (6.8) alone. Even though the factors $G(\bar{x}_1, \bar{x}_3)/r_{IG}$ and (6.13) are equal when the recording surface is horizontal, they do not generally have the same value when the recording surface contains any topographic variation.

For example, consider the topographic model from Chapter 4 shown in Figure 4.6. In this simple, single-reflector model, there is a single, easily determined specular ray between the source and each receiver. Figure 6.1 shows the numerical values of the above factors at each output receiver location, calculated along the associated specular ray, for three datuming surfaces. In each plot, the solid black curve is the value of the data-mapping amplitude factor (6.12), and the dashed curve is that of the Kirchhoff-datuming scale factor (6.13). The two curves have a similar character, but there is a sizable difference between them.

While evaluation of the integrals considers more rays than just the specular paths, both data mapping and Kirchhoff datuming are high-frequency methods, and the most important contributions to the integration are, therefore, assumed to be associated with specular rays. So, this comparison is sufficient to demonstrate not only that the factors (6.12) and (6.13) are not equivalent, but also that they can have significantly different values for the main energy-carrying rays in even this simple model.

Further, the grey dotted curve in Figure 6.1 shows the value of the factor $G(\bar{x}_1, \bar{x}_3)/r_{IG}$ for the same specular paths. Comparison with the dashed curve demonstrates that this factor alone is not generally equivalent to factor (6.13) either. Therefore, the difference in the integrands for a topographic recording surface is not due only to factor (6.8).

So, the data-mapping and Kirchhoff-datuming integrals are not equivalent, even in a constant-wavespeed medium, as illustrated by the difference in the factors (6.12) and (6.13) in their integrands. This implies that amplitudes from the Kirchhoff-datuming approximation are not generally equal to those given by the data-mapping method. Synthetic examples, shown in the next section, compare the results of these two calculations and the influences of these factors.

6.2 Comparison for synthetic data

Here, the influence of the differing integrands in the expressions describing the data-mapping and Kirchhoff-datuming methods is examined using a set of simple synthetic models in a constant-wavespeed medium. As previously noted, the kinematic results of the two methods are identical, so the comparisons focus on the preservation of amplitude.

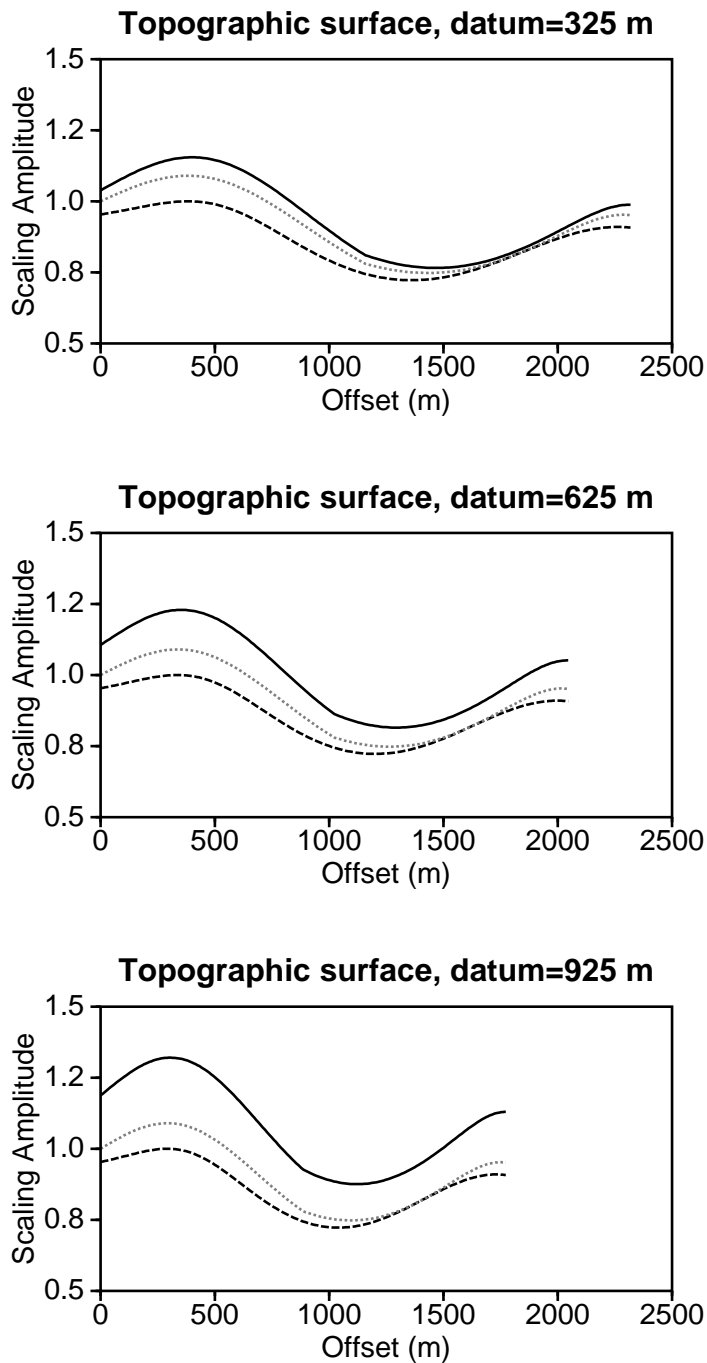


FIG. 6.1. Amplitude scaling for data-mapping and Kirchhoff-datuming, for specular rays to a sinusoidal recording surface of 2500-m wavelength and 125-m amplitude.

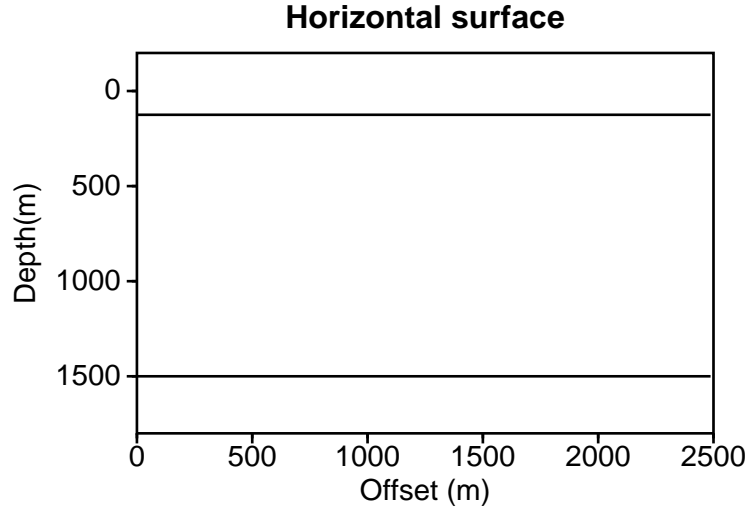


FIG. 6.2. Subsurface model with a horizontal recording surface at 125-m depth and a horizontal reflector, in a constant-wavespeed medium.

All data from the models in this section are common-source gathers, collected over 201 receivers, starting at zero-offset with a uniform lateral spacing of 12.5 m. Unless otherwise specified, the wavelets have a 20-Hz peak frequency. Note that, as in previous examples, the source is placed at a nonzero depth so that all points on the topographic surfaces are defined with a non-negative depth, to accommodate the computer code. Downward continuation of receivers is performed such that the data are extrapolated to a horizontal datum with the same lateral receiver configuration.

First, consider a model with a horizontal recording surface and a horizontal reflector at a depth of 1500 m. The wavespeed between them is a constant 2000 m/s, as shown in Figure 6.2. The source and recording surface are placed at 125-m depth for direct comparison to the next set of models. The three horizontal datum surfaces of interest are at 325-m, 625-m, and 925-m depth.

Figure 6.3 shows show peak amplitude versus offset for the downward-continued data on the three datum surfaces. The grey curve is the true amplitude for the output datum, the solid black curve shows the data-mapping result, and the dashed black curve shows the result of the Kirchhoff-datuming calculation. The data-mapping method yields accurate amplitudes within a particular useful aperture on each datum. The Kirchhoff-datuming results appear to be a good approximation of the true amplitudes when the datum depth is shallow, but become increasingly too low as the datum depth increases. This is consistent with equation (6.7), where it is shown that when the recording surface is horizontal, Kirchhoff datuming differs from data mapping by the factor (6.8) in the integrand, a factor which is near unity when the depth of the datum surface is small compared to that of the reflector, but increases in value

as the datum is moved closer to the reflector. Nevertheless, the Kirchhoff-datuming amplitudes appear to have roughly a correct amplitude variation with offset. In this model, therefore, the influence of factor (6.8) on the integration is that of an approximately constant shift in amplitude.

It has already been noted that when the acquisition surface is not horizontal, the methods differ by more than just factor (6.8) in the integrands. The data-mapping method is also valid only within certain limitations on the surface, as discussed in Chapter 5. The Kirchhoff-datuming approach is also limited by assumptions on the shape of the recording surface, most notably the requirement that the variation on the surface be small enough that integral over the recording surface can be approximated by a horizontal, lateral integration, as previously discussed.

To compare the accuracies of two methods with respect to datuming from a topographic recording surface, consider the same model, except that the surface is now a sinusoid of 125-m amplitude, with a wavelength equal to 2500 m, the length of the receiver spread. This model is shown in Figure 6.4, and peak amplitudes versus offset for the same three datuming depths are shown in Figure 6.5. The data mapping-result is accurate within about the same useful aperture as in the horizontal case. The Kirchhoff-datuming result, however, differs by more than just a downward shift in amplitude, but also shows an increased deviation from the correct offset dependence displayed by the data-mapping result.

In the case of a non-horizontal recording surface, the factor (6.13) appears in the Kirchhoff-datuming integrand in place of the factor (6.12) in the data-mapping integrand. The interaction of these factors in this model causes a degradation in the Kirchhoff-datuming result in both amplitude and amplitude variation with offset. Such a departure from the true amplitude variation can be an important concern for applications where an analysis of amplitude variation with offset is required.

Next, consider the same subsurface model, but one in which the sinusoidal variation on the recording surface is made more severe by decreasing the wavelength of the topography to 1250 m, so that the receiver spread spans two wavelengths of topographic variation. The amplitude of the variation is kept at 125 m. This model is depicted in Figure 6.6.

Figure 6.7 shows the peak amplitudes for this model, at the same datuming depths as in the previous example, and there are now small errors in the data-mapping results. The largest errors occur near the midpoint of the useful aperture in each plot, and smaller deviations appear in regions at roughly 25% and 75% of the length of the useful aperture. In the 325-m datum plot, these regions are centered at offsets of approximately 550 m, 1150 m, and 1700 m. For the deeper datums, the locations change as the length of the useful aperture is reduced, but the relative locations of the erroneous regions inside the aperture remains the same. The Kirchhoff-datuming result displays inaccurate amplitudes in the same regions of the useful aperture, however, these errors are sizeable with respect to those observed in the data-mapping results.

Errors in the data-mapping result are generally attributed to the validity con-

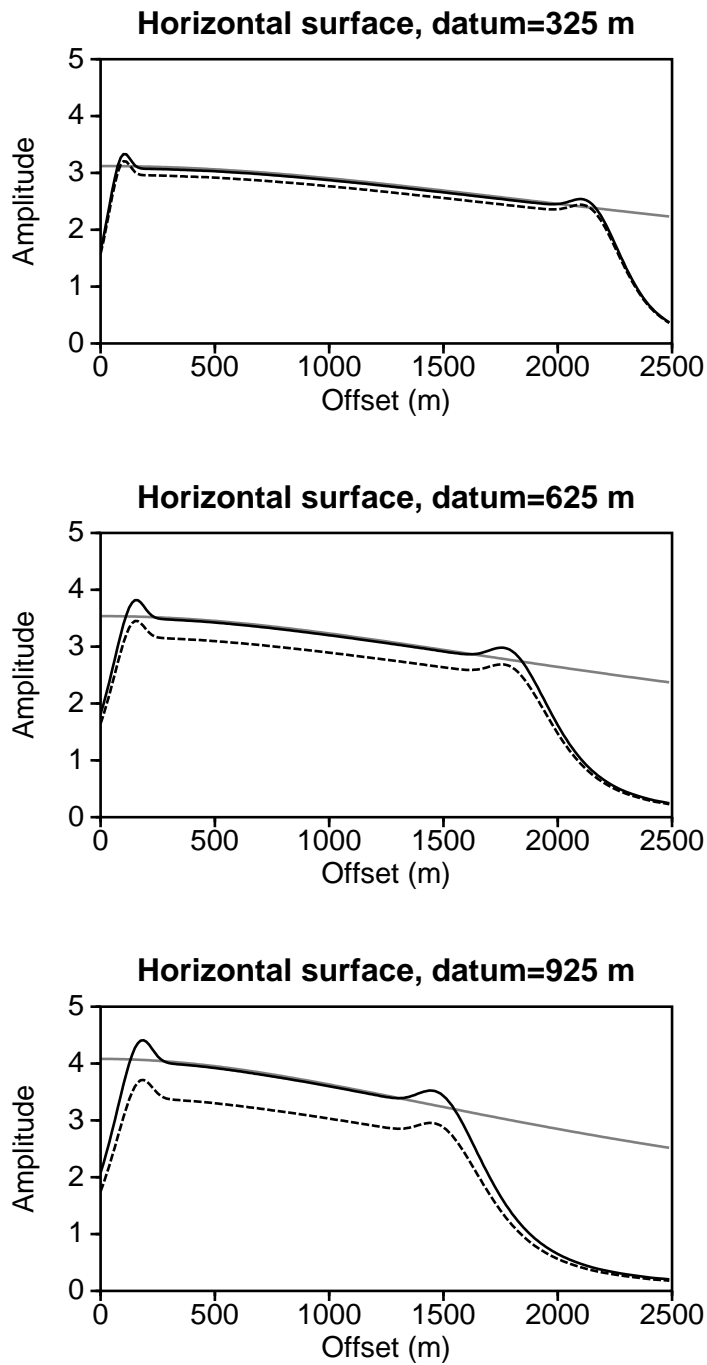


FIG. 6.3. Comparison of peak amplitudes for data mapping and Kirchhoff datuming of receivers from a horizontal recording surface over a horizontal reflector.

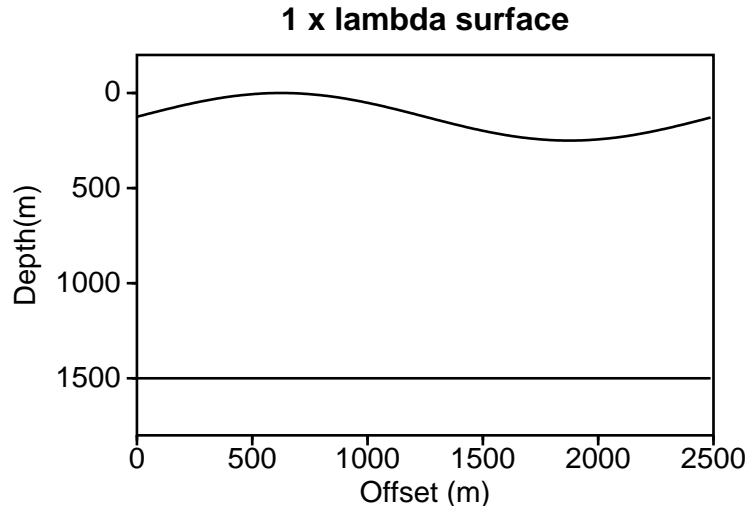


FIG. 6.4. Subsurface model with a sinusoidal recording surface of 2500-m wavelength and 125-m amplitude and a horizontal reflector, in a constant-wavespeed medium.

ditions that arise from asymptotics, as discussed in detail in Chapter 5. Kirchhoff datuming is also an asymptotic method, so it is subject to similar conditions. If the errors in both calculations observed in Figure 6.7 arise from violation of these asymptotic conditions with respect to the recording surface topography, then this fact should be evident from violation of condition (5.25), where the length scale in question is the radius of curvature of this surface. So, let

$$L_0 = R_s = \frac{1}{\kappa_s}, \quad (6.14)$$

where, as before, R_s is the radius of curvature, and κ_s is the magnitude of the associated curvature vector, at each point along the recording surface. Using this in condition (5.25) yields a condition specific to recording surface curvature, or

$$V_s \equiv \frac{2f_0 |\nabla_{\mathbf{x}} \phi|}{\kappa_s^2} \left(\frac{\partial s}{\partial \xi} \right)^2 M(\kappa_s, \kappa_\phi) \geq 1, \quad (6.15)$$

where $M(\kappa_s, \kappa_\phi)$ is defined in equation (5.26). Violations of validity with respect to recording surface curvature occur for upcoming rays and their associated locations on the recording surface if $V_s < 1$.

The condition is also a function of frequency, so the choice of f_0 must be low enough to insure that the condition holds for all the significant low frequencies in the data. This data was generated with a Ricker wavelet of 20-Hz peak frequency. This wavelet has a fairly broad spectrum, and $f_0 = 10$ Hz is a reasonable choice to represent the significant low frequencies in the data.

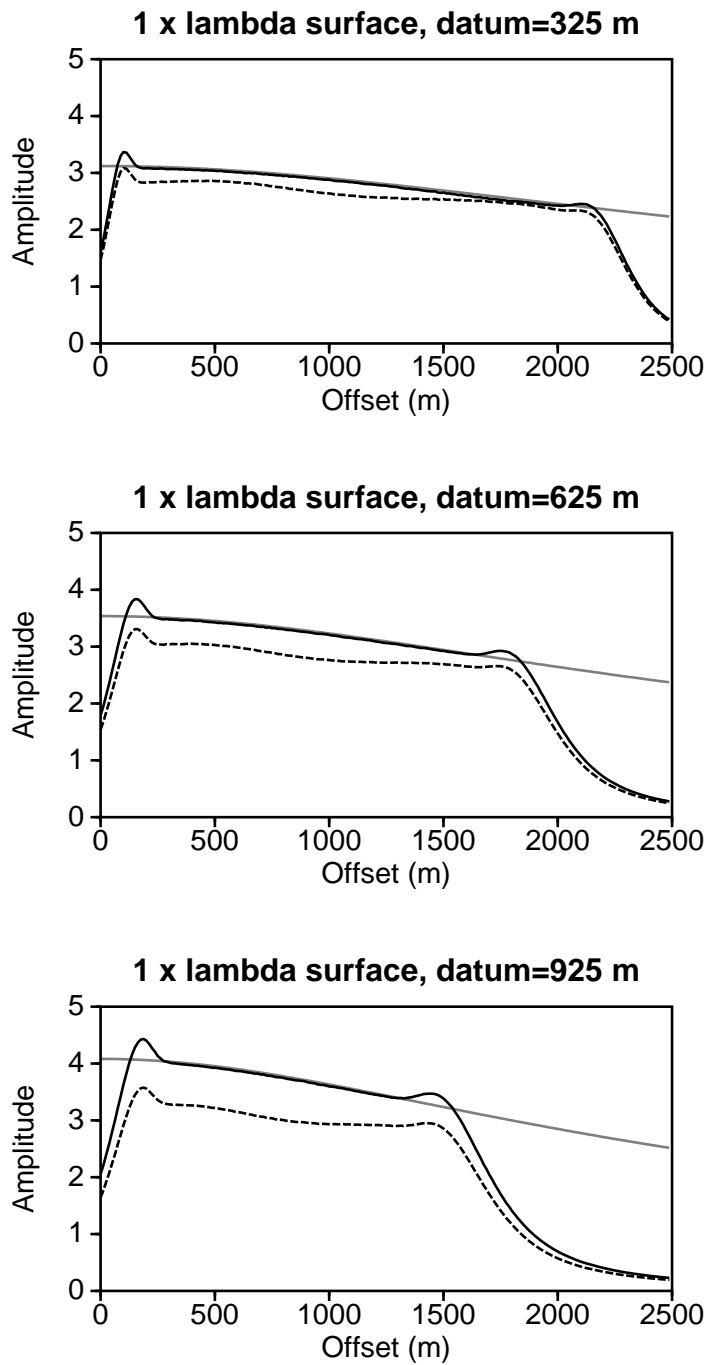


FIG. 6.5. Peak amplitudes for data-mapping and Kirchhoff datuming of receivers from a sinusoidal recording surface of wavelength 2500 m, over a horizontal reflector.

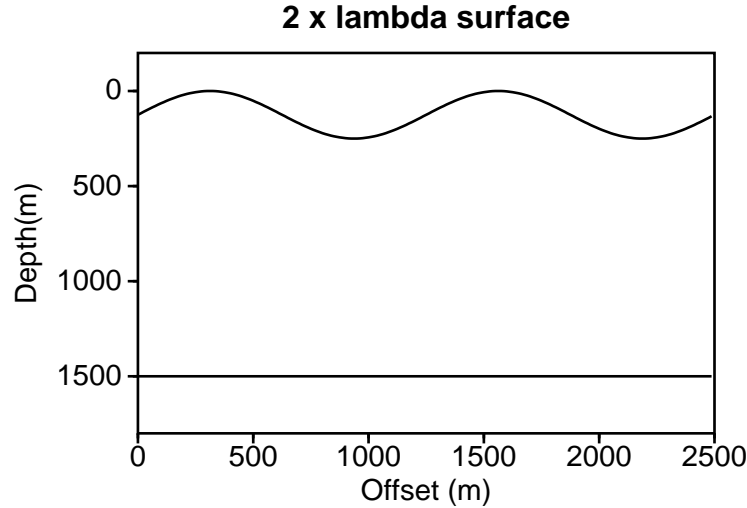


FIG. 6.6. Subsurface model with a sinusoidal recording surface of 1250-m wavelength and 125-m amplitude, over a horizontal reflector, in a constant-wavespeed medium.

The validity condition must hold for all stationary points and rays in the evaluation of the data-mapping result for every output location and output time, and it is impractical to attempt to analyze all of these applications of the condition in this discussion. Nevertheless, evaluating the condition along only the relevant specular rays yields a simple plot that illustrates validity for the main contributions to the output amplitude. So, Figure 6.8 is a plot of V_s for the wave traveling along the specular ray that surfaces at each input receiver location in the current problem, evaluated for $f_0 = 10$ Hz. The gray line is at $V_s = 1$, the validity limit. Contributions to output amplitudes associated with specular rays to input receivers at offsets where the function dips below this line, and therefore violate condition (5.25), are erroneous.

The form of the function V_s in Figure 6.8 makes sense relative to the surface under consideration. Compare Figure 6.8 with Figure 6.6, the model for this calculation. The peaks in V_s correlate with the half-wavelength locations along the sinusoidal surface, where the curvatures are near zero and no validity problems are expected. The valleys in V_s correlate to the peaks and troughs of the sinusoidal surface, where the curvatures are significant, and any violations are expected to occur. The shallower valleys in V_s centered near 900 m and 2200 m are associated with convex-up surface curvatures, opposite to the curvatures of upcoming wavefronts. No violations of the condition occur at these minima. The broader, deeper valleys in V_s centered near 750 m and 1000 m correlate to convex-down curvatures on the recording surface, the same direction as that of the upcoming wavefronts. Violations occur at four locations along these deeper valleys, three of which are inside the useful aperture.

The fact that violations occur in this latter pair of troughs, and not in the

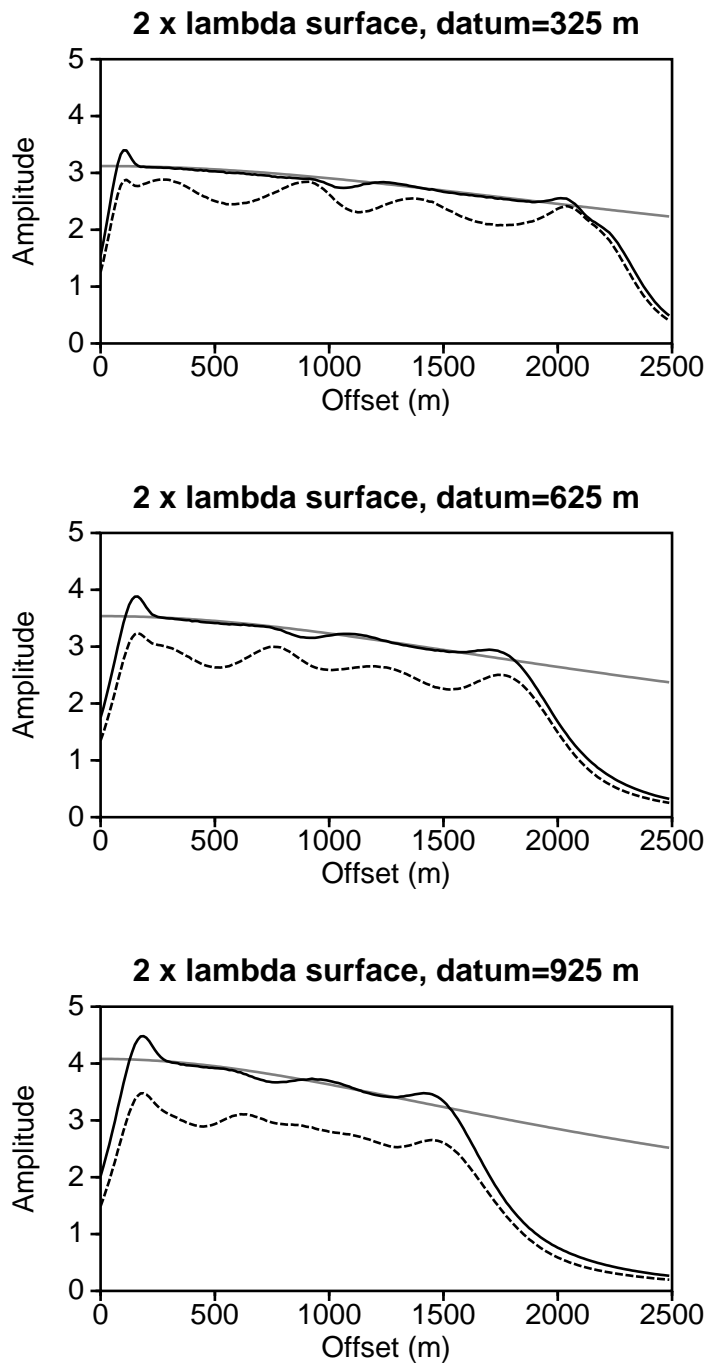


FIG. 6.7. Peak amplitudes for data-mapping and Kirchhoff-datuming of receivers from a sinusoidal recording surface of wavelength 1250 m, over a horizontal reflector.

former, is consistent with the discussions of this validity condition in Chapter 5. It is expected that parts of the function V_s associated with convex-down curvatures on the recording surface violate the condition at smaller curvatures than those that are convex-up, since the value of $M(\kappa_s, \kappa_\phi)$ in condition (6.15), as defined by (5.26), has a smaller value when the wavefront and the recording surface have the same sense of curvature. Namely, it is the absolute value of the difference of curvatures rather than the sum.

In this problem, contributions to the output summations for specular rays that surface any of the four locations on the input surface where $V_s < 1$ are erroneous. For comparison with the downward continuation results in Figure 6.7, however, it is desirable to extrapolate the values of V_s to the output datum surfaces along the appropriate specular ray to their associated output receiver locations. Figure 6.9 is the result of this procedure for the three output surfaces. As the datuming depth is increased, the points of violation of the validity condition, that is, where $V_s < 1$ on the input surface, are associated with output locations of decreasing offset, as is consistent with extrapolation along the upcoming rays in this model.

Recall that the validity condition in these figures is only calculated for the specular ray associated with each receiver. The amplitude at each output location, however, is a weighted summation over contributions from a range of input locations, the most important of which are that where the specular emerges and within some neighborhood surrounding it. So, the errors associated with specular rays that violate the condition do not only degrade the output amplitudes at their associated output locations, but within a surrounding region, as well. Furthermore, it is likely that non-specular rays that surface near these invalid speculars also violate the condition, since they often have similar raypaths and emerge at nearby points on the recording surface with similar curvatures. So, the points where validity is violated on Figure 6.9 are associated not with erroneous points in the output, but with regions of amplitude degradation in Figure 6.7. The size of these degraded regions depends on the net influence of all invalid rays.

A comparison of Figures 6.9 and 6.7 reveals that the errors displayed by both methods occur in offset regions approximately centered on the locations where $V_s < 1$ in Figure 6.9. This suggests, at least qualitatively, that violation of this asymptotic condition on the recording surface is the source of the observed error in both methods.

It is significant to note, though, that the data-mapping result appears to suffer less from the violation of this condition than does Kirchhoff-datuming, all other things being equal. While this study is not able to offer any more explanation for this difference than the data example itself, it is logical to suggest that the assumption of small topographic variation required for the Kirchhoff-datuming method to be applied to non-horizontal surfaces may result in degraded results relative to the data-mapping amplitudes for this recording surface. In any case, the data-mapping procedure appears to handle surface topography better than Kirchhoff datuming with respect to amplitude, even when asymptotic validity is violated. Again, an important consideration in applications where analysis of amplitude variation with offset is

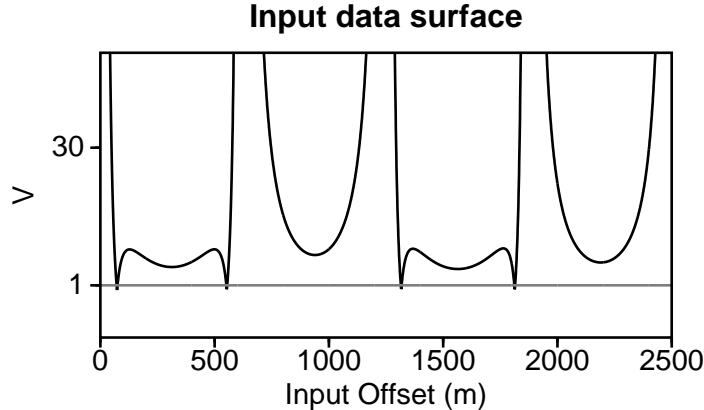


FIG. 6.8. The recording surface validity condition V_s , for a sinusoidal acquisition model with a topographic wavelength of 1250 m, evaluated on the recording surface.

required.

The frequency dependence of condition (6.15) implies that the observed data-mapping error can be corrected if the frequency of the data is increased. A factor of four increase in f roughly accounts for the increase in curvature between this model and the previous model, where no such errors appear. So, Figure 6.10 shows the amplitude results for 80-Hz data.

While the increase of frequency in the input data is enough to heal the small errors in the data-mapping result, it does not result in any significant improvement in the Kirchhoff-datuming result.

Finally, then, consider the sinusoidal model with the topographic variation increased again, this time so that the wavelength of the topography is 835 m, or one-third of the length of the receiver spread, as in Figure 6.11. Note that the wavelet is 20 Hz, as in all but the last example.

The amplitude, displayed in Figure 6.12, in the same form as the previous examples, shows increased error both results because validity conditions associated with the surface are violated further. Figure 6.13 is a plot of V_s for this recording surface on each datum, and shows that the validity condition (6.15) is violated at numerous locations along the recording surface, and sizable errors in amplitude span the entire range of offsets in Figure 6.12 for both methods. The degradation of the data-mapping amplitudes are more significant in this example than in the previous one, and while the data-mapping errors are closer in magnitude to those in the Kirchhoff-datuming amplitudes in this case, they are still better, though to a lesser degree.

The results of these tests show that the data-mapping method has more accurate amplitude and amplitude variation with offset in downward-continued data than does the Kirchhoff-datuming method, particularly when the recording surface is not horizontal.

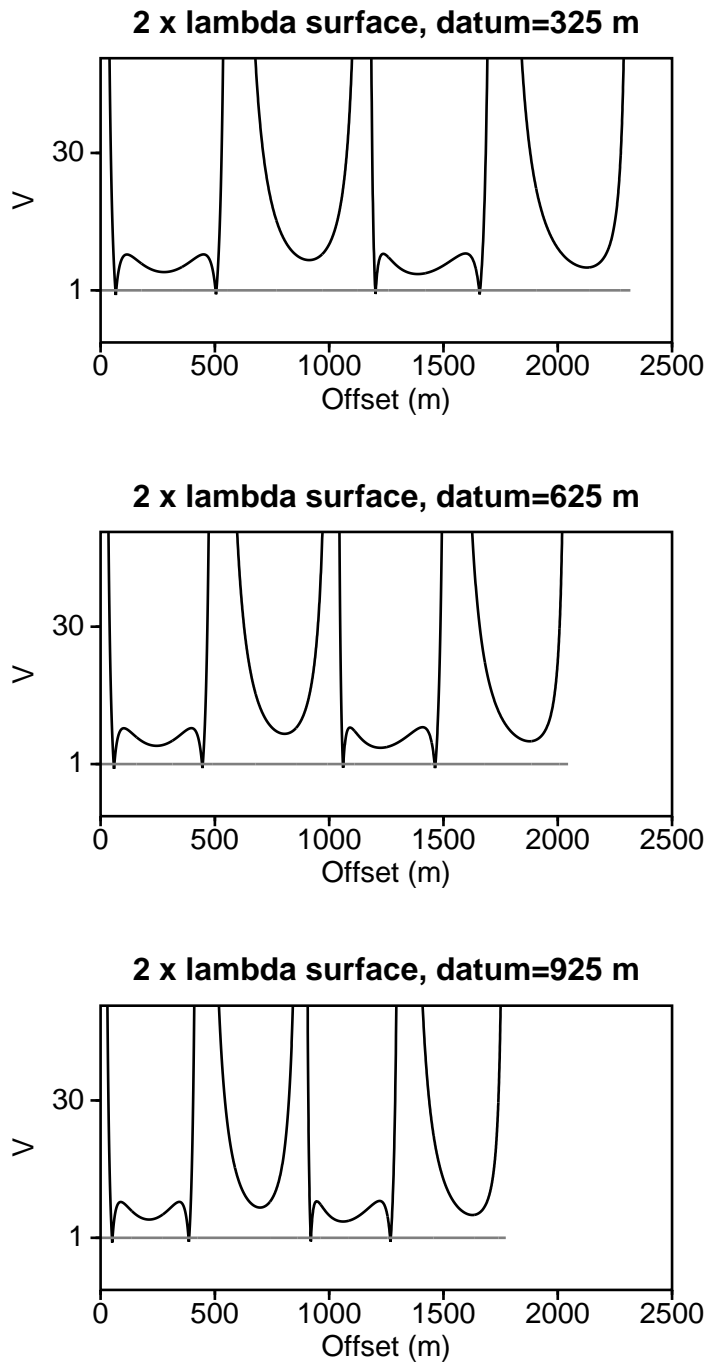


FIG. 6.9. The recording surface validity condition V_s , for a sinusoidal acquisition model with a topographic wavelength of 1250 m, extrapolated to each output datum.

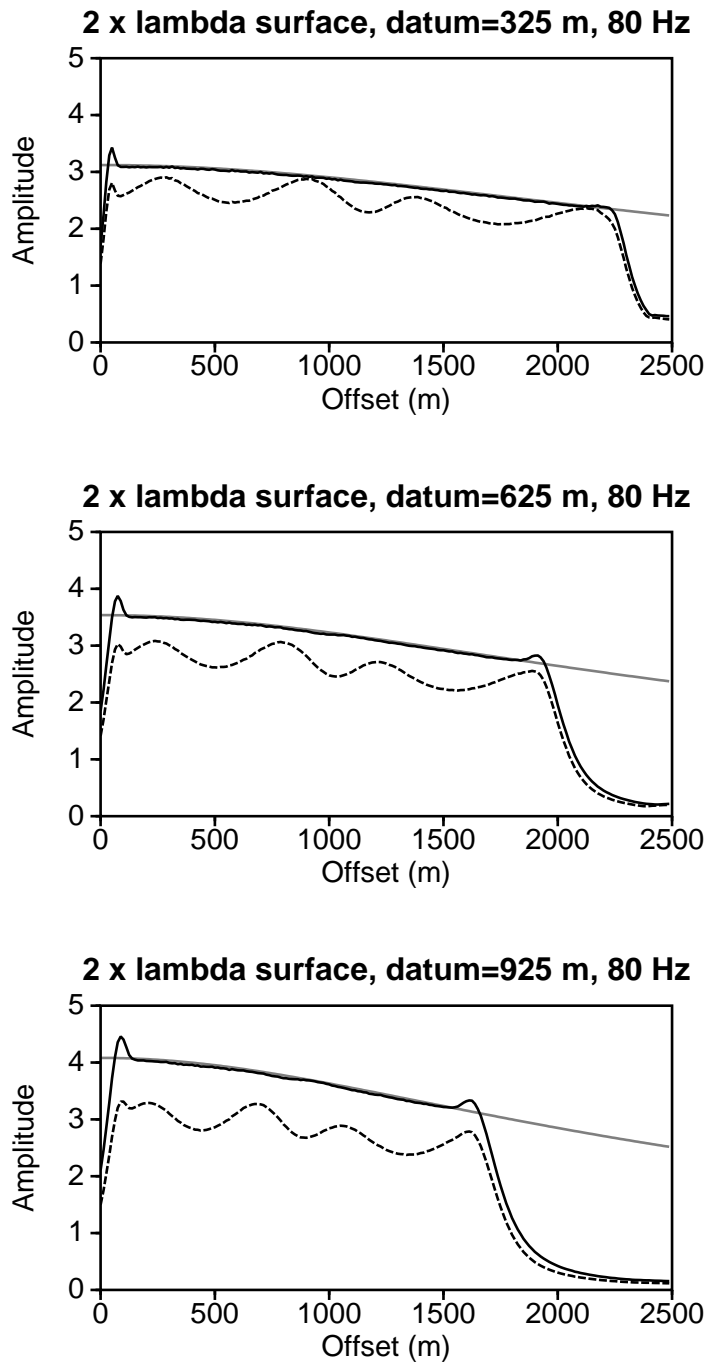


FIG. 6.10. Peak amplitudes for data mapping and Kirchhoff datuming of receivers from a sinusoidal recording surface of wavelength 1250 m, a horizontal reflector, and 80-Hz data.

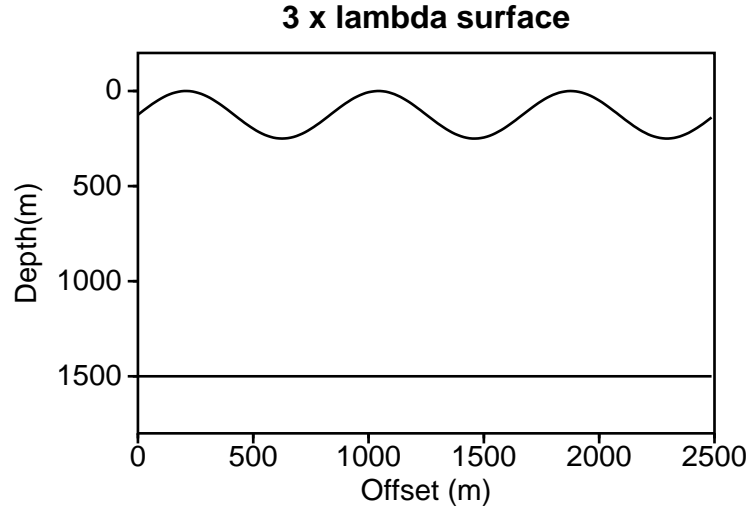


FIG. 6.11. Subsurface model with a sinusoidal recording surface of 835-m wavelength and 125 m amplitude over a horizontal reflector, in a constant-wavespeed medium.

The shape of the reflector is also a consideration in comparing results between data-mapping and Kirchhoff datuming. Some aspects of the two methods are the same with respect to the reflecting surface. The asymptotic validity conditions on the reflector, derived in Chapter 5 for data mapping, must also apply to Kirchhoff-datuming, since it is also an asymptotic method. Furthermore, Kirchhoff datuming requires no additional small-curvature assumption on the reflector as it did on the recording surface.

The data-mapping and Kirchhoff-datuming integrals are not equivalent, however, even when the recording surface is horizontal, since the data-mapping integrand includes an additional factor relative to the Kirchhoff-datuming expression, factor (6.8). Because this factor is a function of incident and scattered raypaths, its value depends on the shapes of both the recording surface and the reflector. Given that the two methods are subject to the same validity conditions on reflector curvature, the shape of the reflecting surface influences the difference in data-mapping and Kirchhoff-datuming amplitudes only in the way that it influences factor (6.8).

Modeling reflector variations is problematic using the CSHOT modeling code, since it is based on a similar asymptotic method, and obeys the same validity conditions as do the downward continuations. Thus, it is not possible to generate accurate synthetic data for reflectors that are near or beyond the allowable curvatures, and a study for progressively more variable reflecting surfaces is difficult. So, this study does not address the issue of reflector curvature in detail.

Nevertheless, examples where the reflector curvature is small are possible. Consider the general subsurface model shown in Figure 4.18, in Chapter 4, where the

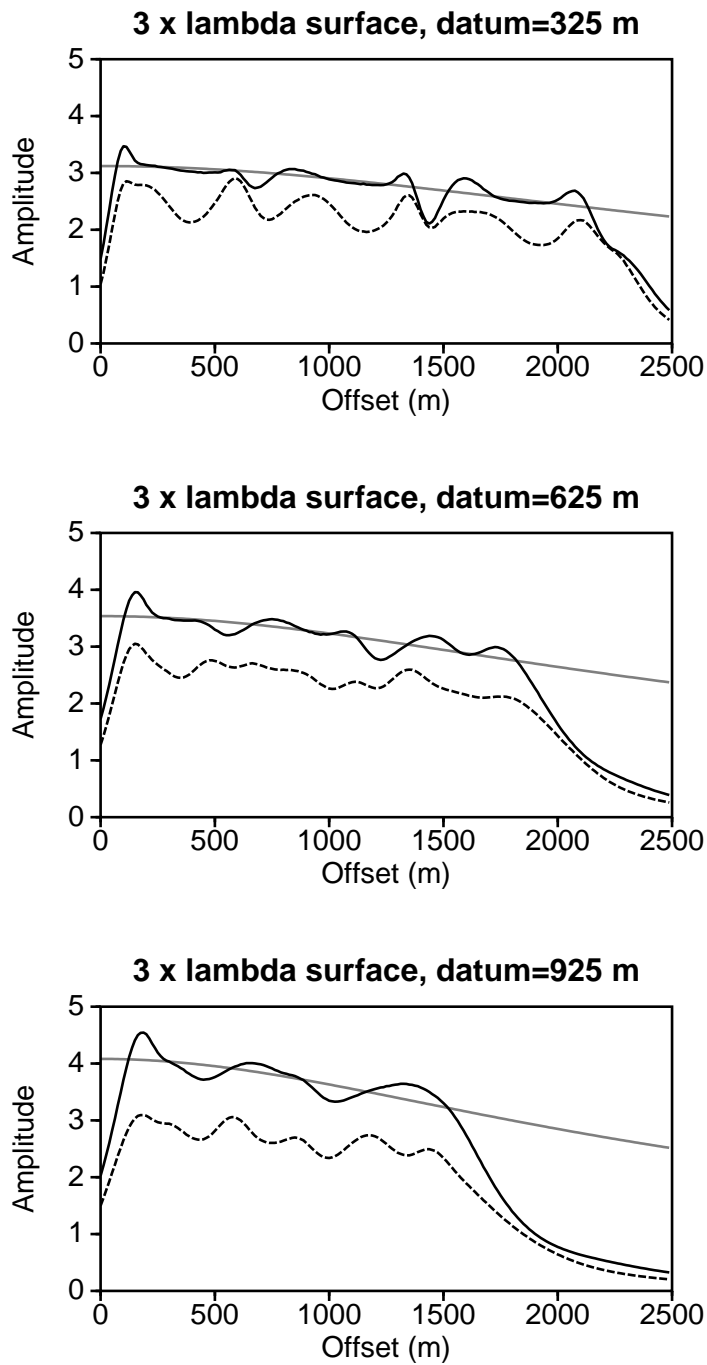


FIG. 6.12. Peak amplitudes for data mapping and Kirchhoff datuming of receivers from a sinusoidal recording surface of wavelength 835 m, over a horizontal reflector.

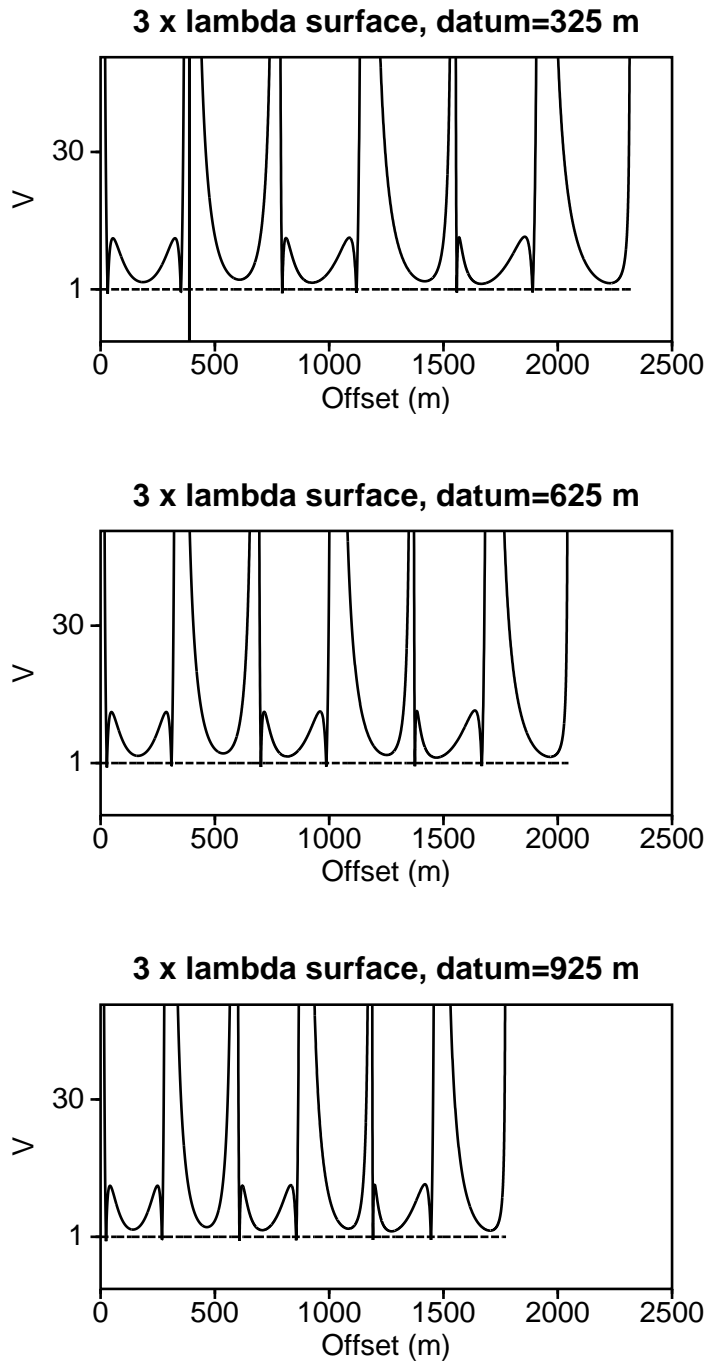


FIG. 6.13. The recording surface validity condition V_s , for a sinusoidal acquisition model with a topographic wavelength of 835 m, extrapolated to each output datum.

recording surface is roughly a sinusoid of 125-m amplitude, and the recording surface is curved. Figure 6.14 shows the peak-amplitude comparison for this model.

This model is roughly the same as the previous example depicted in Figure 6.4, except that the reflector is curved. Note also that the CSHOT modeling code used to generate the data for this model creates the recording surface via a cubic spline calculation, so it is not exactly sinusoidal. It is, however, a close approximation, and allows a qualitative comparison between the results of the two models.

Compare the amplitude plots from the curved reflector model, Figure 6.14, with those from the horizontal reflector model, Figure 6.5. While the amplitude functions differ, the difference in amplitude and amplitude variation with offset between the data-mapping and Kirchhoff-datuming results does not appear to have increased for the curved reflector, and the two models show a difference of a similar character. In this example, at least, it appears that the difference between the data-mapping and Kirchhoff-datuming amplitudes can be accounted for by the influence of factor (6.8) and that of the topographic surface, as previously discussed. Nevertheless, further study is required to fully understand the influence of reflector curvature in the two results.

6.3 Non-Kirchhoff methods

Kirchhoff methods are not the only approach to downward continuation, and there exist wave-equation based, non-Kirchhoff methods that are able to preserve amplitude while only using information about the subsurface between the recording surface and the datum. For example, extrapolation methods based on a frequency-domain or phase-shift operator, such as those used in Stolt (1978) and Gazdag (1978), as well as finite-difference methods, including those reviewed in Berkhout (1981), preserve amplitude in constant-wavespeed models, as well as many types of heterogeneous models, depending on the method. These methods are often more accurate and more computationally efficient than Kirchhoff methods.

These wave-equation methods, though, are generally limited to extrapolation from a horizontal recording surface, where the source and receiver spacing is regular. Therefore, they are not well suited for the downward continuation of data collected on irregular topography, and do not generally preserve amplitude in such a case. Alternatively, Kirchhoff methods generally allow for non-uniform source and receiver spacing, and the data-mapping method, in particular, allows for a variable recording surface.

Furthermore, these non-Kirchhoff methods are based on either 2D or 3D forms of the wave-equation, and while 3D geometrical spreading is properly accounted for in the 3D calculations, it requires data collected in a 2D array on the recording surface. For data collected in a linear survey, the application of a 2D wave-equation method will not preserve 3D amplitudes, since the method implicitly assumes 2D geometrical spreading. Unlike wave-equation methods, however, data mapping is readily adaptable to 2.5D, which allows data collected in a single line on the surface

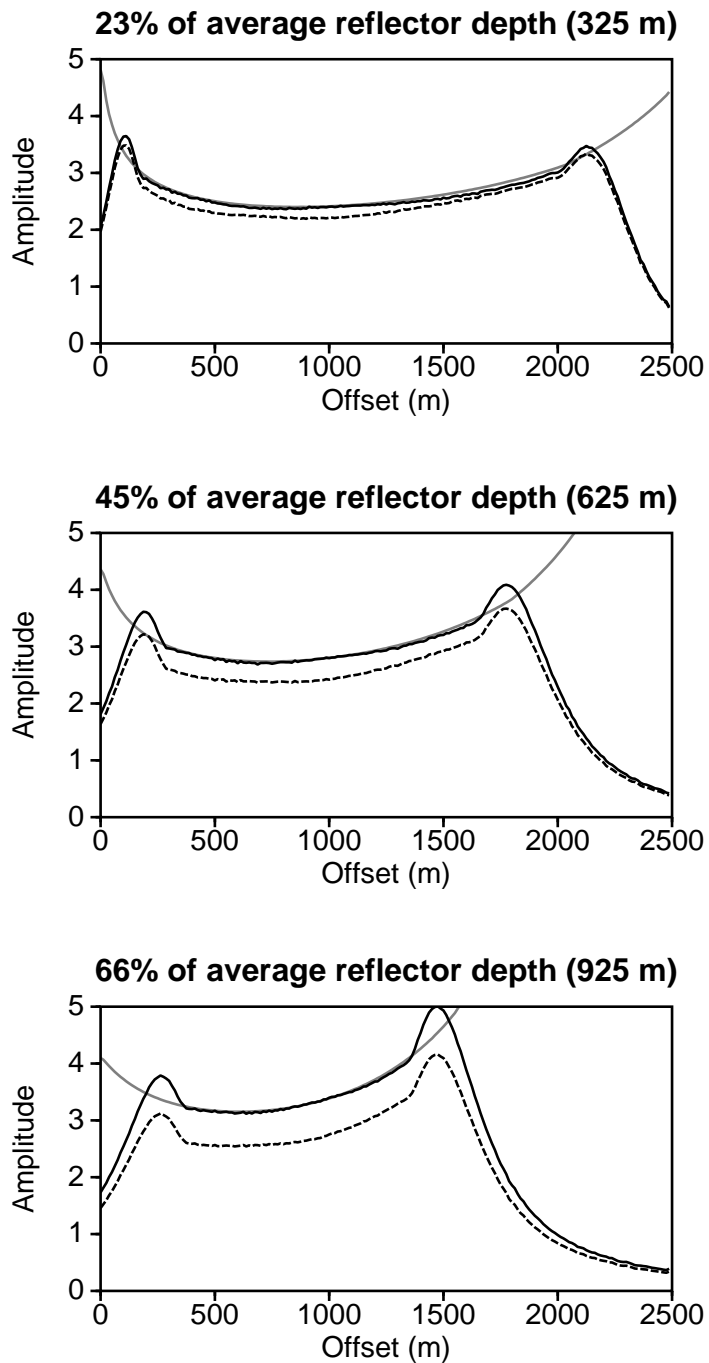


FIG. 6.14. Peak amplitudes for data mapping and Kirchhoff datuming of receivers from a topographic recording surface of 1250-m wavelength, over a curved reflector.

to be extrapolated via a 2D calculation and still preserve 3D geometrical spreading, provided that the subsurface may be assumed constant in the direction normal to the survey line.

Although recent developments in the study of unequally-spaced Fourier transforms, such as those described in Beylkin (1995), may soon result in wave-equation extrapolations that accommodate unequally spaced sources and receivers, data collected on rugged topography or in linear surveys are still best downward continued using Kirchhoff methods. The data-mapping method is one possible choice that will preserve amplitude for a topographic recording surface, as well as for data collected in a linear survey when the 2.5D assumption is appropriate.

Chapter 7

CONCLUSIONS AND FUTURE WORK

7.1 Discussion and conclusions

Among the applications of downward extrapolation of seismic data, two are of primary importance. First, downward continuation is a key step in migration, along with the application of an appropriate imaging condition. The second use is as a preprocessing step for migration, perhaps for the extrapolation of data from a topographic recording surface to a horizontal datum, so they can be used for input to migration algorithms that do not accommodate an irregular acquisition surface. It may also be employed as an intermediate step in a layered migration, such as that described in Bevc (1995), where multipathing is addressed by alternating steps of downward continuation and migration. Regardless of the way in which it is used, downward continuation is a central step in the determination of the final, migrated image. Consequently, preservation of amplitude or amplitude variation with offset in the migrated image requires an extrapolation algorithm that also preserves amplitude. The algorithms used in practice are kinematically correct, but are often not dynamically accurate even when the correct wavespeed model is used. Furthermore, they typically cannot accommodate significant topographic variations on the recording surface.

The 2.5D downward continuation method for data collected in common-source and common-receiver configurations derived here from the general Kirchhoff data-mapping theory of Bleistein & Jaramillo (1997, 1999) yields expressions for “true-amplitude” downward continuation of receivers or sources in heterogeneous media. It is true amplitude in the sense that amplitudes in the output data are consistent with an extrapolation through the given wavespeed model, assuming the absence of multipathing. Moreover, the data-mapping procedure is derived under the assumption that the recording and datuming surfaces may not be horizontal.

As noted above, a primary application of downward continuation is as a key step in the development of a Kirchhoff migration algorithm, along with an appropriate imaging condition. Therefore, it is appropriate to ask if the data-mapping extrapolation can be used to produce a migration algorithm that is “true amplitude” in the same sense as data-mapping. It is essential to note, though, this algorithm already exists. Data mapping is a cascade of a modeling formula and an inversion formula. This inversion is a “true-amplitude” migration in the same sense as data mapping, and details are found in Bleistein et al., (1997).

In fact, it is not generally possible to use the data-mapping extrapolation for true-amplitude imaging (inversion). Imaging requires that the data be downward

continued onto the reflecting surface. Data-mapping is based on asymptotic ray theory, and as a result, the data-mapping integral for receiver continuation is proportional to the ray-theoretical Green's function amplitude $A(\mathbf{x}_{OG}, \mathbf{x})$, as defined by equation (2.25). This amplitude is inversely proportional to the square root of $|J(\mathbf{x}_{OG}, \mathbf{x})|$, the Jacobian along the raypath connecting \mathbf{x}_{OG} and \mathbf{x} . When the datum is coincident with the reflector, asymptotic ray theory breaks-down, since $|J(\mathbf{x}_{OG}, \mathbf{x})| = 0$ and the Green's function amplitude is unbounded. Furthermore, the assumption that the datum and reflector are coincident results in the second derivative of the phase becoming unbounded, since the curvature κ_{OG} becomes infinite. Simply put, the asymptotics assumed in the data-mapping integral break-down.

Fortuitously, factors in the amplitude combine in such a way that equation (2.26) is indeterminate when the output is coincident with the reflector, and the integral turns out to be bounded. So, the application of an imaging condition to (2.26) results in an equation with correct kinematics, but where the amplitudes are unreliable due to the break-down of asymptotics. Therefore, the data-mapping downward continuation could be adapted for migration, but not for inversion. Preservation of 2.5D amplitudes in imaging is obtained by using the 2.5D asymptotic inversion that already exists in Bleistein et al., (1997). The same discussion applies to source continuation.

Given this, the main application of the data-mapping extrapolation is probably that of a preprocessing step prior to migration. Since it accommodates irregular recording surface topography, it is useful for wave-equation datuming, the extrapolation of input data to a horizontal datum, particularly when amplitude variation with offset (AVO) must be preserved.

Simple synthetic models show that the data-mapping method can produce accurate amplitudes and amplitude variation with offset, even when the recording surface is not horizontal. Due to finite data aperture, however, accurate output amplitudes are not generally obtained for all offsets present in the input data, but only within a useful aperture interior to the ends of the receiver spread, the width of which decreases with increasing proximity of the datum surface to the target reflector. Furthermore, amplitudes at any data location may degrade because of violations of asymptotic validity conditions arising from stationary phase approximations inherent in the data mapping platform. Specifically, these conditions limit various length scales in the problem, including the radii of curvature on the recording surface and the reflector.

While the validity conditions involve several quantities, data mapping distorts amplitudes most severely when the surface curvatures are too large, all other things being equal. This is of particular importance for the application of the method to wave-equation datuming of data collected on rugged terrain, as these validity conditions are certainly violated in many acquisition environments. The assumption of no multipathing also limits the models for which the data-mapping result is expected to preserve amplitudes, however, this is a common limitation of ray-based methods, including those of Berryhill (1979) and Bevc (1995). Even with these assumptions and conditions, there is still a large set of models for which the method can acceptably preserve amplitude for data processing and AVO/AVA analysis.

The value of the data-mapping approach as an amplitude preserving method is outlined further when it is compared to other, more familiar Kirchhoff-based downward-continuation methods. Preservation 3D spreading amplitudes in the extrapolation of line data requires a 2.5D method. Common adaptations of 3D Kirchhoff-datuming schemes to line data, such as those in Berryhill (1979), Bevc (1995), and Salinas (1997), reduce the 3D problem to an in-plane calculation that is kinematically correct, but does not produce 2.5D amplitudes. These adaptations are based on the assumption that the input data are independent of one lateral direction on the recording surface, an assumption that is incorrect point-source data. Therefore, these methods yield integrals that do not correctly account for out-of-plane spreading. Furthermore, unlike data mapping, these methods explicitly assume a horizontal recording surface in their basic derivation, introducing a further degradation in the accuracy of their output amplitudes when the recording surface has a significant topographic variation.

These issues result in differing amplitude weights in the integrands of the data-mapping and Kirchhoff-datuming integrals. In simple synthetic models, it is seen that when the recording and reflecting surfaces are horizontal, the influence of these differing factors is to produce roughly a constant relative shift between the results, and each method appears to produce the correct AVO behavior. When surface topography is substantial, however, the data-mapping method yields distinctively superior amplitude behavior with offset. Nevertheless, in areas of rough terrain, the amplitudes resulting from both methods may be unacceptable for AVO analysis.

While the analytic comparisons and the synthetic models show that the Kirchhoff-datuming method does not handle surface topography as well as does data-mapping with respect to accurate output amplitudes and AVO, even when the derivative of the true surface normal is used, both methods do break-down for realistic curvatures on the recording surface that are too large. The models suggest, however, that the Kirchhoff-datuming method breaks-down faster than does the data mapping as the surface curvature is increased. This is consistent with the fact that the data-mapping derivation allows for a recording surface that is irregular, while Kirchhoff-datuming method explicitly assumes that it is horizontal, requiring additional modifications to approximate small topographic variations. The results suggest that data mapping is capable of producing more accurate amplitude and AVO behavior than does Kirchhoff datuming even when the recording-surface curvatures begin to violate the relevant validity conditions. This observation is especially significant for application of the data-mapping method for datum correction in areas of irregular terrain, where preservation of amplitudes and analysis of amplitude variation with offset is required. Again, however, in areas where the topographic variation along the recording surface is too large, *neither* approach yields sufficiently accurate AVO behavior.

7.2 Future work

Most of the discussion in this study concentrates on illustrative results from constant-wavespeed models, but the general downward continuation method for heterogeneous media is derived here, as well. Therefore, a future step might be to implement the method in a more complex medium. However, the evaluation of the relevant amplitude weighting factors for non-constant wavespeed, namely the various σ 's, Jacobians, and traveltimes gradients that appear equations (2.26) and (2.29), is not trivial. While it is probably not possible to construct a totally analytic procedure for general media, the case of a medium with a wavespeed that is purely depth-dependent, a $v(z)$ medium, is likely tractable and efficient with a procedure that combines both analytic and numerical approaches to the determination of the relevant factors. A model of this type is applicable in many field data situations, and could be used to produce a useful processing algorithm.

Models more complex than $v(z)$ are possible only with extensive numerical ray tracing procedures that would probably be considered prohibitively expensive at the current time. However, many data processing procedures, such as datuming, migration, and dip-moveout (DMO), are commonly performed, in practice, under the assumption of a constant or $v(z)$ wavespeed model for amplitude determination. Therefore, an efficient "true-amplitude" datuming algorithm for depth-dependent media and surface topography would most likely be considered an advance in current industrial practice.

While the implementation of the data-mapping method of downward continuation in $v(z)$ media is an important extension of this study, other extensions of data mapping, in general, could be of interest. The application of the method to processes such as transformation-to-zero-offset (TZO), DMO, and offset continuation, as well as to data mapping in 3D, are discussed in Bleistein & Jaramillo (1997, 1999), Bleistein (1998a), Bleistein (1998b), and Jaramillo & Bleistein (1998).

Finally, the near-surface is often complex, with various types of possible wavespeed anomalies, and it is likely that the results of wave-equation datuming using the data-mapping method, and, thus, those of any subsequent migration, will be degraded by the presence of multipathing. It may be possible to adapt the data-mapping method to properly account for multipathing and caustics, greatly increasing the number of models for which the method is valid. This would be a significant contribution, not just to downward continuation, but to all the applications of the data-mapping theory.

REFERENCES

- A. J. Berkhout, 1981. Wavefield Extrapolation Techniques in Seismic Migration, a Tutorial. *Geophysics*, **46**, 1638-1656.
- J. R. Berryhill, 1979. Wave-equation Datuming. *Geophysics*, **44**, 1329-1344.
- J. R. Berryhill, 1984. Wave-equation Datuming Before Stack (Short Note). *Geophysics*, **49**, 2064-2066.
- D. Bevc, 1995. Imaging Under Rugged Topography and Complex Velocity Structure. Ph.D. Thesis, Department of Geophysics, Stanford University.
- G. Beylkin, 1995. On the Fast Fourier Transform of Functions with Singularities. PAM Report 195, *App. and Comp. Harm. Anal.*, **2**, 363-381.
- N. Bleistein, 1998a. 2.5D Data Mappings. 68th Annual Internat. Mtg., Soc. Expl. Geophys., Expanded Abstracts, **98**, 1353-1356.
- N. Bleistein, 1998b. True-Amplitude 3D Constant Background DMO - An Implementation of Data Mapping. 68th Annual Internat. Mtg., Soc. Expl. Geophys., Expanded Abstracts, **98**, 1760-1763.
- N. Bleistein & H. Jaramillo, 1999. A Platform for Kirchhoff Data Mapping in Scalar Models of Data Acquisition. To appear in *Geophys. Prosp.*.
- N. Bleistein & H. Jaramillo, 1997. A Platform for Kirchhoff Data Mapping in Scalar Models of Data Acquisition. CWP-267, Colorado School of Mines.
- N. Bleistein, J.K. Cohen, and J. Stockwell, Jr., 1997. *Mathematics of Multidimensional Seismic Inversion*. In preparation.
- N. Bleistein, 1986. Two-and-One-Half Dimensional In-Plane Wave Propagation. *Geophys. Prosp.*, **34**, 686-703.
- N. Bleistein & R.A. Handelsman, 1986. *Asymptotic Expansions of Integrals*. Dover, New York.
- N. Bleistein, 1984. *Mathematical Methods for Wave Phenomena*. Academic Press, New York.
- J. K. Cohen, 1990. Aperture for Kirchhoff Inversion. CWP-079R, Colorado School of Mines.
- P. Docherty, 1991. Documentation for the 2.5D Common-Shot Modeling Program CSHOT. CWP-U08R, Colorado School of Mines.

- J. Gazdag, 1978. Wave Equation Migration with the Phase-Shift Method. *Geophysics*, **43**, 1342-1351.
- H. Jaramillo & N. Bleistein, 1998. Seismic Data Mapping. 68th Annual Internat. Mtg., Soc. Expl. Geophys., Expanded Abstracts, 98, 1991-1994.
- T. Salinas, 1997. The Influence of Near-Surface Time Anomalies in the Imaging Process. M.Sc. Thesis, Colorado School of Mines.
- W. A. Schneider, 1978. Integral Formulation of Migration in Two and Three Dimensions. *Geophysics*, **43**, 49-76.
- R. Stolt, 1978. Migration by Fourier Transform. *Geophysics*, **43**, 23-48.
- X. Zhu, B.G. Angstman, and D.P. Sixta, 1995. Overthrust Imaging with Tomo-Datuming. 65th Annual Internat. Mtg., Soc. Expl. Geophys., Expanded Abstracts, 95, 1397-1400.

Appendix A

DERIVATION OF THE FACTOR G FOR CONSTANT-WAVESPEED MEDIA

This appendix contains the derivation of the topographic factor $G(\bar{x}_1, \bar{x}_3)$, for receiver continuation, as given in equations (3.6) and (3.7). First, assume the same definitions for the source and receiver locations as in equation (3.1),

$$\mathbf{x}_{IG} = (\xi_I, z_I(\xi_I)) , \quad \mathbf{x}_{OG} = (\xi_O, z_O) , \quad \mathbf{x}_S = (x_S, z_S(\xi_I)) , \quad (\text{A.1})$$

as well as for the stationary point,

$$\mathbf{x} = (\bar{x}_1, \bar{x}_3) . \quad (\text{A.2})$$

Referring to Figure 3.1, the path r_{IG} is represented by the vector

$$\mathbf{r}_{IG} = (\bar{x}_1 - \xi_I, \bar{x}_3 - z_I) . \quad (\text{A.3})$$

The gradient of the isochron associated with waves propagating along this path is a vector pointing in the direction of \mathbf{r}_{IG} with magnitude $1/c$, or

$$\nabla_{\mathbf{x}} \tau_{IG} = \frac{\mathbf{r}_{IG}}{c r_{IG}} = \frac{1}{c r_{IG}} (\bar{x}_1 - \xi_I, \bar{x}_3 - z_I) . \quad (\text{A.4})$$

The derivative of this gradient with respect to the parameter ξ_I is then

$$\frac{\partial \nabla_{\mathbf{x}} \tau_{IG}}{\partial \xi_I} = \frac{\partial}{\partial \xi_I} \left(\frac{\bar{x}_1 - \xi_I}{c r_{IG}} \right) \hat{x}_1 + \frac{\partial}{\partial \xi_I} \left(\frac{\bar{x}_3 - z_I}{c r_{IG}} \right) \hat{x}_3 , \quad (\text{A.5})$$

where \hat{x}_1 and \hat{x}_3 are unit vectors along the corresponding coordinate axes. Remembering that z_I is a function of ξ_I , performing the differentiations yields

$$\begin{aligned} \frac{\partial \nabla_{\mathbf{x}} \tau_{IG}}{\partial \xi_I} &= \frac{1}{c r_{IG}^3} \left[(\bar{x}_1 - \xi_I) (\bar{x}_3 - z_I) \frac{\partial z_I}{\partial \xi_I} - (\bar{x}_3 - z_I)^2 \right] \hat{x}_1 \\ &\quad + \frac{1}{c r_{IG}^3} \left[(\bar{x}_1 - \xi_I) (\bar{x}_3 - z_I) - (\bar{x}_3 - z_I)^2 \frac{\partial z_I}{\partial \xi_I} \right] \hat{x}_3 . \end{aligned} \quad (\text{A.6})$$

Calculating the magnitude of the vector produces a perfect square in terms of the derivative, yielding

$$\left| \frac{\partial \nabla_{\mathbf{x}} \tau_{IG}}{\partial \xi_I} \right| = \frac{1}{c r_{IG}^2} \left| (\bar{x}_3 - z_I) - (\bar{x}_1 - \xi_I) \frac{\partial z_I}{\partial \xi_I} \right| . \quad (\text{A.7})$$

In the text, the second factor is expressed as G , so that

$$\left| \frac{\partial \nabla_{\mathbf{x}} \tau_{IG}}{\partial \xi_I} \right| = \frac{G(\bar{x}_1, \bar{x}_3)}{c r_{IG}^2}, \quad (\text{A.8})$$

where G is defined as in equation (3.7).

The expression for this factor in source continuation follows an analogous derivation, where only the source and receiver parameters are interchanged, yielding equation (3.30).